# 博士論文

# Simulation study of scrape-off-layer plasmas by a virtual divertor model incorporating ion temperature anisotropy

# (非等方イオン温度に基づいた仮想ダイバータモデルによるスクレイプオフ層プラズマのシミュレーション研究)

東郷　訓

新領域創成科学研究科

先端エネルギー工学専攻

# INDEX

# List of Figures

# List of Tables

# Chapter 1
# Introduction

## 1.1 Roles of divertor in tokamaks

Tokamaks are considered to be one of the most promising candidates in order to commercialize the fusion reactors. Many existing tokamaks, such as ASDEX-Upgrade [1, 2], JET [3, 4] and DIII-D [5, 6], and future ones, such as JT-60SA [7, 8], ITER [9, 10] and DEMO [11, 12], adopt divertor magnetic configuration. The purpose of the implementation of the divertor magnetic configuration is to reduce the interaction of the hot plasma and the first wall, which may cause a contamination and dilution of the core plasma, which is sufficiently hot to be in charge of the fusion reactions, by the sputtered impurity particles. Before the divertor magnetic configuration started to be implemented, the limiter configuration was generally used. The limiter is a protruding object in the vacuum vessel and *limits* the radius of the core plasma as shown in Fig. 1 (a). The position of the plasma-wall interaction is limited to the limiter which consists of high-melting-point materials. In the limiter configuration, however, the sputtered impurity particles can easily go into the core plasma as is clear from Fig. 1 (a). The divertor magnetic configuration was first applied to JFT-2a device [13]. The basic idea is to determine the surface of the core plasma by the figure-of-eight separatrix by applying a current to the divertor coil in the same direction as the plasma current as shown in Fig. 1 (b). Here, the region of open magnetic field adjacent to the core plasma is called scrape-off-layer (SOL). The cross-point of the separatrix is called the X-point. The region between X-point and the divertor plates is called the divertor region (DIV). Because the core plasma is far from the walls in the parallel direction to the magnetic field, the impurity particles are expected to be confined in DIV by the friction with the ion flow avoiding the contamination and dilution of core plasma. In addition, the first discovery of the H-mode by ASDEX [14] made the divertor configuration mainstream in the fusion researches.

The walls including the divertor plates work as a strong particle sink for the plasma particles because the charged particles striking the solid surface tend to stick to it for a time long enough to recombine (surface recombination) and are

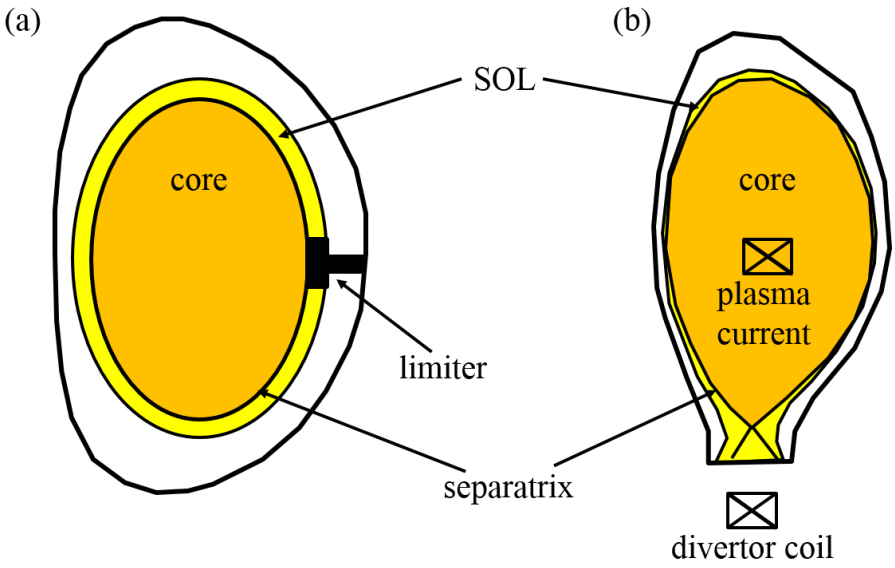


Figure 1 Poloidal cross section of tokamaks with (a) the limiter and (b) the divertor configurations.

released as neutral particles [15]. Some of these neutrals are pumped and the others are re-enter the plasma and ionized in the core or SOL-DIV plasma. This process is called recycling. Due to this recycling process, high density and low temperature plasmas are generated in DIV which promote the impurity radiation and reduce the heat load on the divertor plates (high recycling regime).

## 1.2 Necessity of power handling

Reduction of the divertor heat load is one of the most important issues in order to commercialize the fusion reactors [16]. The heat flux from the core plasma is received by the plasma wetted area of ~ 5 $m^2$ on the divertor plates. Thus, the heat flux should be reduced by radiation in SOL-DIV to the tolerable value from the material of the divertor plate point of view. In case of ITER, whose neutron load is much less than DEMO, the tolerable heat flux density is estimated to be 10 $MW/m^2$ by using the tungsten and copper alloy. The heat flux from the core is estimated to be 100 MW, so that more than 50 % should be removed by radiation in SOL-DIV. In case of SlimCS [17, 12], which is one of the DEMO reactors of 3 GW fusion power and has ITER-like size, the neutron load is too high to avoid the radioactivation of the copper alloy. When the tungsten and reduced radioactivation ferritic martensitic steel are used, the tolerable heat flux density is evaluated to be 5-7 $MW/m^2$ [17]. Meanwhile, the heat flux from the core becomes more than 500

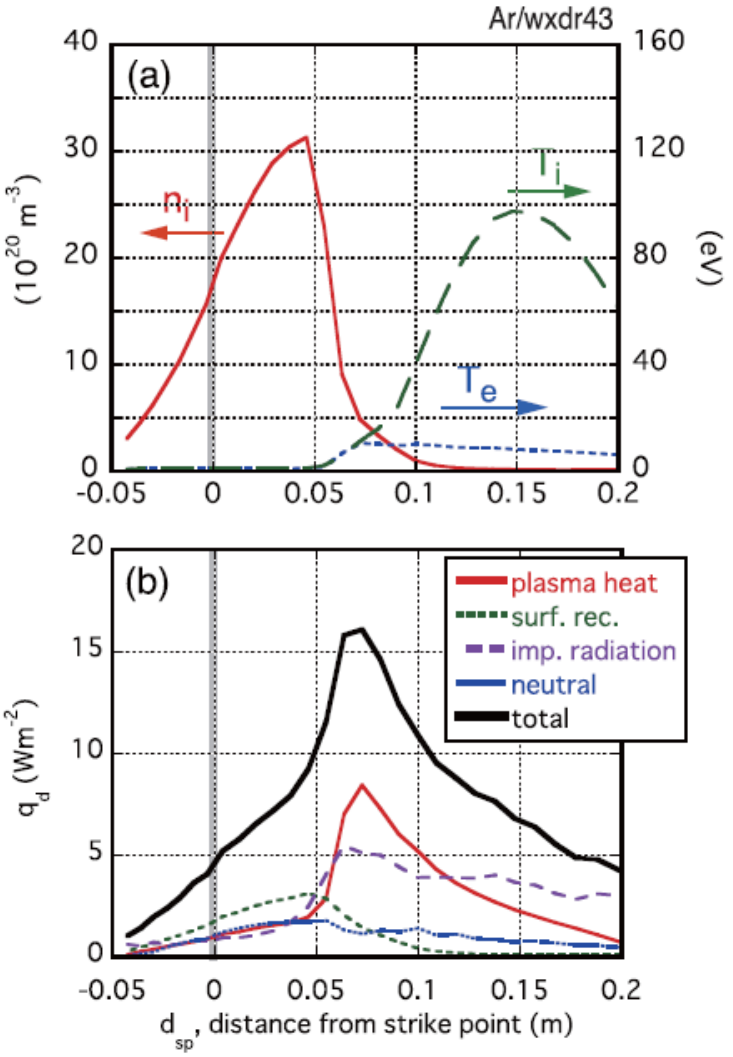


Figure 2 Radial profiles of (a) ion density $n_i$, electron temperature $T_e$ and ion temperature $T_i$, and (b) the target heat load [18].

MW, 5-6 times as large as the heat flux of ITER. It is, therefore, necessary to remove more than ~ 95 % of the heat flux by radiation in SOL-DIV. However, it was reported by the simulations of SONIC, a SOL-DIV plasma code package, that even if 92 % of the heat flux from the core plasma was radiated, the peak heat flux density became 16 MW/m$^2$ due to the radiated power to the divertor plate and the surface recombination although the plasma heat load decreased to less than 8 MW/m$^2$ as shown in Fig. 2 which corresponds to Fig. 5 in Ref. [18]. This result highlights the technological difficulty of the power handling in the fusion reactors of 3 GW fusion power.

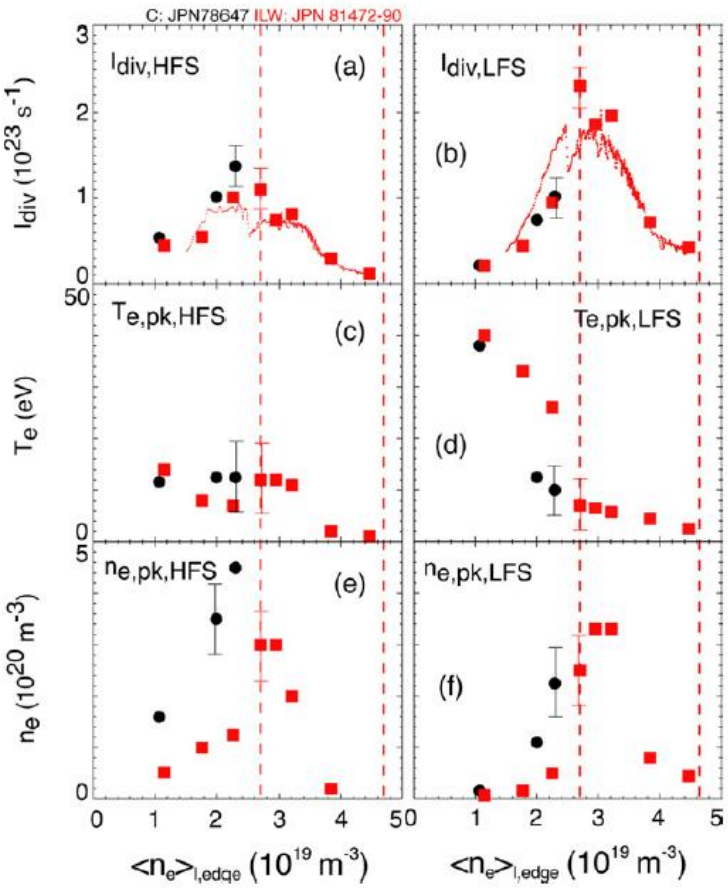


Figure 3 Total input power and radiated power in the core (*a*), total radiated power in the HFS and LFS divertor legs (*b*), radiated power in the entire SOL and in the divertor (*c*), and total conducted power to the HFS and LFS plates (*d*) as a function of line-averaged edge density. Black symbols refer to JET-C, the red symbols to JET-ILW. The two vertical red lines indicate, for JET-ILW, the densities at which the rollover of the ion current to the LFS plate (left line) and the global density limit (right line) occurred [19].

## 1.3 Detached plasma

In the density ramp-up experiments in tokamaks, the particle flux to the divertor plate, which is usually measured as the ion saturation current by the Langmuir probe, increases at first and SOL-DIV plasma transits from low to high recycling regime. But as the electron temperature becomes low, the reaction rate of ionization decreases, so that the particle flux to the divertor starts to decrease (roll-over). When the electron temperature becomes lower than a few eV, the volume recombination reaction dominates leading to the significant decrease of the

particle flux to the divertor plate. This phenomenon is called detached plasma and expected to reduce the divertor heat load more than the high recycling regime. The detached plasma or corresponding decrease of the ion saturation current is observed in many representative tokamaks such as JET [19], ASEDX-Upgrade [20] and JT-60U [21]. Figure 3, which corresponds to Fig. 2 in Ref. [19], shows the observation of the detached plasma in JET. When the line-averaged edge density becomes larger than the critical value represented by the left vertical broken line, the ion saturation current starts to decrease and comparably cold and thin plasma is formed. In order to control the detached plasma, the physical mechanism of it is researched from the aspects of experiments and simulations.

## 1.4 SOL-DIV plasma code package

Simulation studies with precise models are important in order to quantitatively predict the profiles of plasma in SOL-DIV and the heat load on the divertor plate for the future devices. For this purpose, many SOL-DIV plasma code packages such as SOLPS [22], SONIC [23, 24], UEDGE [25] and EDGE2D/NIMBUS (EIRENE) [26] are utilized worldwide. Because it is necessary to simultaneously consider the atomic and molecular processes and the generation, transport and interaction of neutrals and impurities in addition to the plasma transport in SOL-DIV, most of the code packages consist of the codes for plasma, neutral and impurity and solve them self-consistently.

There are largely two models for describing the dynamics of these particles; kinetic and fluid models. The kinetic model describes the velocity distribution function of one species of particles by so-called Boltzmann equation (in case of the plasma, it is particularly called Fokker-Planck equation by replacing the collisional term of gas by that of Coulomb collision). The fluid model, on the other hand, describes the macroscopic quantities obtained by taking average over the velocity space. The fluid equations are obtained by taking moments of the kinetic equation. Because the fluid model only treats the averaged quantities, the computational cost is remarkably lower than the kinetic model. In the fluid model, however, there is always a problem of closure of the higher moment and some physical models are required by considering the kinetic effects.

In the SOL-DIV plasma code packages, the plasma is generally treated with fluid models than kinetic models like B2 code [27] in SOLPS and SOLDOR code [28] in SONIC. Neutrals are mainly described by kinetic models like EIRENE code [29] in SOLPS and NEUT2D code [28] in SONIC while fluid models are also used in some code packages like UEDGE. Impurities are treated with both kinetic (like IMPMC code [30] in SONIC) and fluid models. In the SOL-DIV

simulations of tokamaks, at least two-dimensional (2D) models are used by assuming the toroidal symmetry.

For prediction of ITER SOL-DIV plasma, SOLPS-ITER code package has been developed recently by coupling the plasma fluid code B2.5 and EIRENE code [31]. As for DEMO, simulations on advanced divertors which are designed in order to reduce the divertor heat load from the geometrical aspect such as long-leg divertor [32], super-X divertor [33] and snowflake divertor [34] has been conducted by using code packages.

## 1.5 Treatment of the sheath region in the plasma fluid model

In front of the divertor plate, a thin region called sheath is formed where the charge neutrality, which is the nature of the plasma, does not hold. In the case of tokamak, where the magnetic field intersects the divertor plate at an oblique angle, the thickness of the sheath (magnetic presheath) is the order of the Larmor radius of ion [35]. In this sheath region, the distribution functions of the ion and electron are considered to be too far from the Maxwellian and the fluid model can no longer be applied there. Thus, in the SOL-DIV plasma fluid simulations, boundary conditions at the sheath entrance are imposed instead of solving the sheath region. These boundary conditions are obtained from the analysis of the sheath [15] or the results of kinetic simulations [36]. One of the boundary conditions known as the Bohm criterion is that the Mach number at the sheath entrance should become equal to or larger than unity. This is derived from the condition that the profile of electric potential as the solution of Poisson equation is not oscillatory. Another boundary conditions are on the fraction of the conductive heat flux to the total for ion and electron. These are derived from the wall potential which is determined by the no plasma current condition.

For the plasma fluid model, equations derived by Braginskii [37] are generally used in the SOL-DIV code packages. Since the parallel momentum transport equation is the second-order difference, the Mach number at the sheath entrance is required to be given as the boundary condition. In many simulations, therefore, the Mach at the sheath entrance is set to be unity based on the Bohm criterion.

## 1.6 Validation of SOL-DIV plasma code packages

In parallel with the prediction studies mentioned in Sec. 1.4, validation of the SOL-DIV plasma code packages has been conducted. The basic way is to compare the relation between the particle flux to the divertor plate and the density at the core or the separatrix. Results of the code packages, however, do not satisfactorily agree

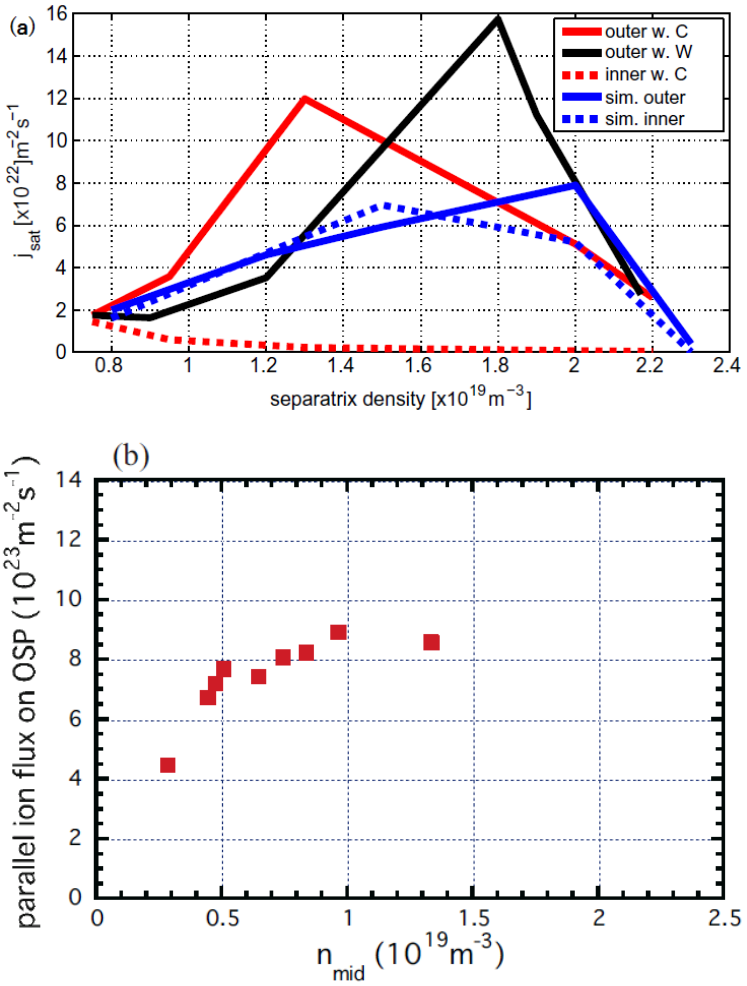


Figure 4 (a) Comparison of simulated ion saturation current with experiment as functions of separatrix density in ASDEX-Upgrade by SOLPS [20]. (b) Simulated parallel ion flux as a function of midplane density in JT-60U by SONIC [38].

with those of experimental measurements. Figure 4 (a) shows the comparison of simulated ion saturation current with experiment in ASDEX-Upgrade by using SOLPS [20]. Although simulation result successfully reproduces the roll-over in high separatrix density regime, in-out asymmetry is not satisfactorily reproduced. In Fig. 4 (b), simulated parallel ion flux in JT-60U by using SONIC is shown. The parallel ion flux saturates at the midplane density of $1\times10^{19}$ /$m^3$, but the significant reduction in the detached plasma regime is not seen.

Efforts have been made to resolve this issue from various aspects. For example, from a comparison of simulation by SOLPS and experiment in ASDEX-Upgrade, it is pointed out that the discrepancy could be attributed to insufficient neutral

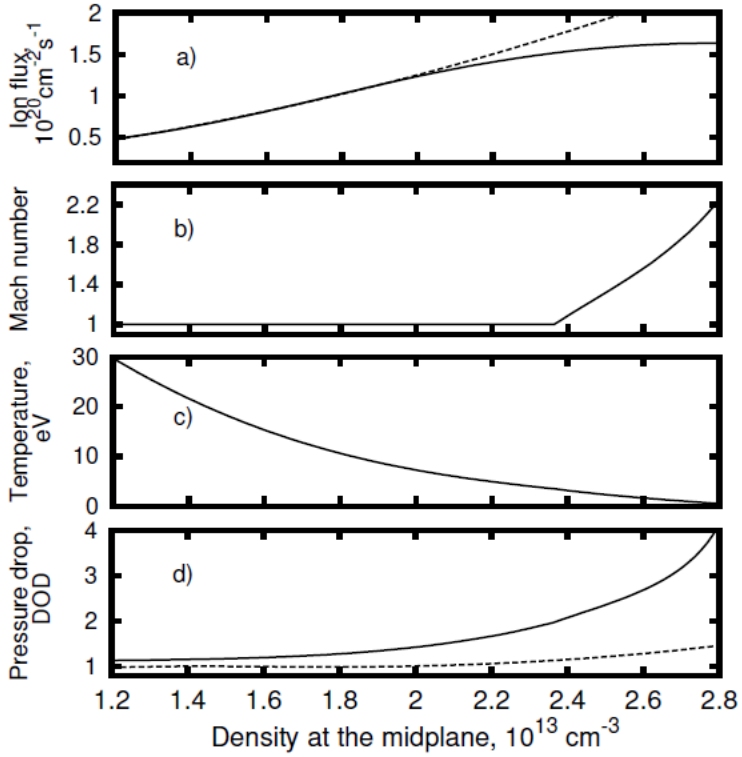


Figure 5 Dependencies of the plasma parameters at the target plate on the upstream density: a) ion flux $j_t = n_t c_{st} M_t$ (solid line), extrapolated flux from the high-recycling regime $j_t^a$ (dashed-line); b)Mach number; c) plasma temperature; d) drop in the total pressure - $p_u/p_t$ (solid line) and degree of detachment (dashed line) [39].

model, plasma fluctuations and non-local kinetic effect on parallel heat transport in Ref. [40]. It is reported that the effects of cross field drifts and enhanced chemical sputtering applied to UEDGE improved the simulation results compared with experiments in ASDEX-Upgrade, JET and DIII-D [41]. In Ref. [38, 42], the effects of low chemical sputtering, wall pumping and supersonic flow on the particle flux to the divertor plate are investigated by SONIC.

## 1.7 One-dimensional simulation codes

SOL-DIV plasma code packages are the main tools to predict the divertor performance of the future devices. Meanwhile, one-dimensional (1D) codes still have some advantages in order to investigate the effects which are not yet considered in the code packages because they are much simpler and their

computational times are much shorter than the code packages. For example, the stability of detached plasma was studied by a 1D code and the unstable radiation front moving from DIV to X-point was found in Ref. [43]. It is reported in Ref. [44] that the cross field transport stabilizes the radiation front. In Ref. [39], supersonic flow in DIV was observed and it reduces the particle flux to the divertor plate compared to the sonic flow case as shown in Fig. 5. In this code, by using the inviscid approximation, the boundary condition at the sheath entrance, i.e., the Mach number of unity, becomes unnecessary.

## 1.8 Motivation of our work

We focus on the SOL-DIV plasma fluid model in order to resolve the problem of the discrepancy between the results of simulations and experiments. As is mentioned in Sec. 1.5, plasma fluid equations derived by Braginskii [37] are generally applied in the SOL-DIV code packages. In the derivation of fluid equations, it is assumed that the collisionality of the plasma is high enough for the temperature to be isotropic. Under this assumption, the ion stress tensor which reflects the effect of ion pressure anisotropy is approximated as the parallel ion viscous flux. The parallel momentum transport equation, therefore, becomes the second-order differential. From the numerical stability point of view, the second-order differential equations are solved more stably than the first-order ones. Instead, the Mach number at the sheath entrance must be given as a boundary condition.

Meanwhile, generalized plasma fluid equations which directly introduces the temperature anisotropy have been proposed [45, 46] but not yet been applied to SOL-DIV plasma fluid code. Because the parallel momentum transport equation becomes the first-order differential, the Mach number at the sheath entrance is determined self-consistently by the upstream condition. Therefore, the Mach number at the sheath entrance is no longer fixed but should be floating. One of the reasons why the generalized plasma fluid model has not yet been applied to SOL-DIV plasma fluid code is probably due to this difficulty of the treatment of the boundary condition at the sheath entrance. We have been developing a virtual divertor (VD) model in order to resolve the difficulty of sheath boundary conditions [47]. In this model, based on a simple idea that the divertor plate is a pure plasma particle sink, an artificial region is set beyond the sheath entrance with artificial sinks for the plasma particle, momentum and energy.

The purpose of our work is to show the physical importance of introducing the temperature anisotropy into the SOL-DIV plasma fluid model, so that this will be the standard in the SOL-DIV plasma code packages. We developed a 1D SOL-

DIV plasma fluid code which introduces the ion temperature anisotropy. The VD model is also incorporated for the sheath boundary conditions.

## 1.9 Outline

The numerical model for the plasma and the virtual divertor (VD) model is explained in Chapter 2. The validity of the VD model is shown in Chapter 3 with some preliminary results by using the plasma fluid model. In Chapter 4, the numerical model for the neutrals which works with the VD model is described with the validity of the VD model and some preliminary results related to the effect of neutrals. As an application of our code, we reproduced the detached plasmas and the effect of radial diffusive loss of particle and heat on the particle flux to the divertor plate was investigated in Chapter 5. Conclusion is presented in Chapter 6.

# Chapter 2
# Numerical Model for Plasma and Virtual Divertor Model

## 2.1 Fluid equations for plasma

In the conventional SOL-DIV simulations [22, 23, 25, 26], a set of fluid equations, the ion continuity, the parallel momentum transport for plasma, the ion energy transport and the electron energy transport, are solved for the plasma density $n$, the parallel flow velocity of the plasma $V$, the ion temperature $T_\mathrm{i}$ and the electron temperature $T_\mathrm{e}$. These equations were derived by taking the zeroth, the first and the second moment of the Boltzmann equation [37]. Here, the temperatures were assumed to be almost isotropic. It was pointed out by kinetic simulations, however, that the ion temperature would not always be isotropic in the SOL-DIV plasmas [48, 49]. In addition, the assumption of isotropic ion temperature requires some physical models. For example, the ion stress tensor $\pi_\mathrm{i}$, which is defined as

$$\pi_\mathrm{i} \equiv \frac{2n\left(T_{\mathrm{i},//} - T_{\mathrm{i},\perp}\right)}{3} \tag{2.1}$$

in terms of the ion temperature of parallel and perpendicular components to the magnetic field, $T_{\mathrm{i},//}$ and $T_{\mathrm{i},\perp}$, is approximated as a parallel ion viscous flux [15],

$$\pi_\mathrm{i} \approx -\eta_\mathrm{i} \frac{\partial V}{\partial s}, \tag{2.2}$$

where $\eta_\mathrm{i}$ is the parallel ion viscosity and $s$ is the coordinate in the parallel direction to the magnetic field. Due to the introduction of parallel ion viscosity term, which is the second-order derivative in space, to the parallel momentum transport equation, the Mach number at the sheath entrance $M_\mathrm{t}$ must be given as a boundary condition.

In our simulation code, on the other hand, the ion temperature of parallel and perpendicular components to the magnetic field, $T_{\mathrm{i},//}$ and $T_{\mathrm{i},\perp}$, are directly introduced to the plasma fluid model while electron temperature $T_\mathrm{e}$ is assumed to

be isotropic because of its fast collisional relaxation.

The 1D plasma fluid equations solved in our simulation code are derived from the parallel component of the Boltzmann equation by assuming that the magnetic field is uniform for simplicity as follows [47];

$$\frac{\partial n}{\partial t}+\frac{\partial}{\partial s}(nV)=S, \tag{2.3}$$

$$\frac{\partial}{\partial t}(m_{\mathrm{i}}nV)+\frac{\partial}{\partial s}\left(m_{\mathrm{i}}nV^{2}+nT_{\mathrm{i},//}+nT_{\mathrm{e}}\right)=M_{\mathrm{m}}, \tag{2.4}$$

$$\begin{aligned}&\frac{\partial}{\partial t}\left(\frac{1}{2}m_{\mathrm{i}}nV^{2}+\frac{1}{2}nT_{\mathrm{i},//}\right)+\frac{\partial}{\partial s}\left(\frac{1}{2}m_{\mathrm{i}}nV^{3}+\frac{3}{2}nT_{\mathrm{i},//}V+q_{\mathrm{i},//}\right)\\&=Q_{\mathrm{i},//}+\frac{n\left(T_{\mathrm{i},\perp}-T_{\mathrm{i},//}\right)}{\tau_{\mathrm{rlx}}}+\frac{m_{\mathrm{e}}}{m_{\mathrm{i}}}\frac{n\left(T_{\mathrm{e}}-T_{\mathrm{i},//}\right)}{\tau_{\mathrm{e}}}-V\frac{\partial}{\partial s}(nT_{\mathrm{e}}),\end{aligned} \tag{2.5}$$

$$\frac{\partial}{\partial t}\left(nT_{\mathrm{i},\perp}\right)+\frac{\partial}{\partial s}\left(nT_{\mathrm{i},\perp}V+q_{\mathrm{i},\perp}\right)=Q_{\mathrm{i},\perp}-\frac{n\left(T_{\mathrm{i},\perp}-T_{\mathrm{i},//}\right)}{\tau_{\mathrm{rlx}}}+\frac{2m_{\mathrm{e}}}{m_{\mathrm{i}}}\frac{n\left(T_{\mathrm{e}}-T_{\mathrm{i},\perp}\right)}{\tau_{\mathrm{e}}}, \tag{2.6}$$

$$\frac{\partial}{\partial t}\left(\frac{3}{2}nT_{\mathrm{e}}\right)+\frac{\partial}{\partial s}\left(\frac{5}{2}nT_{\mathrm{e}}V+q_{\mathrm{e}}\right)=Q_{\mathrm{e}}-\frac{3m_{\mathrm{e}}}{m_{\mathrm{i}}}\frac{n\left(T_{\mathrm{e}}-T_{\mathrm{i}}\right)}{\tau_{\mathrm{e}}}+V\frac{\partial}{\partial s}(nT_{\mathrm{e}}). \tag{2.7}$$

The detail of the derivation of these equations is described in Appendix A.1. Here, $t$ represents the time. The mass is denoted by $m$. The subscripts "i" and "e" correspond to the ion and electron, and "//" and " $\perp$ " to the parallel and perpendicular component to the magnetic field, respectively. The effective isotropic ion temperature is defined as

$$T_{\mathrm{i}}\equiv\frac{T_{\mathrm{i},//}+2T_{\mathrm{i},\perp}}{3}. \tag{2.8}$$

The ion-ion and electron-ion Coulomb collision times, $\tau_{\mathrm{i}}$ and $\tau_{\mathrm{e}}$, are evaluated as follows [50];

$$\tau_{\mathrm{i}}=\frac{12\pi^{3/2}\varepsilon_{0}^{2}\sqrt{m_{\mathrm{i}}}T_{\mathrm{i}}^{3/2}}{Z_{\mathrm{eff}}^{4}e^{4}n\ln\Lambda}, \tag{2.9}$$

$$\tau_{\mathrm{e}}=\frac{6\sqrt{2}\pi^{3/2}\varepsilon_{0}^{2}\sqrt{m_{\mathrm{e}}}T_{\mathrm{e}}^{3/2}}{Z_{\mathrm{eff}}^{2}e^{4}n\ln\Lambda}, \tag{2.10}$$

where $\varepsilon_0$ and $e$ are the electric permittivity of vacuum and elementary charge, respectively. The effective ion charge is denoted by $Z_{\mathrm{eff}}$ which is an input

parameter in our code. The Coulomb logarithm is given as follows [51];

$$\ln\Lambda = 29.3 - \frac{1}{2}\ln n\left[/\,\mathrm{m}^3\right] + \frac{3}{2}\ln T_\mathrm{e}\left[\mathrm{eV}\right]. \tag{2.11}$$

The ion temperature relaxation time is given as follows [45, 46];

$$\tau_\mathrm{rlx} = 2.5\tau_\mathrm{i}. \tag{2.12}$$

In order to consider the kinetic effect, the conductive heat flux $q$ is estimated by harmonic average of the Spitzer-Härm (SH) heat flux $q^\mathrm{SH}$ and the free streaming (FS) heat flux $q^\mathrm{FS}$ [49] as

$$q = \left(\frac{1}{q^\mathrm{SH}} + \frac{1}{\alpha q^\mathrm{FS}}\right)^{-1}. \tag{2.13}$$

The SH heat fluxes $q^\mathrm{SH}$ are estimated as follows;

$$q_{\mathrm{i},/\!/}^\mathrm{SH} = -c\kappa_\mathrm{i}^\mathrm{SH}\frac{\partial T_{\mathrm{i},/\!/}}{\partial s}, \tag{2.14}$$

$$q_{\mathrm{i},\perp}^\mathrm{SH} = -(1-c)\kappa_\mathrm{i}^\mathrm{SH}\frac{\partial T_{\mathrm{i},\perp}}{\partial s}, \tag{2.15}$$

$$q_\mathrm{e}^\mathrm{SH} = -\kappa_\mathrm{e}^\mathrm{SH}\frac{\partial T_\mathrm{e}}{\partial s}. \tag{2.16}$$

Here, the coefficient $c$, which remains as an ambiguity and is fixed to be $c = 0.5$, determines the fraction of the SH conductive heat fluxes for $T_{\mathrm{i},/\!/}$ and $T_{\mathrm{i},\perp}$. The parallel heat conductivities of the ion and electron are given as follows [50];

$$\kappa_\mathrm{i}^\mathrm{SH} = 3.9\frac{n\tau_\mathrm{i}T_{\mathrm{i},/\!/}}{m_\mathrm{i}}, \tag{2.17}$$

$$\kappa_\mathrm{e}^\mathrm{SH} = 3.16\frac{n\tau_\mathrm{e}T_\mathrm{e}}{m_\mathrm{e}}. \tag{2.18}$$

The FS heat fluxes $q^\mathrm{FS}$ are estimated as follows [49];

$$q_{\mathrm{i},/\!/}^\mathrm{FS} = nT_{\mathrm{i},/\!/}\sqrt{\frac{T_{\mathrm{i},/\!/}}{m_\mathrm{i}}}, \tag{2.19}$$

$$q_{\mathrm{i},\perp}^{\mathrm{FS}} = nT_{\mathrm{i},\perp}\sqrt{\frac{T_{\mathrm{i},//}}{m_{\mathrm{i}}}}, \tag{2.20}$$

$$q_{\mathrm{e}}^{\mathrm{FS}} = nT_{\mathrm{e}}\sqrt{\frac{T_{\mathrm{e}}}{m_{\mathrm{e}}}}. \tag{2.21}$$

Thus, the effective parallel heat conductivities are evaluated as follows;

$$\kappa_{\mathrm{i},//}^{\mathrm{eff}} = \frac{c\kappa_{\mathrm{i}}^{\mathrm{SH}}}{1+\dfrac{q_{\mathrm{i},//}^{\mathrm{SH}}}{\alpha_{\mathrm{i},//}q_{\mathrm{i},//}^{\mathrm{FS}}}}, \tag{2.22}$$

$$\kappa_{\mathrm{i},\perp}^{\mathrm{eff}} = \frac{(1-c)\kappa_{\mathrm{i}}^{\mathrm{SH}}}{1+\dfrac{q_{\mathrm{i},\perp}^{\mathrm{SH}}}{\alpha_{\mathrm{i},\perp}q_{\mathrm{i},\perp}^{\mathrm{FS}}}}, \tag{2.23}$$

$$\kappa_{\mathrm{e}}^{\mathrm{eff}} = \frac{\kappa_{\mathrm{e}}^{\mathrm{SH}}}{1+\dfrac{q_{\mathrm{e}}^{\mathrm{SH}}}{\alpha_{\mathrm{e}}q_{\mathrm{e}}^{\mathrm{FS}}}}. \tag{2.24}$$

The flux-limiting factor is denoted by $\alpha$. Here, we use $\alpha_{\mathrm{i},//} = \alpha_{\mathrm{i},\perp} = 0.5$ and $\alpha_{\mathrm{e}} = 0.2$, respectively [46]. In Eqs. (2.3)-(2.7), the notations $S$, $M_{\mathrm{m}}$ and $Q$ represent the source terms for particle, momentum and energy, respectively. The term $V(\partial(nT_{\mathrm{e}})/\partial s)$ in Eqs. (2.5) and (2.7) is the replacement of the force term due to electric field and thermal force term by using the following generalized Ohm's law with the assumption of no net plasma current;

$$\frac{\mathrm{d}}{\mathrm{d}s}(nT_{\mathrm{e}}) + eEn = -R_T, \tag{2.25}$$

where $E$ is the parallel electric field and $R_T$ denotes the thermal force. The sound speed is defined as follows;

$$c_{\mathrm{s}} = \sqrt{\frac{T_{\mathrm{e}}+T_{\mathrm{i},//}}{m_{\mathrm{i}}}}. \tag{2.26}$$

The Mach number is defined as $M = V/c_{\mathrm{s}}$. Especially, near the sheath entrance, due to the large gradient of the ion temperature, we use the following definition of adiabatic sound speed;

$$c_{\mathrm{s}}^{*}=\sqrt{\frac{T_{\mathrm{e}}+\gamma_{\mathrm{A}}T_{\mathrm{i},//}}{m_{\mathrm{i}}}}, \tag{2.27}$$

where the adiabatic index $\gamma_{\mathrm{A}}$ is defined as follows;

$$\frac{\mathrm{d}}{\mathrm{d}s}\left(nT_{\mathrm{i},//}\right)=\gamma_{\mathrm{A}}T_{\mathrm{i},//}\frac{\mathrm{d}n}{\mathrm{d}s}. \tag{2.28}$$

Near the sheath entrance, the plasma flow becomes 1D and adiabatic with no coupling of parallel and perpendicular pressures, so that $\gamma_{\mathrm{A}} = 3$ is used [15]. Then, the Mach number at the sheath entrance is evaluated by $M^{*} = V/c_{\mathrm{s}}^{*}$.

We briefly discuss here the relationship between the plasma fluid model described above and the conventional one. If we focus on the parallel momentum transport equation, Eq. (2.4), the effective isotropic ion pressure, $nT_{\mathrm{i}}$, and the parallel ion viscous flux, $-\eta_{\mathrm{i}}(\partial V/\partial s)$, in the conventional equation,

$$\frac{\partial}{\partial t}\left(m_{\mathrm{i}}nV\right)+\frac{\partial}{\partial s}\left(m_{\mathrm{i}}nV^{2}+nT_{\mathrm{i}}+nT_{\mathrm{e}}\right)+\frac{\partial}{\partial s}\left(-\eta_{\mathrm{i}}\frac{\partial V}{\partial s}\right)=M_{\mathrm{m}}, \tag{2.29}$$

is replaced by parallel ion pressure, $nT_{\mathrm{i},//}$. As is discussed above, the parallel ion viscous flux, Eq. (2.2), is the approximated form of the ion stress tensor $\pi_{\mathrm{i}}$, Eq. (2.1), so that the summation of $nT_{\mathrm{i}} \equiv n(T_{\mathrm{i},//} + 2T_{\mathrm{i},\perp})/3$ and $\pi_{\mathrm{i}} \equiv 2n(T_{\mathrm{i},//} - T_{\mathrm{i},\perp})/3$ becomes $nT_{\mathrm{i},//}$. Therefore, these two equations are consistent. When we focus on Eqs. (2.5) and (2.6), the conventional ion energy transport equation for the effective isotropic ion temperature, $T_{\mathrm{i}}$,

$$\begin{aligned}&\frac{\partial}{\partial t}\left(\frac{1}{2}m_{\mathrm{i}}nV^{2}+\frac{3}{2}nT_{\mathrm{i}}\right)+\frac{\partial}{\partial s}\left(\frac{1}{2}m_{\mathrm{i}}nV^{3}+\frac{5}{2}nT_{\mathrm{i}}V+q_{\mathrm{i}}\right)\\&=Q_{\mathrm{i}}-\frac{\partial}{\partial s}\left(-\eta_{\mathrm{i}}\frac{\partial V}{\partial s}\right)V+\frac{3m_{\mathrm{e}}}{m_{\mathrm{i}}}\frac{n\left(T_{\mathrm{e}}-T_{\mathrm{i}}\right)}{\tau_{\mathrm{e}}}-V\frac{\partial}{\partial s}\left(nT_{\mathrm{e}}\right),\end{aligned} \tag{2.30}$$

is divided into the parallel and perpendicular components. If the ion temperature is almost isotropic, $T_{\mathrm{i},//} \approx T_{\mathrm{i},\perp} \approx T_{\mathrm{i}}$, the summation of Eqs. (2.5) and (2.6) becomes Eq. (2.30) by defining $q_{\mathrm{i}}$ and $Q_{\mathrm{i}}$ as $q_{\mathrm{i}} \equiv -\kappa_{\mathrm{i}}^{\mathrm{SH}}(\partial T_{\mathrm{i}}/\partial s)$ and $Q_{\mathrm{i}} \equiv Q_{\mathrm{i},//} + Q_{\mathrm{i},\perp}$. Equations (2.29) and (2.30) are the famous Braginskii equations [37] which have been employed in many SOL-DIV plasma fluid simulation codes. Nevertheless, we employ Eqs. (2.4)-(2.6) instead of Eqs (2.29) and (2.30) in order to treat the ion temperature anisotropy accurately and to eliminate the boundary condition for $M_{\mathrm{t}}$.

Figure 6 shows a schematic picture of the 1D SOL-DIV system. Here, we assume that the magnetic field is uniform and that the inner and outer SOL-DIV system is symmetric for simplicity. In the SOL, the particle and heat fluxes from

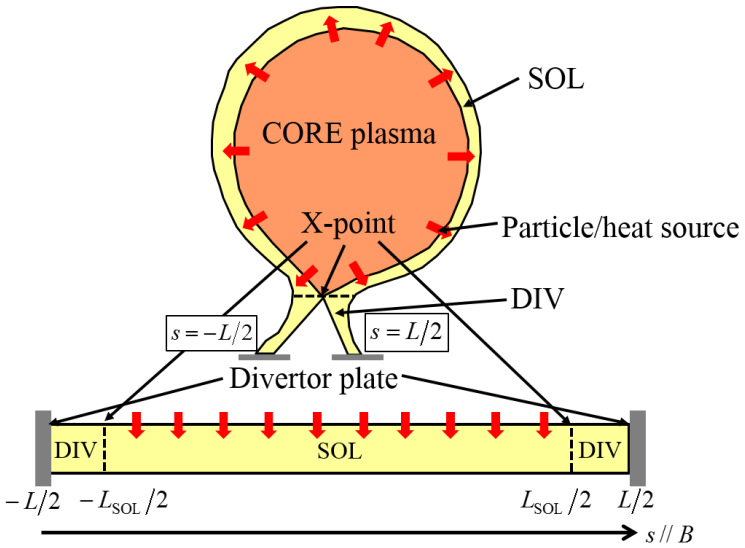


Figure 6 Schematic picture of the 1D SOL-DIV system.

the core plasma, $\Gamma_{\mathrm{sep}}$ and $P_{\mathrm{sep}}$, are distributed uniformly. The particle and heat source terms in the SOL are given as follows;

$$S^{\mathrm{core}} = \frac{\Gamma_{\mathrm{sep}}}{V_{\mathrm{SOL}}} H\left(\frac{L_{\mathrm{SOL}}}{2} - |s|\right), \tag{2.31}$$

$$Q_{\mathrm{i},/\!/}^{\mathrm{core}} = \frac{1}{6}\frac{P_{\mathrm{sep}}}{V_{\mathrm{SOL}}} H\left(\frac{L_{\mathrm{SOL}}}{2} - |s|\right), \tag{2.32}$$

$$Q_{\mathrm{i},\perp}^{\mathrm{core}} = \frac{1}{3}\frac{P_{\mathrm{sep}}}{V_{\mathrm{SOL}}} H\left(\frac{L_{\mathrm{SOL}}}{2} - |s|\right), \tag{2.33}$$

$$Q_{\mathrm{e}}^{\mathrm{core}} = \frac{1}{2}\frac{P_{\mathrm{sep}}}{V_{\mathrm{SOL}}} H\left(\frac{L_{\mathrm{SOL}}}{2} - |s|\right). \tag{2.34}$$

Here, the volume of the SOL is defined as $V_{\mathrm{SOL}} \equiv A_{\mathrm{sep}} d_{\mathrm{SOL}}$ in terms of the separatrix area $A_{\mathrm{sep}}$ and the radial width of the flux tube in the SOL region $d_{\mathrm{SOL}}$, which is assumed to be uniform. The Heaviside step function is denoted by $H$. The parallel length of the SOL is denoted by $L_{\mathrm{SOL}}$ and the origin of the coordinate $s$ is set at the center of the SOL which is always the stagnation point in the in-out symmetric condition.

## 2.2 Virtual divertor model

The boundary conditions at the sheath entrance requires quite delicate treatments. As is well known, the sheath theory imposes the following physical boundary

conditions; (a) the Mach number $M_t$ is equal or larger than unity, $M_t \geq 1$ (so called Bohm criterion), and (b) the ion and electron heat fluxes are given by $\gamma_i n T_i V$ and $\gamma_e n T_e V$, respectively, where the sheath heat transmission factors, $\gamma_i$ and $\gamma_e$, depend on the sheath potential [15]. As is reviewed briefly in the previous section, the parallel momentum transport is described by the second-order differential equation in the conventional SOL-DIV plasma fluid code. Thus, $M_t$ is given as the boundary condition like $M_t = 1$ based on the Bohm criterion. But this treatment is not necessarily self-consistent. In our code, on the other hand, the first-order differential parallel momentum transport equation is used, so that $M_t$ is determined self-consistently only by the upstream condition in principle. This one-way nature of the first-order differential equations matches our image of the way the flow velocity is determined. For example, the flow velocity just in front of a waterfall does not depend on the scale of it but only on the upstream conditions. On the other hand, because the energy transport equations, Eqs. (2.5)-(2.7), are the second-order differential, the sheath transmission factors should be given in order to determine the temperature profiles consistently.

In order to satisfy these boundary conditions at the sheath entrance, we have developed and incorporated a virtual divertor (VD) model in our code. The concept of this VD model is similar to the penalization scheme [52] which has been developed in the fluid mechanics for the simulations with obstacles and is adopted in some edge plasma modeling [53, 54, 55]. In the penalization scheme, the computational domain is set even on the inside of the obstacles instead of imposing boundary conditions at the surfaces of them. For the case of the plasma, the obstacles, like limiters and divertor plates, work as pure sinks for particles. Based on this idea, the penalization terms are set on the inside of the obstacles, so that the particle density $n$ and the particle flux $\Gamma \equiv nV$ become zero there. It is shown in the isothermal case that the Bohm condition ($M_t = 1$) is satisfied at the limiter surface with the penalization scheme [53]. In Ref. [54], an extended penalization scheme is applied to the non-isothermal 1D plasma fluid model for a limiter configuration. The normalized equations including the penalization terms are as follows;

$$\frac{\partial n}{\partial t} + \frac{\partial \Gamma}{\partial s} + \frac{\chi}{\eta_n}\left(n - n_\Omega\right) = S, \tag{2.35}$$

$$\frac{\partial \Gamma}{\partial t} + \frac{\partial}{\partial s}\left(\frac{\Gamma^2}{n} + n\left(T_i + T_e\right)\right) + \frac{\chi}{\eta_\Gamma}\left(\Gamma - \Gamma_\Omega\right) = 0, \tag{2.36}$$

$$\frac{\partial T_i}{\partial t} + \frac{\chi_1}{\eta_T}\left(\frac{\partial T_i}{\partial s} - G_i\right) - \frac{\chi_2}{\eta_T}\left(\frac{\partial T_i}{\partial s} - G_i\right) + \frac{\chi}{\eta_T}\left(T_i - T_\Omega\right) = \mathrm{RHS}_{T_i}, \tag{2.37}$$

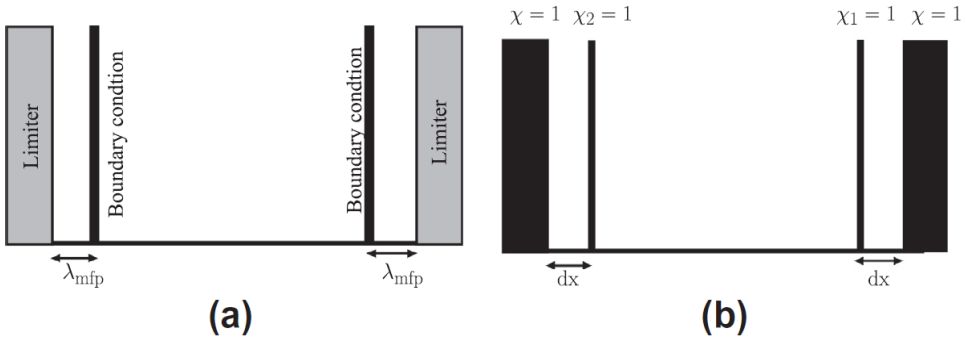


Figure 7 (a) Schematic representation of the plasma domain showing the non-collisional region of length $\lambda_{mfp}$, (b) mask function $\chi$ describing the limiter geometry and mask functions $\chi_1$ et $\chi_2$ pointing out the place where the heat flux becomes entirely advective [54].

$$\frac{\partial T_e}{\partial t} + \frac{\chi_1}{\eta_T}\left(\frac{\partial T_e}{\partial s} - G_e\right) - \frac{\chi_2}{\eta_T}\left(\frac{\partial T_e}{\partial s} - G_e\right) + \frac{\chi}{\eta_T}\left(T_e - T_\Omega\right) = \mathrm{RHS}_{T_e}. \tag{2.38}$$

Here, $\chi$, $\chi_1$ and $\chi_2$ are the mask functions carrying the information of limiter configuration. As shown in Fig. 7, which corresponds to Fig. 3 in Ref. [54], $\chi$, $\chi_1$ and $\chi_2$ are zero except for the inside of the limiter and at the sheath entrances, respectively, where these become one. The terms with these mask functions are called the penalization terms which force the plasma parameters $\varphi$ to $\varphi_\Omega$ in the obstacles. The notation $G$ is defined as $G \equiv -(\gamma - 5/2)T\Gamma/\kappa$ which is used to force the temperature gradient to that determined by the sheath heat transmission factor $\gamma$. The penalization parameters, $\eta_n$, $\eta_\Gamma$ and $\eta_T$, must be small enough (<< 1). This extended penalization scheme is applied to the SOLEDGE2D code and used for the divertor configurations, too [55].

In the VD model, like the penalization scheme, we set artificial regions beyond the sheath entrance, as shown in Fig. 8. We call this region a virtual divertor (VD) region hereafter. In the VD region, just like the penalization terms, we set artificial sink terms according to the image of a waterfall as follows [47];

$$S^{\mathrm{VD}} = -\frac{n}{\tau^{\mathrm{VD}}}, \tag{2.39}$$

$$M_{\mathrm{m}}^{\mathrm{VD}} = -\frac{m_{\mathrm{i}} n V}{\tau^{\mathrm{VD}}} + \frac{\partial}{\partial s}\left(m_{\mathrm{i}} n D_{\mathrm{m}}^{\mathrm{VD}} \frac{\partial V}{\partial s}\right), \tag{2.40}$$

$$Q_{\mathrm{i},//}^{\mathrm{VD}} = -\frac{1}{\tau^{\mathrm{VD}}}\left(\frac{1}{2} m_{\mathrm{i}} n V^2 + \frac{g_{\mathrm{i},//}^{\mathrm{VD}}}{2} n T_{\mathrm{i},//}\right), \tag{2.41}$$

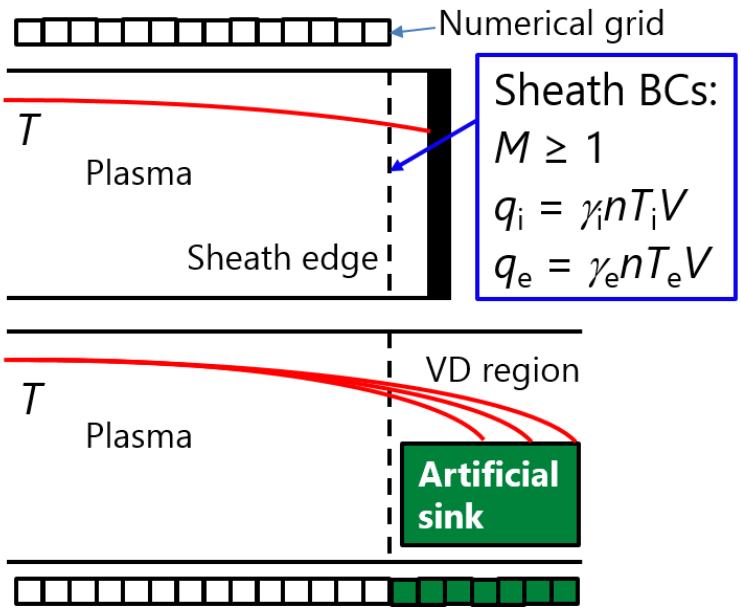


Figure 8 Schematic picture of the basic concept of a virtual divertor (VD) model. The VD regions have artificial sink terms for particle, momentum and energy in order to represent the effects of the sheath region and the divertor plate.

$$Q_{i,\perp}^{VD} = -\frac{g_{i,\perp}^{VD} n T_{i,\perp}}{\tau^{VD}}, \tag{2.42}$$

$$Q_e^{VD} = -\frac{1}{\tau^{VD}}\left( g_e^{VD} \frac{3}{2} n T_e \right). \tag{2.43}$$

Here, the artificial sink terms are introduced with the characteristic decay time denoted by $\tau^{VD}$ in the VD region, which corresponds to the penalization parameters $\eta_n$, $\eta_\Gamma$ and $\eta_T$. Unlike the penalization scheme, the decay times for the momentum and energy are also $\tau^{VD}$ basically, except for the second term of Eq. (2.40) and the effects of the artificial energy sink coefficients $g^{VD}$ in Eqs. (2.41)-(2.43). In that point, the artificial sink terms in the VD model are more intuitive and comprehensive than the penalization terms. The second term of Eq. (2.40) is an artificial viscosity term which is required in order to prevent the flow velocity from diverging in the VD region. This is explained in detail in Appendix A.2. Thanks to this second-order differential artificial viscosity term, we can impose some artificial boundary condition on $V$ at the edge of the system like $V = 0$ ($M = 0$) as shown in Fig. 9, which is necessary in order to make the model tractable numerically. As is described later, the artificial momentum diffusivity $D_m^{VD}$ has non-zero values only at the position far enough from the sheath entrance, so that Eq. (2.4) keeps its nature as the first-order differential equation in the plasma

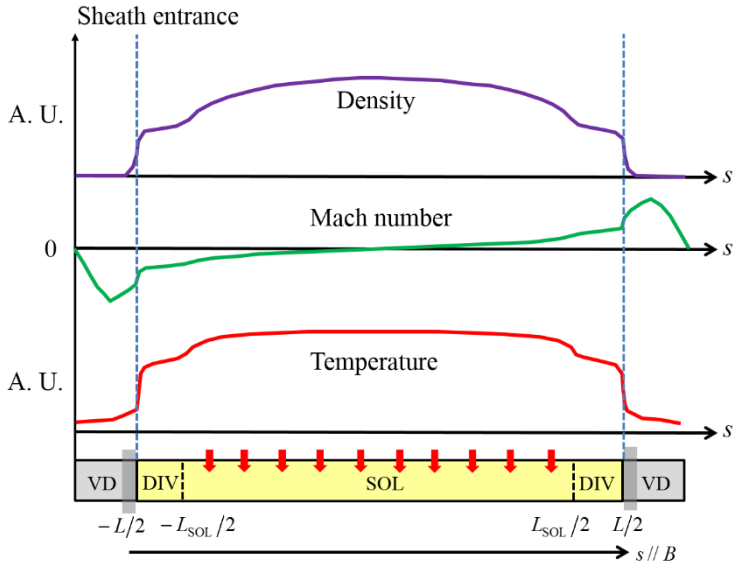


Figure 9 Schematic picture of the SOL-DIV system with VD regions.

region. In addition, by controlling the artificial energy sink coefficients $g^{VD} \geq 1$, the ratio of the conductive heat flux to the convective one can be controlled, so that the sheath heat transmission factors, $\gamma_i$ and $\gamma_e$, satisfy the values given by the sheath theory [15]. The effective heat conductivities $\kappa^{eff}$ in the VD region are given by the values at the sheath entrance in order to insure that the heat fluxes and gradients of the temperatures are continuous there.

There is a problem of numerical boundary conditions at the edge of the system because there is no way to decide them physically. In order to avoid this problem, we connect the two VD regions and use a periodic boundary condition as shown in Fig. 10. This is the same strategy as the penalization scheme. In this case, the effective heat conductivities $\kappa^{eff}$ in the VD region are interpolated by using the values at the sheath entrance in order to deal with asymmetric systems in the future.

By connecting the VD region, one might anticipate that information of the plasma parameters $\varphi$ on the one side of the DIV would numerically affect those on the other side through the VD region. Probably, the same question arises when the penalization scheme is used. To answer this question, we should recall that the plasma parameters described by the first-order differential equations are determined only by the upstream conditions. Because there will be always a point of $V = 0$ in the VD region even in the asymmetric SOL-DIV conditions, the information of the plasma density $n$ and the flow velocity $V$, which are described by the first-order differential equations (2.3) and (2.4) (at least in the plasma region), does not propagate from the one side to the other side of DIV through the VD region. In addition, it seems to be important intuitively that the dumping of $n$ in the VD region is decisively strong in order to model the effects of the sheath

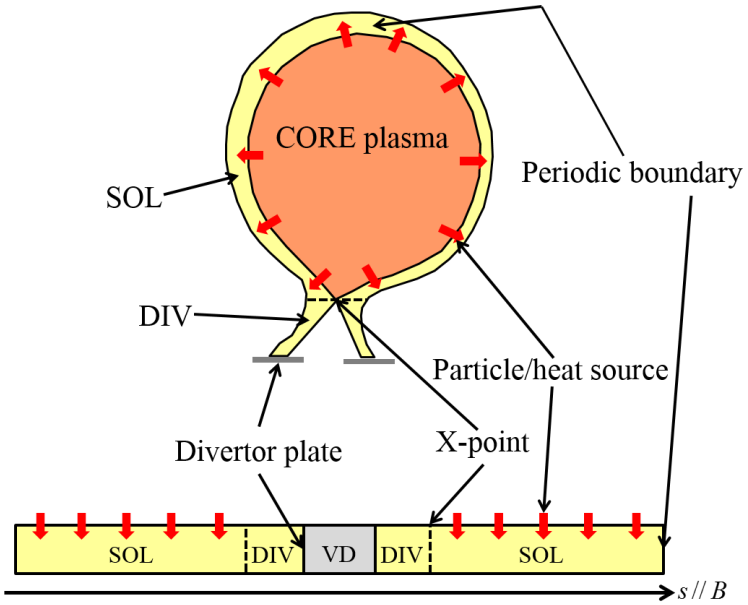


Figure 10 Schematic picture of the connected VD region. By using a periodic boundary condition, the problem of numerical boundary conditions at the edge of the system in Fig. 9 is automatically avoided.

region and divertor plate. As far as this condition is satisfied, the profiles of $n$ and $V$ do not depend on the value of $\tau^{\mathrm{VD}}$ in principle, which is the same nature as the penalization scheme [53]. For the temperatures $T$, the information indeed propagates through the VD region because they are described by the second-order differential equations (2.5)-(2.7). Actually, this does not matter because the values of the sheath heat transmission factors $\gamma$ at the sheath entrance can be controlled by the artificial energy sink coefficients $g^{\mathrm{VD}}$. Like the penalization scheme, profiles in the VD region do not have any physical senses.

By the artificial dumping of the flow velocity $V$ in the center of VD region by the artificial viscosity term in the momentum sink Eq. (2.40), an artificial adiabatic compression is sometimes induced which causes a raise of parallel ion temperature $T_{\mathrm{i},//}$. Therefore, we introduce an additional cooling for parallel ion energy by using the following Gaussian-type $g_{\mathrm{i},//}{}^{\mathrm{VD}}$;

$$g_{\mathrm{i},//}^{\mathrm{VD}} = g_{\mathrm{i},//}^{\mathrm{c,VD}} \exp\left(-\frac{4s'}{L_0^2}\right) + g_{\mathrm{i},//}^{\mathrm{e,VD}}. \tag{2.44}$$

Here, $g_{\mathrm{i},//}{}^{\mathrm{c,VD}} \geq 3$ and $g_{\mathrm{i},//}{}^{\mathrm{e,VD}}$ are the control parameters. The coordinate $s'$ is in the parallel direction to the magnetic field with its origin at the center of the VD region. The notation $L_0$ represents the parallel length of the region for the connection of

the flow velocity $V$ in the VD region. The artificial momentum diffusivity $D_{\mathrm{m}}^{\mathrm{VD}}$ is also given by the Gaussian-type as follows;

$$D_{\mathrm{m}}^{\mathrm{VD}} = c_D \frac{L_0^2}{\tau^{\mathrm{VD}}} \exp\left( -\frac{4s'}{L_0^2} \right). \tag{2.45}$$

Here, the coefficient $c_D$ is set to be 1. The parallel length of the connection region $L_0$ is used again. In the calculations below, $L_0/L^{\mathrm{VD}} = 4/15$ is used where $L^{\mathrm{VD}}$ is the parallel length of the VD region. Thus, the exponential term becomes $\exp(-(L^{\mathrm{VD}}/L_0)^2) \approx 10^{-6}$ at the sheath entrance ($s' = \pm L^{\mathrm{VD}}/2$), so that the artificial viscosity term does not work except for the center of the VD region.

Consequently, the plasma-wall boundary condition can be replaced by the VD model with a periodic boundary condition. Thus, the VD model can make it much easier to treat the complex wall geometry of the real devices. This fact gives us a future prospect to couple a SOL-DIV simulation code with a core plasma simulation code both of which can be treated with a periodic boundary condition.

## 2.3 Numerical scheme

Equations (2.3)-(2.7) are solved one-by-one and self-consistent solutions are obtained iteratively. For simplicity, a uniform staggered grid is used where the grid points for the flow velocity $V$ are located at the cell boundaries. This calculation method is inspired by the B2 code [27] which used the staggered grid in the framework of the SIMPLE method [56]. For the discretization of inertia terms, the full implicit scheme is used. The convection terms and diffusion terms are discretized by the first-order accurate upwind scheme and the second-order accurate central-difference scheme. By using the first-order accurate upwind scheme, numerical instability can be avoided and the matrix of the equation becomes cyclic tridiagonal which can be solved by a direct method which is based on the Sherman-Morrison formula and TriDiagonal Matrix Algorithm (TDMA) [57]. A fluid equation for a physical quantity $\varphi$ with non-periodic boundary conditions is discretized as follows;

$$a_i \varphi_i = b_i \varphi_{i+1} + c_i \varphi_{i-1} + d_i, \quad c_1 = 0, \quad b_N = 0. \tag{2.46}$$

Here, $a$, $b$, $c$ and $d$ are the numerical coefficient and $i = 1, 2, 3, \ldots, N$ is the grid number. Equation (2.46) can be rewritten in terms of a tridiagonal matrix as follows;

$$\begin{pmatrix} a_1 & b_1 & & & & & 0 \\ c_2 & a_2 & b_2 & & & & \\ & \ddots & \ddots & \ddots & & & \\ & & c_i & a_i & b_i & & \\ & & & \ddots & \ddots & \ddots & \\ & & & & c_{N-1} & a_{N-1} & b_{N-1} \\ 0 & & & & & c_N & a_N \end{pmatrix} \begin{pmatrix} \varphi_1 \\ \varphi_2 \\ \vdots \\ \varphi_i \\ \vdots \\ \varphi_{N-1} \\ \varphi_N \end{pmatrix} = \begin{pmatrix} d_1 \\ d_2 \\ \vdots \\ d_i \\ \vdots \\ d_{N-1} \\ d_N \end{pmatrix}. \tag{2.47}$$

As a solver for such tridiagonal matrix equations, TriDiagonal Matrix Algorithm (TDMA) is the fastest direct method [56]. This algorithm proceeds as follows;

1. Calculate $P_1$ and $Q_1$ by using following equation;

$$P_1 = \frac{b_1}{a_1}, \quad Q_1 = \frac{d_1}{a_1}. \tag{2.48}$$

2. Calculate $P_i$ and $Q_i$ for $i$ = 2, 3, …, $N$ by using following recurrence formulas;

$$P_i = \frac{b_i}{a_i - c_i P_{i-1}}, \quad Q_i = \frac{d_i + c_i Q_{i-1}}{a_i - c_i P_{i-1}}. \tag{2.49}$$

3. Set $\varphi_N = Q_N$.
4. Calculate $\varphi_i$ for $i = N$-1, $N$-2, …, 2, 1 by using following recurrence formula;

$$\varphi_i = P_i \varphi_{i+1} + Q_i. \tag{2.50}$$

In case of a periodic boundary condition, the discretized equations become as follows;

$$a_i \varphi_i = \begin{cases} b_i \varphi_{i+1} + c_i \varphi_N + d_i & (i = 1) \\ b_i \varphi_{i+1} + c_i \varphi_{i-1} + d_i, & (2 \le i \le N-1) \\ b_i \varphi_1 + c_i \varphi_{i-1} + d_i & (i = N) \end{cases} \tag{2.51}$$

Equation (2.51) can be rewritten in terms of a cyclic tridiagonal matrix as follows;

$$\begin{pmatrix} a_1 & b_1 & & & & & c_1 \\ c_2 & a_2 & b_2 & & & & \\ & \ddots & \ddots & \ddots & & & \\ & & c_i & a_i & b_i & & \\ & & & \ddots & \ddots & \ddots & \\ & & & & c_{N-1} & a_{N-1} & b_{N-1} \\ b_N & & & & & c_N & a_N \end{pmatrix} \begin{pmatrix} \varphi_1 \\ \varphi_2 \\ \vdots \\ \varphi_i \\ \vdots \\ \varphi_{N-1} \\ \varphi_N \end{pmatrix} = \begin{pmatrix} d_1 \\ d_2 \\ \vdots \\ d_i \\ \vdots \\ d_{N-1} \\ d_N \end{pmatrix}. \tag{2.52}$$

A cyclic tridiagonal matrix equation boils down to the problem of solving two tridiagonal matrix equations by using Sherman-Morrison formula on a square matrix A as follows;

$$\left(\mathrm{A} + \boldsymbol{uv}\right)^{-1} = \mathrm{A}^{-1} - \mathrm{A}^{-1}\boldsymbol{u}\left(1 + \boldsymbol{v}\cdot\mathrm{A}^{-1}\boldsymbol{u}\right)^{-1}\boldsymbol{v}\mathrm{A}^{-1}. \tag{2.53}$$

The cyclic tridiagonal matrix G in Eq. (2.52) can be expressed as G = A + $\boldsymbol{uv}$ in terms of a tridiagonal matrix A and vectors $\boldsymbol{u}$ and $\boldsymbol{v}$ as follows;

$$A = \begin{pmatrix} a_1 - c_1 & b_1 & & & & & 0 \\ c_2 & a_2 & b_2 & & & & \\ & \ddots & \ddots & \ddots & & & \\ & & c_i & a_i & b_i & & \\ & & & \ddots & \ddots & \ddots & \\ & & & & c_{N-1} & a_{N-1} & b_{N-1} \\ 0 & & & & & c_N & a_N - b_N \end{pmatrix}, \tag{2.54}$$

$$\boldsymbol{u} = \begin{pmatrix} c_1 \\ 0 \\ \vdots \\ 0 \\ \vdots \\ 0 \\ b_N \end{pmatrix}, \quad \boldsymbol{v} = \begin{pmatrix} 1 \\ 0 \\ \vdots \\ 0 \\ \vdots \\ 0 \\ 1 \end{pmatrix}. \tag{2.55}$$

Thus, G$\boldsymbol{\varphi}$ = $\boldsymbol{d}$, Eq. (2.52), can be solved as follows;

$$\boldsymbol{\varphi} = \mathrm{G}^{-1}\boldsymbol{d} = \left(\mathrm{I} - \frac{\boldsymbol{zv}}{1 + \boldsymbol{v}\cdot\boldsymbol{z}}\right)\boldsymbol{y}. \tag{2.56}$$

Here, I is the unit matrix. Two vectors $\boldsymbol{y}$ and $\boldsymbol{z}$ are defined as follows;

$$\boldsymbol{y} = \mathrm{A}^{-1}\boldsymbol{d}\ ,\quad \boldsymbol{z} = \mathrm{A}^{-1}\boldsymbol{u}\ . \tag{2.57}$$

Therefore, the problem of solving a cyclic tridiagonal matrix equation is equivalent to that of solving two tridiagonal matrix equations, Eq. (2.57).

The detail of the numerical calculation method is explained in Appendix A.3.

# Chapter 3
# Validation of Virtual Divertor Model

## 3.1 Basic calculation conditions

In this section, we show some numerical results that validate the virtual divertor (VD) model. As mentioned in the previous section, we assume that the inner and outer SOL-DIV system is symmetric and that the plasma current is absent for simplicity. In addition, as is clear from the plasma fluid equations, the magnetic field is assumed to be uniform. The effect of the neutral particles is not considered here. The plasma parameters of medium-size tokamaks shown in Table 1 are chosen in the simulations by referring to, for example, those of ASDEX-Upgrade plasma [1]. The parameters regarding the VD model are shown in Table 2. The mesh size and time step are set to be $\Delta s$ = 1 cm and $\Delta t$ = 25 ns, respectively. Simulations were conducted until the plasma becomes quasi-stationary unless otherwise noted on the LHD Numerical Analysis Server (PRIMEHPC FX100).

## 3.2 Bohm criterion

It should be verified that the Bohm criterion ($M_t \geq 1$) is satisfied automatically by using the VD model. First, we briefly review the Bohm criterion in an isothermal plasma, $M_t$ = 1 [15]. In the steady state, the equations of continuity and parallel momentum transport become as follows;

$$\frac{\mathrm{d}}{\mathrm{d}s}(nV) = S, \tag{3.1}$$

$$\frac{\mathrm{d}}{\mathrm{d}s}\left(m_i n V^2 + nT_{i,//} + nT_e\right) = 0. \tag{3.2}$$

By eliminating d$n$/d$s$ term, following equation is obtained;

$$\frac{\mathrm{d}M}{\mathrm{d}s} = \frac{S}{nc_s}\frac{1+M^2}{1-M^2} \tag{3.3}$$

This equation has a singularity at the sonic point, $M$ = 1, and does not have

Table 1 Basic parameters of the plasma.

| Parameters | Values |
|---|---|
| The ion species | Hydrogen |
| Parallel SOL length $L_{SOL}$ | 35.2 m |
| Parallel plasma region length $L$ | 44 m |
| Separatrix area $A_{sep}$ | 40 $m^2$ |
| Flux tube width of SOL $d_{SOL}$ | 2 cm |
| Particle flux from the core $\Gamma_{sep}$ | $2\times10^{22}$ /s |
| Heat flux from the core $P_{sep}$ | 2 MW |

Table 2 Basic parameters of the virtual divertor model.

| Parameters | Values |
|---|---|
| Parallel VD region length $L^{VD}$ | 6 m |
| Characteristic time of VD sink $\tau^{VD}$ | 5 μs |
| Artificial energy sink coefficient $g_{i,//}{}^{e,VD}$ | 3 |
| Artificial energy sink coefficient $g_{i,\perp}{}^{VD}$ | 1.2 |
| Artificial energy sink coefficient $g_e{}^{VD}$ | 2.5 |

Table 3 Changed parameters in the smaller SOL-DIV plasma.

| Parameters | Values |
|---|---|
| Parallel SOL length $L_{SOL}$ | 2 m |
| Parallel plasma region length $L$ | 4 m |
| Parallel VD region length $L^{VD}$ | 3 m |
| Particle flux from the core $\Gamma_{sep}$ | $2\times10^{21}$ /s |
| Heat flux from the core $P_{sep}$ | 0.2 MW |

supersonic solutions as far as $S \geq 0$. It thus leads to $M \leq 1$ in the plasma. By combining this fact with the Bohm criterion, the only possibility is $M_t = 1$ at the sheath entrance. Next, we consider a more general case with non-zero parallel ion temperature gradient ($\partial T_{i,//}/\partial s \neq 0$). Note that there are no cooling effects due for example to impurity radiation. In this case, as we mentioned in Sec. 2.1, the adiabatic index $\gamma_A = 3$ is used in estimating the sound speed at the sheath entrance $c_s{}^*$. In a kinetic simulation, $\gamma_A$ was calculated by assuming $M_t{}^* = 1$. The result is shown in Fig. 11 which corresponds to Fig. 3 in Ref [36]. It shows that $\gamma_A$ becomes

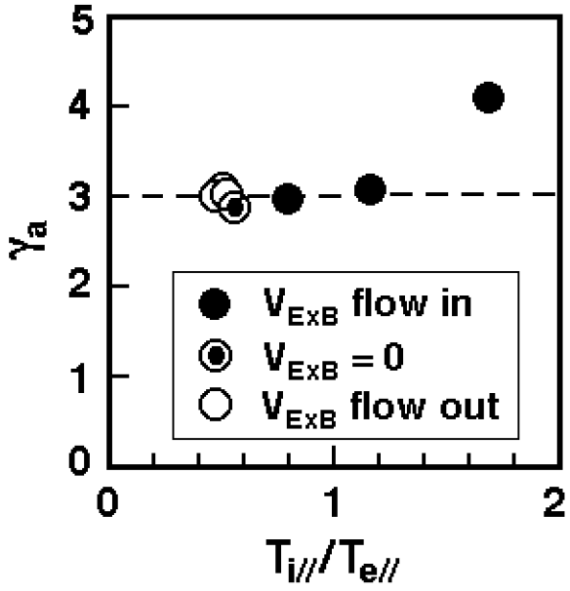


Figure 11 Adiabatic index $\gamma_a$ vs. temperature ratio $T_{i//}/T_{e//}$. Value of $\gamma_a$ is about 3 [36].

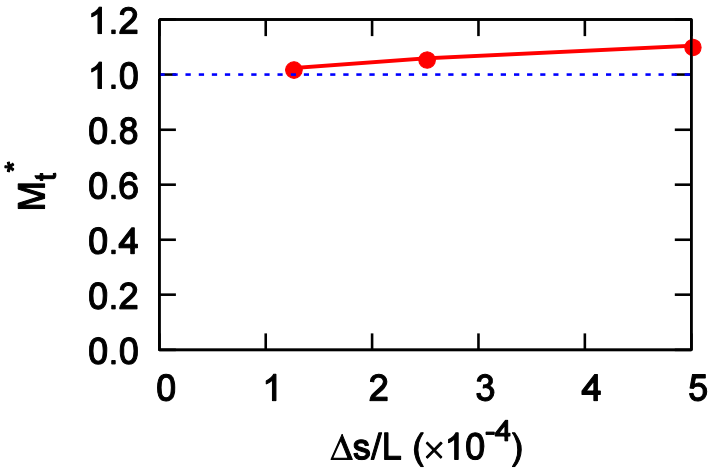


Figure 12 Mach number at the sheath edge $M_t^*$ as a function of normalized mesh size $\Delta s/L$. $M_t^*$ approaches unity as $\Delta s$ approaches zero.

about 3 and means that the assumption of $M_t^* = 1$ is correct. We applied our code to this situation. As we explained in Sec. 2.2, $M_t^*$ is not affected by the downstream condition in principle. In the present numerical simulations, however, due to the first-order accurate upwind scheme, $M_t^*$ is affected by the values of $\tau^{VD}$. This fact requires to use remarkably small mesh sizes $\Delta s$ in order to show the convergence of $M_t^*$, resulting in an enormous increase of computational time. Thus, only in this section, we introduce a smaller SOL-DIV plasma parameters as shown in Table 3.

Here, we used $\Delta s$ = 2, 1 and 0.5 mm. Figure 12 shows the Mach number at the sheath entrance $M_t^*$ as a function of normalized mesh size $\Delta s/L$. Although $M_t^*$ is slightly larger than unity due to the numerical error from the first-order accurate upwind scheme, it approaches unity as $\Delta s$ approaches zero. Thus, we can say that the validity of the VD model for the Bohm criterion is verified.

## 3.3 Sheath heat transmission factors

We should verify that the output values of the sheath heat transmission factors, $\gamma_i$ and $\gamma_e$, can be adjusted to the prescribed values from the sheath theory by changing the values of artificial energy sink coefficients $g^{VD}$ in Eqs. (2.41)-(2.43). From the sheath theory [15], the sheath heat transmission factors are given as follows;

$$\gamma_i = 3, \tag{3.4}$$

$$\gamma_e = 2.5 - 0.5 \ln\left[\left(2\pi \frac{m_e}{m_i}\right)\left(1 + \frac{T_i}{T_e}\right)\right]. \tag{3.5}$$

Here, the effect of the secondary electron is not considered. It should be emphasized that the second term of Eq. (3.5) corresponds to the potential drop in the sheath region and that $\gamma_e$ depends on the mass ratio $m_i/m_e$, so that $\gamma_e \sim 5$ for $H^+$ plasma and $\gamma_e \sim 5.3$ for $D^+$ plasma when $T_i = T_e$. The output sheath heat transmission factors as functions of the artificial energy sink coefficients $g^{VD}$ are shown in Fig. 13. Here, the value of the artificial energy sink coefficient was changed one-by-one with the other two fixed to the values shown in Table 2. Figure 13 shows that $\gamma_i$ scarcely depends on $g^{VD}$. This is because, as will be shown later, the ion heat flux is dominated by the convection. On the other hand, $\gamma_e$ depends on $g_e^{VD}$ as $\gamma_e \sim 5$ ($H^+$ plasma) when $g_e^{VD} \sim 2.6$ and $\gamma_e \sim 5.3$ ($D^+$ plasma) when $g_e^{VD} \sim 2.8$, respectively. When $g_e^{VD} = 1$, $\gamma_e \sim 2.5$ which reflects there is no potential drop in the sheath region. Consequently, it is verified that the output sheath heat transmission factors can be adjusted to the values from the sheath theory in the VD model. The relations shown in Fig. 13, however, can be changed for the calculation conditions. Thus, control of the values of $g^{VD}$ will be necessary in the future.

## 3.4 Preliminary results with plasma model

Here, we show some preliminary results by using the plasma model with VD model. First, we show the profiles of the plasma parameters for collisional and

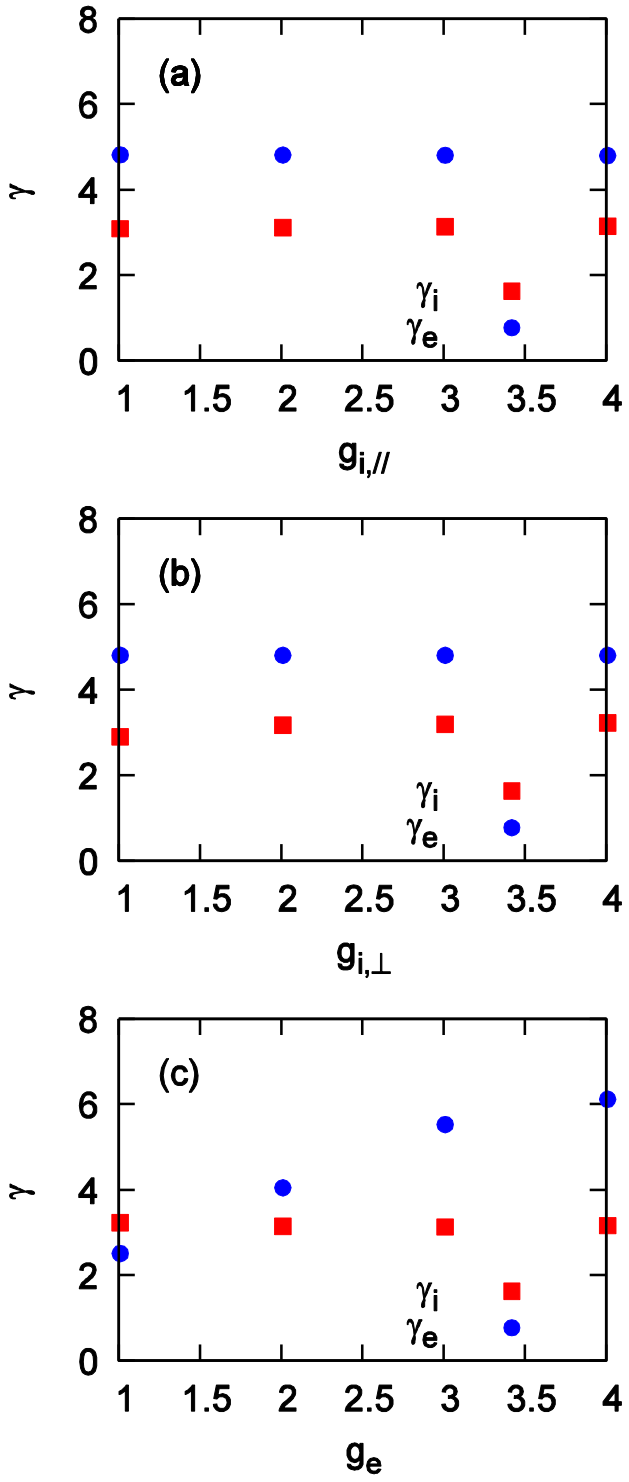


Figure 13 Output sheath heat transmission factors $\gamma$ as functions of the artificial energy sink coefficients (a) $g_{i,//}{}^{e,VD}$, (b) $g_{i,\perp}{}^{VD}$ and (c) $g_e{}^{VD}$.

collisionless conditions. We also investigate the anisotropy of ion temperature for various collisionalities. Secondly, we show that supersonic flows arise due to the radiation cooling. The solutions are compared with the kinetic simulation results and theoretical curves. Finally, the validity of the viscosity approximation is investigated by directly comparing the parallel ion viscous flux and the ion stress tensor $\pi_i$.

### *3.4.1 Collisionality and ion temperature anisotropy*

We conducted a parameter survey by changing the particle and heat fluxes from the core plasma in the ranges of $\Gamma_{sep}$ = 1-5×$10^{22}$ /s and $P_{sep}$ = 1-4 MW, respectively, in order to investigate the relation between the collisionality and the ion temperature anisotropy, $T_{i,//}/T_{i,\perp}$ [47]. The collisionality is estimated by the mean free path of ion-ion Coulomb collision $\lambda_{mfp} \equiv (T_{i,//}/m_i)^{1/2}\tau_i$ normalized by the parallel length of the plasma $L$. First, we show the profiles of plasma parameters for collisional ($\Gamma_{sep}$ = 4×$10^{22}$ /s and $P_{sep}$ = 2 MW; $\lambda_{mfp}/L \sim 0.1$) and collisionless ($\Gamma_{sep}$ = 2×$10^{22}$ /s and $P_{sep}$ = 4 MW; $\lambda_{mfp}/L \sim 10$) conditions in Fig. 14. Because we assume that the inner and outer SOL-DIV plasma is symmetric, the profiles are symmetric at $s$ = 0. A large drop of $T_{i,//}$ can be seen at the X-point $s$ = ± 17.6 m particularly in collisionless case while such a drop can't be seen in $T_{i,\perp}$ profiles. This is because the flow acceleration occurs by consuming the parallel ion pressure $nT_{i,//}$, not $nT_i$, which is described by Eq. (2.4). The ion temperature anisotropy, $T_{i,//}/T_{i,\perp}$, in DIV is about 0.6 for collisional case and 0.2 for collisionless case, respectively.

Here, we briefly explain the origin of the ion temperature anisotropy by a simple analysis. We consider steady state equations of ion energy transport in collisionless limit as follows;

$$\frac{d}{ds}\left(\frac{3}{2}nT_{i,//}V\right) = \frac{1}{3}Q_i^{core}, \tag{3.6}$$

$$\frac{d}{ds}\left(nT_{i,\perp}V\right) = \frac{2}{3}Q_i^{core}. \tag{3.7}$$

Here, the kinetic energy is neglected. We assume that the ion temperature in the core plasma is isotropic as can be seen in the RHS of these equations. In the real plasma, the ion temperature in the core plasma can also be anisotropic depending on the heating methods such as neutral beam injection (NBI) and ion cyclotron resonance frequency (ICRF) heating. In the open magnetic field region, however, the ion temperature tends to be anisotropic due to the energy transport even if the heat source is isotropic. By solving Eqs. (3.6) and (3.7), we obtain the following

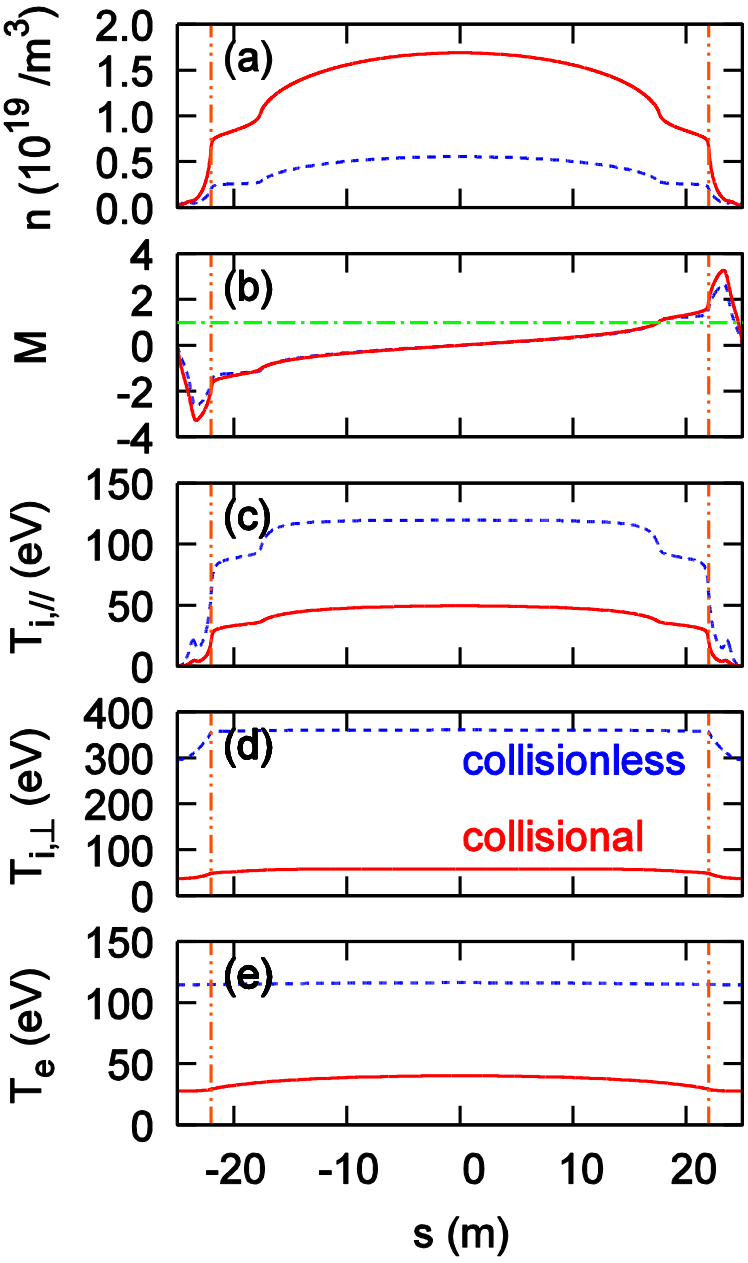


Figure 14 Profiles of (a) plasma density $n$, (b) Mach number $M$, (c) parallel ion temperature $T_{i,//}$, (d) perpendicular ion temperature $T_{i,\perp}$ and (e) electron temperature $T_e$ for collisional (solid lines) and collisionless (broken lines). Vertical chain lines at $s = \pm 22$ m represent the position of the sheath entrance, so that plasma region is $-22 \leq s \leq 22$ m. The X-point exists at $s = \pm 17.6$ m. Profiles are symmetric at $s = 0$ due to the inner/outer SOL-DIV symmetric assumption.

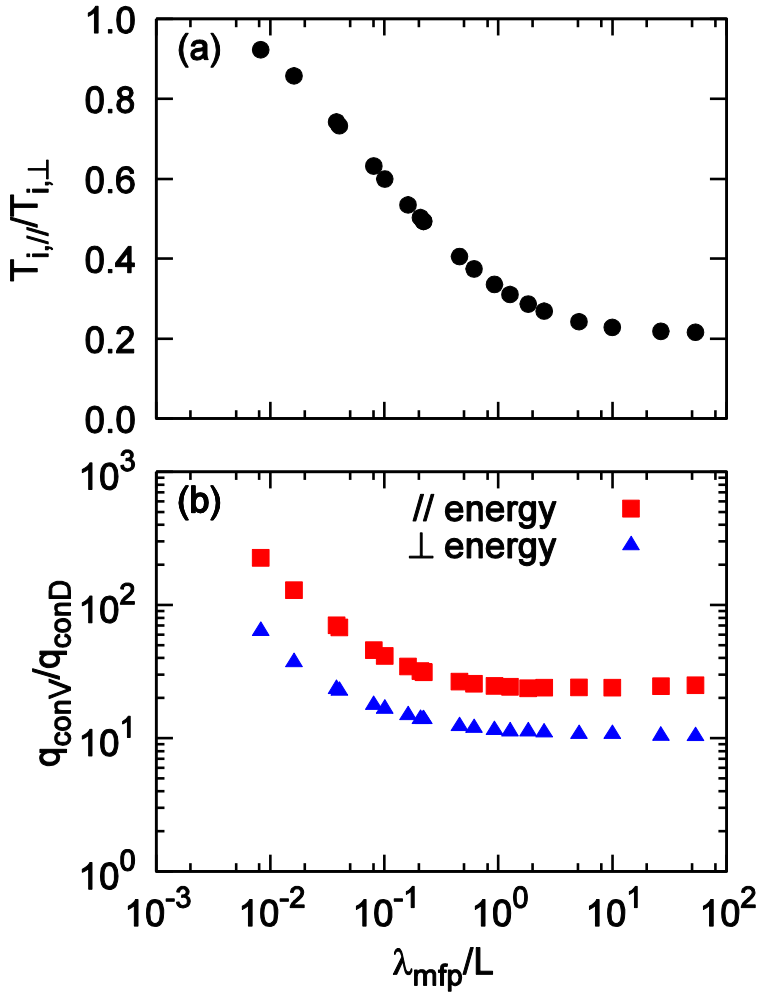


Figure 15 (a) Ion temperature anisotropy and (b) ratios of the convective heat flux $q_{\mathrm{conV}}$ to the conductive one $q_{\mathrm{conD}}$ for parallel (squares) and perpendicular (triangles) ion energy as functions of the normalized mean free path of ion-ion Coulomb collision. Data are picked at $s$ = 20.005 m. The tendency of (a) agrees well with that of the kinetic simulations [48, 49].

solutions in DIV;

$$T_{\mathrm{i},//} = \frac{2Q_{\mathrm{i}}^{\mathrm{core}}}{9S^{\mathrm{core}}}, \quad T_{\mathrm{i},\perp} = \frac{2Q_{\mathrm{i}}^{\mathrm{core}}}{3S^{\mathrm{core}}}. \tag{3.8}$$

Thus, the ion temperature anisotropy becomes $T_{\mathrm{i},//}/T_{\mathrm{i},\perp}$ = 1/3. This is brought about by the difference of convective heat fluxes between the parallel and perpendicular ion energy. This ion temperature anisotropy is relaxed by the ion-ion Coulomb collision.

We investigate the relation between the ion temperature anisotropy and the

collisionality. The result is shown in Fig. 15 (a). Data are picked at $s$ = 20.005 m in DIV. In the collisionless limit, the ion temperature anisotropy becomes $T_{\mathrm{i},/\!/}/T_{\mathrm{i},\perp}$ ~ 0.2 which can be explained qualitatively by the difference of the convective heat fluxes between parallel and perpendicular components. This result agrees well with that of kinetic simulations [48, 49].

In Fig. 15 (b), the ratios of the convective heat flux $q_{\mathrm{conV}}$ to the conductive one $q_{\mathrm{conD}}$ for parallel and perpendicular ion energy are shown. It can be said that the ion heat flux is dominated by the convection in the present calculation conditions. Thus, the choice of the value for $c$ in Eqs. (2.14) and (2.15) does not affect the profiles largely.

### *3.4.2 Supersonic flows due to cooling*

It is shown by kinetic simulations that supersonic flows can be driven by the effects of radiation cooling and radial diffusive loss [58]. Here, we define the flux amplification factor $R$ for particle flux $\Gamma$ and momentum flux $p$ as follows;

$$R_{\Gamma} = \frac{\Gamma_{\mathrm{t}}}{\Gamma_{\mathrm{X}}} = \frac{(nV)_{\mathrm{t}}}{(nV)_{\mathrm{X}}}, \tag{3.9}$$

$$R_{p} = \frac{p_{\mathrm{t}}}{p_{\mathrm{X}}} = \frac{\left(m_{\mathrm{i}} nV^{2} + nT_{\mathrm{i},/\!/} + nT_{\mathrm{e}}\right)_{\mathrm{t}}}{\left(m_{\mathrm{i}} nV^{2} + nT_{\mathrm{i},/\!/} + nT_{\mathrm{e}}\right)_{\mathrm{X}}}. \tag{3.10}$$

Here, the subscripts t and X represent the sheath entrance and the X-point, respectively. From these equations, we obtain following equation;

$$\frac{M_{\mathrm{X}} + M_{\mathrm{X}}^{-1}}{M_{\mathrm{t}} + M_{\mathrm{t}}^{-1}} = C \equiv \frac{R_{\Gamma}}{R_{p}} \sqrt{\frac{T_{\mathrm{t}}}{T_{\mathrm{X}}}}. \tag{3.11}$$

Here, $T \equiv T_{\mathrm{i},/\!/} + T_{\mathrm{e}}$ and $M_{\mathrm{t}} = V_{\mathrm{t}}/c_{\mathrm{s}}$ are used. By assuming that $M_{\mathrm{X}} = 1$ for $C < 1$ and $M_{\mathrm{t}} = 1$ for $C > 1$, we obtain following theoretical curves;

$$M_{\mathrm{t}} = \begin{cases} C^{-1} + \sqrt{C^{-2} - 1} & (C < 1) \\ 1 & (C > 1) \end{cases}, \tag{3.12}$$

$$M_{\mathrm{X}} = \begin{cases} 1 & (C < 1) \\ C - \sqrt{C^{2} - 1} & (C > 1) \end{cases}. \tag{3.13}$$

The kinetic simulation results agree well with those theoretical curves as shown in Fig. 16 which corresponds to Fig. 4 in Ref. [58]. In this figure, $M_1 = M_{\mathrm{X}}$ and $M_2$ =

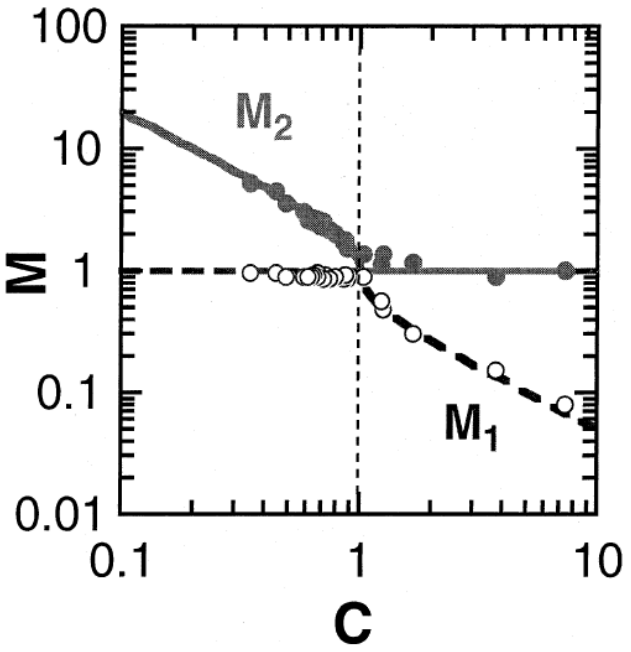


Figure 16 Mach number $M$ vs $C \equiv (R_I/R_p)(T_2/T_1)^{1/2}$. Suffixes 1 and 2 correspond to throat and plate, respectively. Dashed line ($M_1$) and solid line ($M_2$) represent analytical solutions. Simulation results shown by circles agree well with analytical expressions [58].

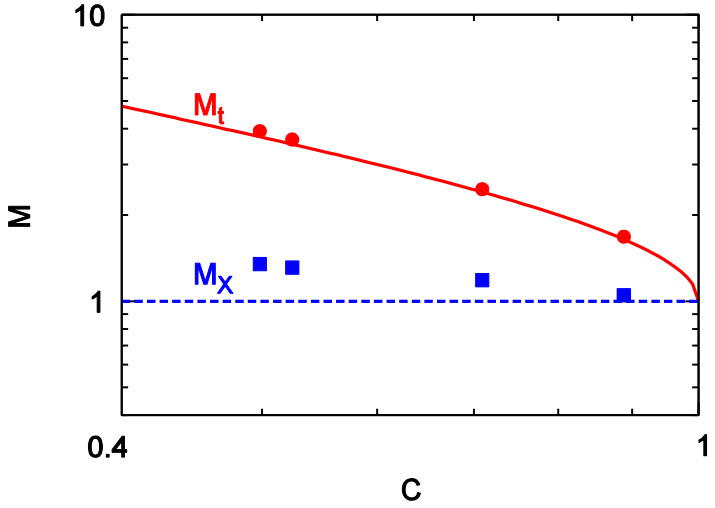


Figure 17 Mach number at the sheath entrance $M_t$ and at the X-point $M_X$ as functions of $C$. The circles and squares are the simulation results for $M_t$ and $M_X$, respectively. The solid and broken lines correspond to the theoretical curves, Eqs. (3.12) and (3.13), respectively.

$M_t$, respectively.

We conducted simulations with radiation cooling by introducing an energy loss term $Q_{rad} = -nT_e/\tau_{rad}$ with an input time constant $\tau_{rad}$ to the electron energy transport equation Eq. (2.7) in DIV. It is one of the superiorities of our code that $M_t$ is self-consistently determined and supersonic flows become tractable. The simulation result is shown in Fig. 17. Mach numbers agree well with the theoretical curves, Eqs. (3.12) and (3.13).

### *3.4.3 Validity of the viscosity approximation*

The validity of the viscosity approximation is investigated by directly comparing the parallel ion viscous flux with the ion stress tensor $\pi_i$ by using the results of parameter survey in Sec. 3.4.1. Here, we give a superscript "def" to the ion stress tensor as $\pi_i^{def}$ in order to distinguish it clearly from the parallel ion viscous flux. For the parallel ion viscous flux, following two kinds are considered (in the region of $V > 0$);

$$\pi_i^{BR} = -\eta_i \frac{\partial V}{\partial s}, \quad \eta_i = 0.96 n T_i \tau_i \quad [37], \tag{3.14}$$

$$\pi_i^{lim} = \left( \frac{1}{\pi_i^{BR}} - \frac{1}{bnT_i} \right)^{-1}. \tag{3.15}$$

We call these viscous fluxes the Braginskii one and the limited one, respectively. The Braginskii viscous flux $\pi_i^{BR}$ was derived under the assumption that the collisionality was high enough for $\pi_i^{def}$ to be much smaller than $nT_i$ and that there was no particle source [15]. Therefore, the validity of $\pi_i^{BR}$ can be lost in the collisionless condition or in the SOL where there is a particle source from the core plasma. In SOL-DIV plasma fluid codes, thus, the limited viscous flux $\pi_i^{lim}$ is often used. The viscous flux limiter is denoted by $b$. From the kinetic results, $b$ = 0.5, for example, is proposed [59]. In the simulation results below, $b$ = 0.7 is also used so that $\pi_i^{lim} = \pi_i^{def}$ in the collisionless limit. Dada are picked up at $s$ = 17.005 m in SOL and $s$ = 20.005 m in DIV. The ratios of two kinds of parallel ion viscous fluxes to the ion stress tensor are shown in Fig. 18 as functions of the normalized mean free path of ion-ion Coulomb collision. It is shown in Fig. 18 (a) that $\pi_i^{BR}$ indeed becomes larger than $\pi_i^{def}$ as the collisionality becomes low. Dissociation of $\pi_i^{BR}$ from $\pi_i^{def}$ is faster in SOL than in DIV. As shown in Fig. 18 (b), this tendency of $\pi_i^{BR}$ affects $\pi_i^{lim}$, too, particularly in the collisional regime where the effect of $\pi_i^{BR}$ is dominant in Eq. (3.15). If we use $b$ = 0.5, the dissociation in the collisionless limit becomes larger. It indicates, therefore, that the viscous flux

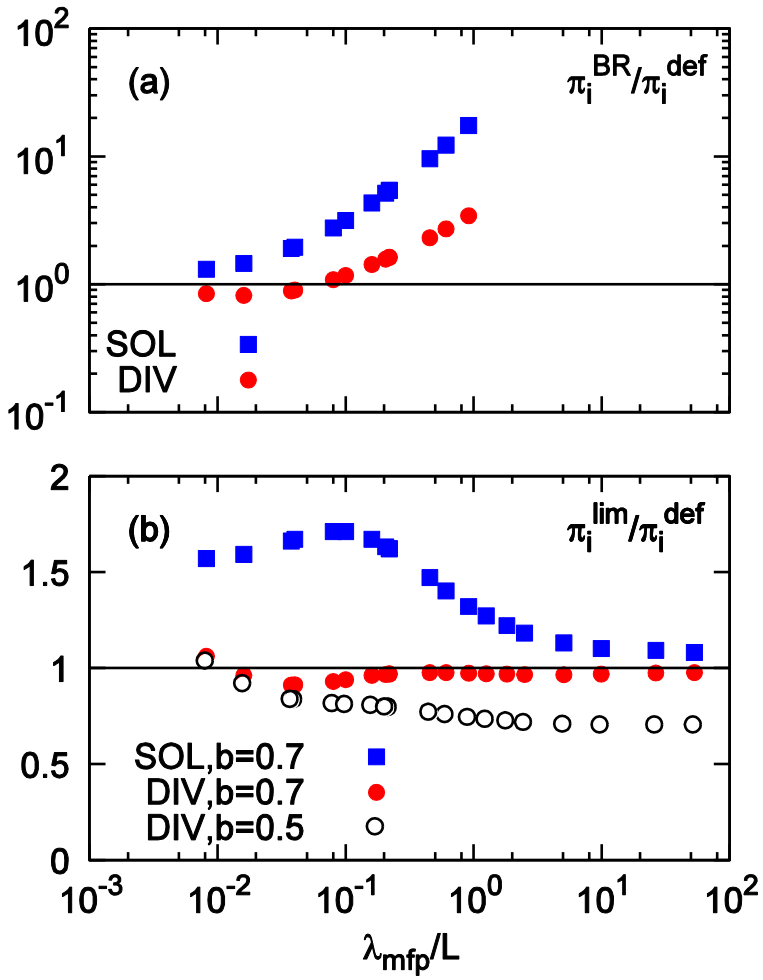


Figure 18 Ratios of (a) the Braginskii viscous flux $\pi_i^{BR}$ and (b) the limited one $\pi_i^{lim}$ to the ion stress tensor $\pi_i^{def}$ in SOL and DIV as functions of the normalized mean free path of ion-ion Coulomb collision. Squares and circles correspond to SOL and DIV, respectively. In (b), the viscous flux limiter of $b = 0.7$ (closed points) and $b = 0.5$ (open circles) are used.

limiter must be expressed as a function of the collisionality, $b = b(\lambda_{mfp}/L)$, if the viscosity approximation is used. However, the relation of the viscous flux limiter $b$ and the collisionality might be changed with neutral effects. Consequently, it is more important and easier way to introduce the anisotropic ion temperatures in the SOL-DIV plasma fluid model.

# Chapter 4
# Numerical Model for Neutrals

## 4.1 Fluid equations for neutrals

In order to simulate more general plasmas in SOL-DIV region, the effect of neutrals is essential for, in particular, the reproduction of the high recycling or the detached plasmas. Because neutrals are not affected by the magnetic field and the geometry of the walls directly affects the profile of neutrals, they are generally treated in the models of at least 2D. In addition, kinetic neutral codes other than the fluid codes are often coupled with the plasma fluid code in many SOL-DIV plasma code packages [22, 23, 24]. The atomic and molecular processes are also important. In our code, however, we introduce a 1D (poloidal direction) fluid neutral model for atoms which is the minimum required to reproduce the general SOL-DIV plasmas. The considered atomic processes are as follows;

Ionization (iz): $\mathrm{H}^0 + \mathrm{e}^- \rightarrow \mathrm{H}^+ + \mathrm{e}^- + \mathrm{e}^-$, (4.1)

Charge exchange (cx): $\mathrm{H}^0 + \mathrm{H}^+ \rightarrow \mathrm{H}^+ + \mathrm{H}^0$, (4.2)

Volume recombination (rc): $\mathrm{H}^+ + \mathrm{e}^- \rightarrow \mathrm{H}^0$. (4.3)

In dense plasmas, it is valid to express the neutral transport as a diffusion process because the neutrals are thermalized due to the charge exchange reaction as follows [60];

$$\frac{\partial n_{\mathrm{n}}}{\partial t} + \frac{\partial}{\partial x}\left( - D_{\mathrm{n}} \frac{\partial n_{\mathrm{n}}}{\partial x} \right) = S_{\mathrm{n}}. \tag{4.4}$$

Here, the density, diffusivity and source term of the neutrals are denoted by $n_{\mathrm{n}}$, $D_{\mathrm{n}}$ and $S_{\mathrm{n}}$, respectively. The coordinate $x$ is in the poloidal direction and the relation between $x$ and $s$ is shown in Fig. 19 and described in terms of the pitch angle $\theta$ as follows;

$$x = s(\sin\theta), \tag{4.5}$$

$$\sin\theta = \frac{B_{\mathrm{p}}}{B}, \tag{4.6}$$

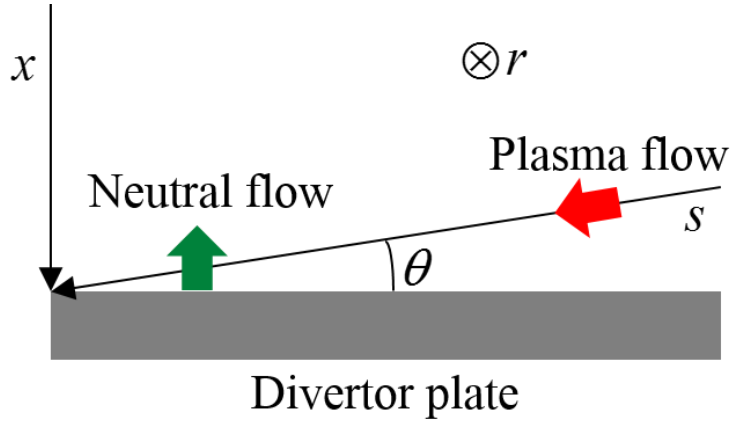


Figure 19 Relation between the coordinates $s$ and $x$ ($r$ is in the radial direction).

where $B_p$ and $B$ are the magnitude of poloidal and total magnetic field. The diffusivity of the neutrals $D_n$ is estimated as follows;

$$D_n = \frac{v_n^2}{\nu_{cx} + \nu_{iz}}. \tag{4.7}$$

Here, $v_n \equiv (T_n/m_i)^{1/2}$ is the thermal velocity of neutrals with temperature $T_n$. The neutral temperature is assumed to be the same of ion temperature $T_i$ due to the charge exchange reaction. The source term $S_n$ is estimated as follows;

$$S_n = -n_n \nu_{iz} + n \nu_{rc}. \tag{4.8}$$

Here, the radial loss of neutrals is not included. The frequencies $\nu$ are defined as follows;

$$\nu_{iz} = n\langle \sigma v \rangle_{iz}, \tag{4.9}$$

$$\nu_{cx} = n\langle \sigma v \rangle_{cx}, \tag{4.10}$$

$$\nu_{rc} = n\langle \sigma v \rangle_{rc}, \tag{4.11}$$

where $<\sigma v>$ is the reaction rate. The effect of recycling of the ions is treated by the boundary condition at the divertor plate as follows;

$$-D_0 \frac{\partial n_n}{\partial x} = -\eta n V \sin\theta. \tag{4.12}$$

Here, $\eta$ is the recycling coefficient of ions.

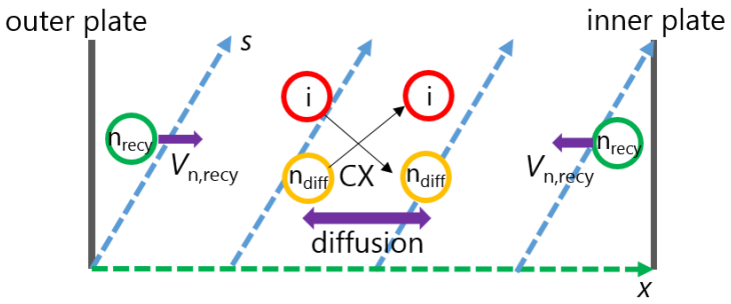


Figure 20 Schematic picture of the neutral model based on the FFCD model [61].

This diffusion description of the neutrals, however, cannot be applied to the neutrals originating at the divertor plates because they are not thermalized until they experience at least one charge exchange reaction. Thus, the diffusion description tends to be invalid in a low density plasma. In order to resolve this problem, the first flight corrected diffusion (FFCD) model was proposed in Ref. [62]. This model distinguishes between the neutrals originating at the divertor plates and those which have experienced at least one charge exchange reaction. Here, we call the former the recycling neutrals and the latter the diffusion ones, respectively. The recycling neutrals are further divided into two groups depending on the divertor plates where they are generated. The schematic picture of this neutral model is shown in Fig. 20. The fluid equations for these neutrals are as follows [63];

$$\frac{\partial n_{\mathrm{n,recy}}^{\mathrm{out}}}{\partial t}+\frac{\partial}{\partial x}\left(n_{\mathrm{n,recy}}^{\mathrm{out}}V_{\mathrm{n,recy}}^{\mathrm{out}}\right)=S_{\mathrm{n,recy}}^{\mathrm{out}}, \tag{4.13}$$

$$\frac{\partial n_{\mathrm{n,recy}}^{\mathrm{inn}}}{\partial t}+\frac{\partial}{\partial x}\left(n_{\mathrm{n,recy}}^{\mathrm{inn}}V_{\mathrm{n,recy}}^{\mathrm{inn}}\right)=S_{\mathrm{n,recy}}^{\mathrm{inn}}, \tag{4.14}$$

$$\frac{\partial n_{\mathrm{n,diff}}}{\partial t}+\frac{\partial}{\partial x}\left(-D_{\mathrm{n}}\frac{\partial n_{\mathrm{n,diff}}}{\partial x}\right)=S_{\mathrm{n,diff}}. \tag{4.15}$$

Here, the subscripts “recy” and “diff” represent the recycling and diffusion neutrals, and the superscripts “out” and “inn” the recycling neutrals generated on the outer and inner divertor plates, respectively. The flow velocities of the recycling neutrals are determined as follows;

$$V_{\mathrm{n,recy}}^{\mathrm{out}}=-V_{\mathrm{n,recy}}^{\mathrm{inn}}=\frac{1}{2}\sqrt{\frac{2\varepsilon_{\mathrm{FC}}}{m_{\mathrm{i}}}}, \tag{4.16}$$

where $\varepsilon_{\mathrm{FC}}$ = 3.5 eV is the Franck-Condon energy which is the energy that the dissociated atoms from a molecule have. For the diffusivity, we use the following

equation by considering the radial loss of the diffusion neutrals;

$$D_{\mathrm{n}} = \frac{v_{\mathrm{n}}^2}{\nu_{\mathrm{cx}} + \nu_{\mathrm{iz}} + \nu_{\mathrm{L,diff}}}. \tag{4.16}$$

Here, $\nu_{\mathrm{L,diff}}$ is the frequency of radial loss of the diffusion neutrals defined as follows;

$$\nu_{\mathrm{L,diff}} = \alpha_{\mathrm{L}} \frac{v_{\mathrm{n}}}{d}, \tag{4.17}$$

$$\alpha_{\mathrm{L}} = \exp\left( -\frac{d}{\lambda_{\mathrm{n,cx}}} \right), \quad \lambda_{\mathrm{n,cx}} = \frac{v_{\mathrm{n}}}{\nu_{\mathrm{cx}}}. \tag{4.18}$$

Here, the coefficient $\alpha_{\mathrm{L}}$ reflects the efficiency of confinement of the diffusion neutrals by the charge exchange reactions. The notations $d$ and $\lambda_{\mathrm{cx}}$ are the radial width of the flux tube and the mean free path of charge exchange of neutrals, respectively. For the boundary conditions, we assume that there is no reflection of the diffusion neutrals at the divertor plates and that they are recycled as recycling neutrals as follows;

$$n_{\mathrm{n,recy}}^{\mathrm{out}} V_{\mathrm{n,recy}}^{\mathrm{out}} = -\eta n V \sin\theta + \eta_{\mathrm{n}} \left( D_{\mathrm{n}} \frac{\partial n_{\mathrm{n,diff}}}{\partial x} \right), \tag{4.19}$$

$$n_{\mathrm{n,recy}}^{\mathrm{inn}} V_{\mathrm{n,recy}}^{\mathrm{inn}} = -\eta n V \sin\theta + \eta_{\mathrm{n}} \left( D_{\mathrm{n}} \frac{\partial n_{\mathrm{n,diff}}}{\partial x} \right), \tag{4.20}$$

$$-D_{\mathrm{n}} \frac{\partial n_{\mathrm{n,diff}}}{\partial x} = C_{\mathrm{n}} n_{\mathrm{n,diff}} v_{\mathrm{n}}. \tag{4.21}$$

Here, $\eta_{\mathrm{n}}$ is the recycling coefficient of the diffusion neutrals. The coefficient $C_{\mathrm{n}}$ is determined by considering the kinetic effects and, for example, $C_{\mathrm{n}} = (1/\pi)^{1/2}$ is proposed in Ref. [62].

## 4.2 Virtual divertor model for neutrals

As we explained in Chapter 2, the virtual divertor (VD) model was introduced in order to represent the effects of the sheath region and the divertor plate where an artificial region (VD region) was set beyond the sheath entrance with artificial volume sinks for particle, momentum and energy of the plasma. This kind of model is necessary because the conventional boundary condition for the Mach number at the sheath entrance, $M_{\mathrm{t}} = 1$, is no longer used with the first-order

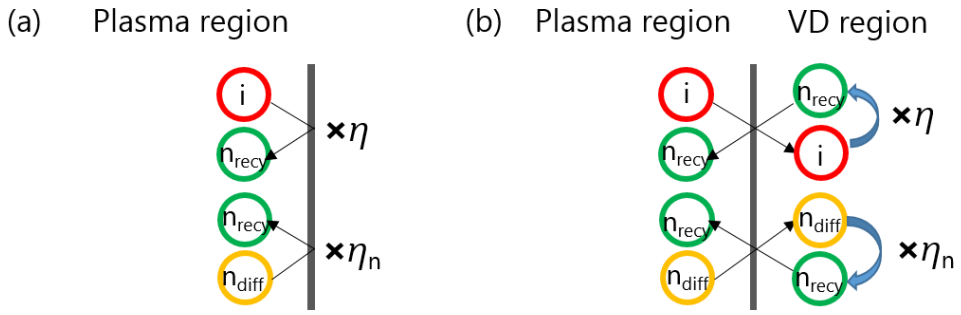


Figure 21 Schematic picture of the comparison of boundary condition treatment for the neutrals between (a) a conventional way and (b) using the VD model [61].

differential parallel momentum transport equation, Eq. (2.4). In addition, by using a periodic boundary condition, it becomes much easier to treat the complex geometry of the walls in real devices. Thus, it is worthwhile to develop a VD model for neutrals. The basic idea is schematically shown in Fig. 21. First, because the divertor plate works as a pure sink for the diffusion neutrals in no reflection conditions, we set the following artificial particle sink term in the VD region;

$$S_{\mathrm{n,diff}}^{\mathrm{VD}} = -\frac{n_{\mathrm{n,diff}}}{\tau_{\mathrm{n}}^{\mathrm{VD}}}. \tag{4.22}$$

Here, the characteristic time for artificial sink for diffusion neutrals $\tau_{\mathrm{n}}^{\mathrm{VD}}$ is an input parameter. Because the equation for the diffusion neutrals, Eq. (4.15), is the second-order differential, $\tau_{\mathrm{n}}^{\mathrm{VD}}$ should be controlled to adjust the coefficient $C_{\mathrm{n}}$ to the prescribed value by an analogy of the artificial energy sink coefficient $g^{\mathrm{VD}}$ for the sheath heat transmission factors $\gamma$.

Second, in order to reproduce the boundary conditions of recycling, Eqs. (4.19) and (4.20), the dumped ions and diffusion neutrals in the VD region are converted into the recycling neutrals multiplied by $\eta$ and $\eta_{\mathrm{n}}$, respectively, and given to the equation for the recycling neutrals, Eqs. (4.13) and (4.14) as an artificial source terms as follows;

$$S_{\mathrm{n,recy}}^{\mathrm{out,VD}} = \eta \frac{n}{\tau^{\mathrm{VD}}} H(-V) + \eta_{\mathrm{n}} \frac{n_{\mathrm{n,diff}}}{\tau_{\mathrm{n}}^{\mathrm{VD}}} H\left(\frac{\partial n_{\mathrm{n,diff}}}{\partial x}\right), \tag{4.23}$$

$$S_{\mathrm{n,recy}}^{\mathrm{inn,VD}} = \eta \frac{n}{\tau^{\mathrm{VD}}} H(V) + \eta_{\mathrm{n}} \frac{n_{\mathrm{n,diff}}}{\tau_{\mathrm{n}}^{\mathrm{VD}}} H\left(-\frac{\partial n_{\mathrm{n,diff}}}{\partial x}\right). \tag{4.24}$$

The Heaviside step function $H$ is necessary in order to decide the "watershed" of the particle sources for inner-derived and outer-derived in the asymmetric condition in the future although it is always the center of the VD region in the

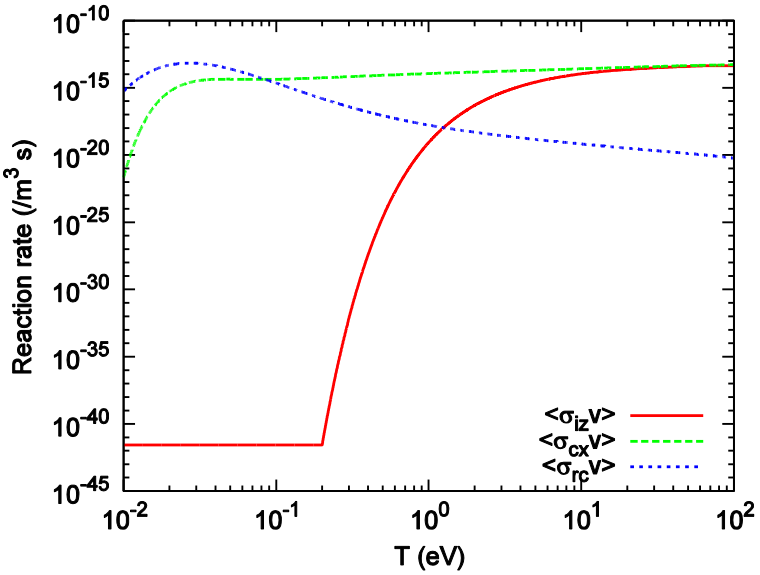


Figure 22 Reaction rates of ionization (iz, solid line), charge exchange (cx, broken line) and volume recombination (rc, dotted line) as functions of ion or electron temperatures [43].

symmetric condition. In the calculations below, we use $\eta = \eta_n = 1$.

## 4.3 Source terms

In this section, we explain the source terms for the neutral particles and plasma particles, momentum and energy relevant to the atomic processes. The reaction rates $<\sigma v>_{iz}(T_e)$, $<\sigma v>_{cx}(T_i)$ and $<\sigma v>_{rc}(T_e)$ are shown in Fig. 22. Note that in the source terms below, the atomic processes do not work in the VD region and only the artificial sinks are effective there. The source term for the recycling neutrals which are lost by the charge exchange, ionization and radial transport is described as follows;

$$S_{n,recy}^{out} = -n_{n,recy}^{out}\left(\nu_{cx} + \nu_{iz} + \nu_{L,recy}\right) + S_{n,recy}^{out,VD}, \tag{4.25}$$

$$S_{n,recy}^{inn} = -n_{n,recy}^{inn}\left(\nu_{cx} + \nu_{iz} + \nu_{L,recy}\right) + S_{n,recy}^{inn,VD}. \tag{4.26}$$

Here, the frequency of radial loss of the recycling neutrals is given by;

$$\nu_{L,recy} = \frac{\sqrt{\varepsilon_{FC}/m_i}}{d}. \tag{4.27}$$

As for the diffusion neutrals, which are lost by the ionization and radial transport,

and generated by the charge exchange of the recycling neutrals and the volume recombination of plasma, the source term is described as follows;

$$S_{\mathrm{n,diff}} = -n_{\mathrm{n,diff}}\left(\nu_{\mathrm{iz}} + \nu_{\mathrm{L,diff}}\right) + n_{\mathrm{n,recy}}\nu_{\mathrm{cx}} + n\nu_{\mathrm{rc}} + S_{\mathrm{n,diff}}^{\mathrm{VD}}. \tag{4.28}$$

Accompanied by these reactions, the source terms for the plasma particles, momentum and energy are estimated as follows;

$$S = S^{\mathrm{core}} + n_{\mathrm{n}}\nu_{\mathrm{iz}} - n\nu_{\mathrm{rc}} + S^{\mathrm{VD}}, \tag{4.29}$$

$$\begin{aligned} M_{\mathrm{m}} &= m_{\mathrm{i}}\sin\theta\left(n_{\mathrm{n,recy}}^{\mathrm{out}}V_{\mathrm{n,recy}}^{\mathrm{out}} + n_{\mathrm{n,recy}}^{\mathrm{inn}}V_{\mathrm{n,recy}}^{\mathrm{inn}}\right)\left(\nu_{\mathrm{cx}} + \nu_{\mathrm{iz}}\right) \\ &- m_{\mathrm{i}}V\left(n_{\mathrm{n}}\nu_{\mathrm{cx}} + n\nu_{\mathrm{rc}}\right) + M_{\mathrm{m}}^{\mathrm{VD}}, \end{aligned} \tag{4.30}$$

$$\begin{aligned} Q_{\mathrm{i},//} &= Q_{\mathrm{i},//}^{\mathrm{core}} + \left(\frac{2}{3}m_{\mathrm{i}}n_{\mathrm{n,recy}}V_{\mathrm{n,recy}}^{2} + \frac{1}{2}n_{\mathrm{n,diff}}T_{\mathrm{i}}\right)\left(\nu_{\mathrm{cx}} + \nu_{\mathrm{iz}}\right) \\ &- \left(\frac{1}{2}m_{\mathrm{i}}V^{2} + \frac{1}{2}T_{\mathrm{i},//}\right)\left(n_{\mathrm{n}}\nu_{\mathrm{cx}} + n\nu_{\mathrm{rc}}\right) + Q_{\mathrm{i},//}^{\mathrm{VD}}, \end{aligned} \tag{4.31}$$

$$\begin{aligned} Q_{\mathrm{i},\perp} &= Q_{\mathrm{i},\perp}^{\mathrm{core}} + \left(\frac{4}{3}m_{\mathrm{i}}n_{\mathrm{n,recy}}V_{\mathrm{n,recy}}^{2} + n_{\mathrm{n,diff}}T_{\mathrm{i}}\right)\left(\nu_{\mathrm{cx}} + \nu_{\mathrm{iz}}\right) \\ &- T_{\mathrm{i},\perp}\left(n_{\mathrm{n}}\nu_{\mathrm{cx}} + n\nu_{\mathrm{rc}}\right) + Q_{\mathrm{i},\perp}^{\mathrm{VD}}, \end{aligned} \tag{4.32}$$

$$Q_{\mathrm{e}} = Q_{\mathrm{e}}^{\mathrm{core}} - \varepsilon_{\mathrm{iz}}n_{\mathrm{n}}\nu_{\mathrm{iz}} - \frac{3}{2}T_{\mathrm{e}}n\nu_{\mathrm{rc}} + Q_{\mathrm{rad}} + Q_{\mathrm{e}}^{\mathrm{VD}}. \tag{4.33}$$

Here, we assume that the each recycling neutral has kinetic energy of $\varepsilon_{\mathrm{FC}}$ (corresponding velocity of $(2\varepsilon_{\mathrm{FC}}/m_{\mathrm{i}})^{1/2}$) and is emitted in all directions with equal probability. The average velocities in the poloidal direction ($x$) and in the parallel direction to the magnetic field ($s$) are $|V_{\mathrm{n,recy}}| = (2\varepsilon_{\mathrm{FC}}/m_{\mathrm{i}})^{1/2}/2$ and $|V_{\mathrm{n,recy}}|\sin\theta$, respectively. The average energy in the parallel and perpendicular directions to the magnetic field are $(1/3)\varepsilon_{\mathrm{FC}} = (2/3)m_{\mathrm{i}}V_{\mathrm{n,recy}}^{2}$ and $(2/3)\varepsilon_{\mathrm{FC}} = (4/3)m_{\mathrm{i}}V_{\mathrm{n,recy}}^{2}$, respectively. We define $n_{\mathrm{n,recy}} \equiv n_{\mathrm{n,recy}}^{\mathrm{out}} + n_{\mathrm{n,recy}}^{\mathrm{inn}}$ and $n_{\mathrm{n}} \equiv n_{\mathrm{n,recy}} + n_{\mathrm{n,diff}}$. The ionization energy loss is set to be $\varepsilon_{\mathrm{iz}} = 30$ eV assuming that the excitation energy loss occurs at the same frequency. For the electron energy loss due to impurity radiation $Q_{\mathrm{rad}}$, we use the following simple radiation model [64];

$$Q_{\mathrm{rad}} = -L_{\mathrm{z}}\left(T_{\mathrm{e}}\right)r_{\mathrm{imp}}n^{2}. \tag{4.34}$$

Here, $L_{\mathrm{z}}$ and $r_{\mathrm{imp}}$ are the radiation rate and fraction of impurity to the plasma

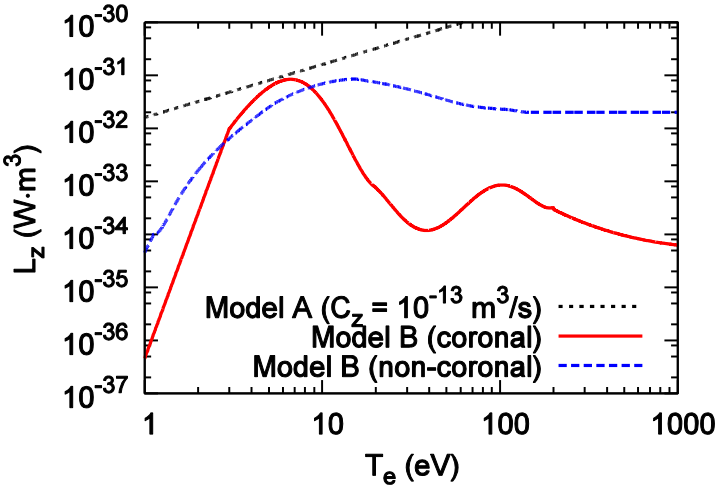


Figure 23 Radiation rates as functions of $T_e$ of Model A for $C_z$ = $10^{-13}$ m$^3$/s by dotted line and Model B for coronal and non-coronal by solid and dashed lines, respectively [65].

density, respectively. For $L_z$, we use the following two types of models;

Model A: $L_z$ is given by the following equation;

$$L_z = C_z T_e. \tag{4.35}$$

Here, $C_z$ is an input parameter. The shape of $L_z$ for $C_z$ = $10^{-13}$ m$^3$/s is shown in Fig. 23.

Model B: $L_z$ is given from the radiation data of carbon impurity as shown in Fig. 23.

In addition, the radiation region is chosen from following two types;

Type A: in the range of 1 m in parallel direction in front of the sheath entrance.

Type B: in the whole plasma region.

## 4.4 Diffusion neutral model

The diffusion neutral model [60] with the VD model is also available in our code. The basic equations are as follows;

$$\frac{\partial n_n}{\partial t} + \frac{\partial}{\partial x}\left( - D_n \frac{\partial n_n}{\partial x} \right) = S_n, \tag{4.36}$$

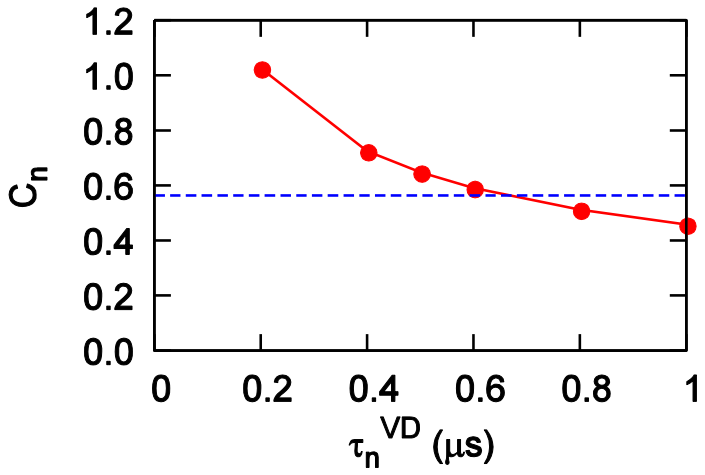


Figure 24 Coefficient $C_n$ as a function of $\tau_n^{VD}$. The dashed line represents $C_n = 1/\pi^{1/2}$.

$$D_n = \frac{v_n^2}{\nu_{cx} + \nu_{iz} + \nu_L}, \tag{4.37}$$

$$S_n = -n_n(\nu_{iz} + \nu_L) + n\nu_{rc} + S_n^{VD}, \tag{4.38}$$

$$\nu_L = \alpha_L \frac{v_n}{d}, \quad \alpha_L = \exp\left(-\frac{d}{\lambda_{n,cx}}\right), \quad \lambda_{n,cx} = \frac{v_n}{\nu_{cx}}, \tag{4.39}$$

$$S_n^{VD} = \eta \frac{n}{\tau^{VD}}. \tag{4.40}$$

Here, the artificial sink, Eq. (4.40), is for the following boundary condition;

$$D_n \frac{\partial n_n}{\partial x} = -\eta n V \sin\theta. \tag{4.41}$$

This model is available only in the symmetric conditions. In asymmetric conditions, the “watershed” should be considered like Eqs. (4.23) and (4.24) and convective transport should be introduced in the VD region in order to reproduce the boundary condition Eq. (4.41) by the artificial sink Eq. (4.40).

## 4.5 Validity of the virtual divertor model for the neutral model

It should be verified that the coefficient $C_n$ in Eq. (4.21) can be adjusted to the prescribed value by changing the value of $\tau_n^{VD}$ in Eq. (4.22). The plasma

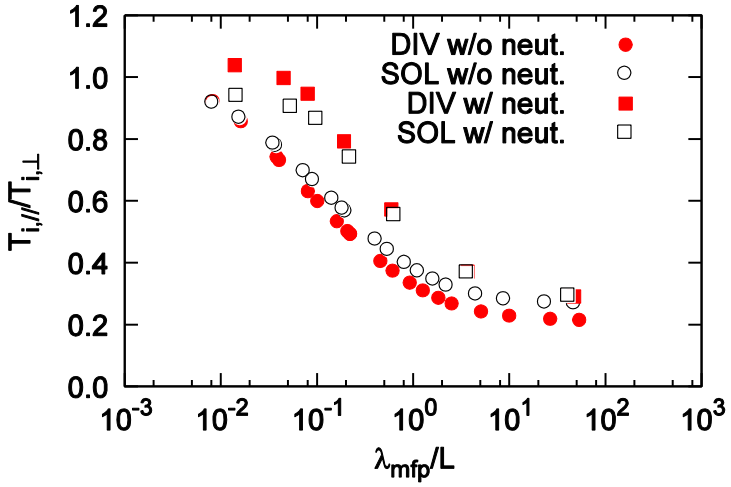


Figure 25 Ion temperature anisotropy as a function of the normalized mean free path of ion-ion Coulomb collision. Circles and squares correspond to "without" and "with" neutrals, and closed and open to DIV and SOL, respectively. Data are picked at $s$ = 17.005 m in SOL and $s$ = 20.005 m in DIV.

parameters and the VD model parameters are the same as Table. 1 and 2. The flux tube width in DIV is $d_{DIV}$ = 2 cm and $\theta$ = 6°. The coefficient $\alpha_L$ in Eq. (4.18) is fixed to be unity and the impurity radiation is absent for simplicity. The value of $\tau_n^{VD}$ is changed in the range of $0.2 \leq \tau_n^{VD} \leq 1$ μs. Figure 24 shows the coefficient $C_n$ as a function of $\tau_n^{VD}$. It can be seen that $C_n$ can be adjusted to the prescribed value by changing the value of $\tau_n^{VD}$ for example $C_n = 1/\pi^{1/2}$ [62] when $\tau_n^{VD} \sim 0.65$ μs. Because this relationship between $C_n$ and $\tau_n^{VD}$ can be changed by the calculation conditions, it will be needed to control the value of $\tau_n^{VD}$ in the future.

## 4.6 Preliminary results with neutral model

Here, we show some preliminary results by using the plasma and neutral model with VD model. First, we show the anisotropy of ion temperature for various collisionalities again by introducing the effect of neutrals. Second, we investigated the effect of the modification of the diffusivity $D_n$ on the profiles. In these simulations, $\alpha_L$ is fixed to be unity for simplicity and $\tau_n^{VD}$ = 1 μs is used.

### *4.6.1 Effect of neutrals on the ion temperature anisotropy*

We set the particle and heat fluxes from the core plasma to be ($\Gamma_{sep}$ ($\times 10^{22}$ /s), $P_{sep}$ (MW)) = (1, 4), (2, 4), (3, 4), (4, 1), (4, 2), (4, 4), (4, 5). Data are picked up from

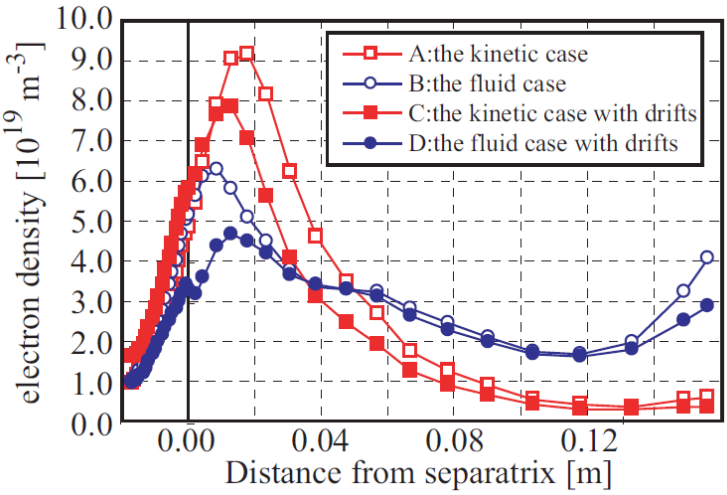


Figure 26 Radial profile of electron density at the outer divertor [66].

$s$ = 17.005 m in SOL and $s$ = 20.005 m in DIV, respectively. The FFCD neutral model was used. The ion temperature anisotropy, $T_{i,//}/T_{i,\perp}$, as a function of the normalized mean free path of ion-ion Coulomb collision is shown in Fig. 25. The ion temperature anisotropy tends to be relaxed by the effect of neutrals.

### *4.6.2 Effect of modification of the diffusivity on the profiles*

In the conventional SOL-DIV code packages [22, 23], a kinetic Monte-Carlo (MC) model is often used for the neutral model. Although the kinetic MC models consider every kinetic effect, it always has problems of long computational time and MC noise. In this point, fluid neutral model is useful. It is pointed out, however, that there is a significant difference between the simulation results with a fluid model and those with a kinetic MC model as shown in Fig. 26 which corresponds to Fig. 3 (a) [66]. It is indicated that spread of the neutral particles in DIV is larger in the fluid model than in the kinetic MC model. Thus, we suspect that this overestimation of neutral particle diffusivity comes from the fact that the frequency of radial loss of neutrals is not considered in the conventional diffusivity as shown in Eq. (4.7). From the random walk point of view, the effect of radial loss should be treated in the same way as the ionization as shown in Eqs. (4.16) and (4.37). Here, we denote the conventional and our diffusivities $D_{ci}$ and $D_{ciL}$, respectively. Note that the effect of radial loss is included in the source term Eq. (4.28) even if $D_{ci}$ is used.

First, we compared the profiles of plasma and neutral densities in DIV between the two kinds of diffusivities by using the diffusion neutral model as shown in Fig. 27 (a). In this case, the frequency of radial loss $\nu_L \sim 4\times10^6$ /s is larger by one order

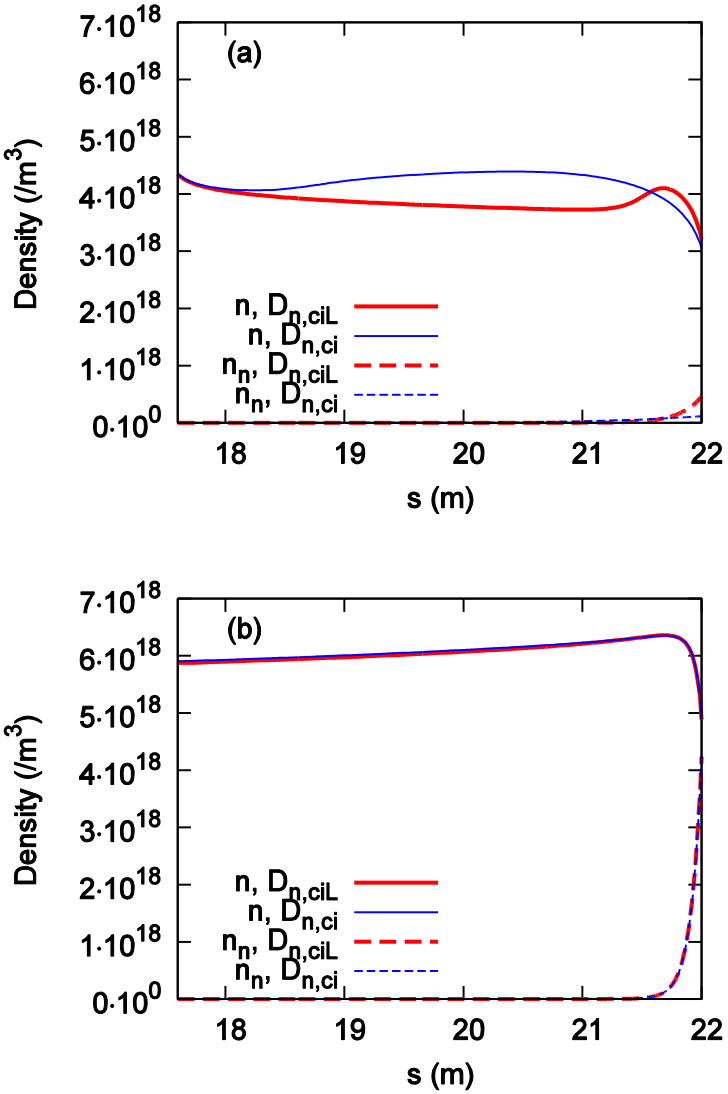


Figure 27 Profiles of plasma density (solid lines) and neutral density (broken lines) in DIV by using ordinary diffusivity $D_{n,ci}$ (thin lines) and modified diffusivity $D_{n,ciL}$ (thick lines) with (a) diffusion neutral model and (b) FFCD neutral model.

than the frequencies of ionization and charge exchange $\nu_{iz} \sim \nu_{cx} \sim 2\times10^5$ /s, so that the effect of radial loss dominates and reduces the diffusivity of Eq. (4.37). It is clear from Fig. 27 (a) that the spread of neutral particles is larger in the case of $D_{n,ci}$ than $D_{n,ciL}$. This difference of neutral dynamics affects the plasma density, so that the increase of the density spreads in the case of $D_{n,ci}$. Second, we used the FFCD neutral model and again compared the profiles of plasma and neutral densities in DIV between two kinds of diffusivities in Fig. 27 (b). In this case, too,

$\nu_{L,diff} \sim 3\times10^6$ /s is larger by one order than $\nu_{iz} \sim \nu_{cx} \sim 3\times10^5$ /s but the diffusion neutral density $n_{n,diff}$ is by two orders lower than the recycling neutral density $n_{n,recy}$ near the divertor plate, so that the difference is negligible. In cases of $n_{n,diff} >> n_{n,recy}$, the plasmas are in high recycling regime and $\nu_{L,diff}$ is much smaller than $\nu_{cx}$ meaning $D_{ci} \sim D_{ciL}$. Consequently, attention should be paid to the modification of the diffusivity of the plasma when the neutrals are described by the diffusion model. Direct comparison of the results from our fluid neutral model and those from a kinetic MC model is one of our future issues.

# Chapter 5
# Application of the Code

## 5.1 Recombination detachment

It was shown by the kinetic simulation that the supersonic flows could be driven by the effects of the radiative cooling and the radial diffusive loss of particle and energy as is shown in Fig. 16 [58]. In addition, it was predicted that supersonic flows might help the smoother transition from the attached to detached plasmas. First, we reproduce the detached plasma without the radial diffusive loss of particle and energy by using our 1D SOL-DIV plasma fluid code and studied its characteristics.

The parameters on the SOL-DIV plasma are shown in Table 4. The values in bold type are the basic ones when the other variable is changed. The parameters on the VD model are shown in Table 5. Figure 28 shows the profiles of the plasma

Table 4 Parameters of the plasma.

| Parameters | Values |
|---|---|
| The ion species | Hydrogen |
| Parallel SOL length $L_{SOL}$ | 35.2 m |
| Parallel plasma region length $L$ | 44 m |
| Separatrix area $A_{sep}$ | 40 $m^2$ |
| Flux tube width of SOL $d_{SOL}$ | 2 cm |
| Flux tube width of DIV $d_{DIV}$ | 2, **5**, 10 cm |
| Particle flux from the core $\Gamma_{sep}$ | variable |
| Heat flux from the core $P_{sep}$ | 2, **4**, 6 MW |
| Pitch angle $\theta$ | 6° |
| Impurity radiation model | Model A, Type A |
| $C_z$ in Model A | $\mathbf{10^{-13}}$, $10^{-12}$ $m^3/s$ |
| Impurity fraction $r_{imp}$ | 1 % |
| Effective ion charge $Z_{eff}$ | 1 |

Table 5 Parameters of the virtual divertor model.

| Parameters | Values |
|---|---|
| Parallel VD region length $L^{VD}$ | 6 m |
| Characteristic time of VD sink for plasma $\tau^{VD}$ | 5 μs |
| Characteristic time of VD sink for neutrals $\tau^{VD}$ | 1 μs |
| Artificial energy sink coefficient $g_{i,//}{}^{e,VD}$ | 3 |
| Artificial energy sink coefficient $g_{i,\perp}{}^{VD}$ | 1.2 |
| Artificial energy sink coefficient $g_e{}^{VD}$ | 2.5 |
| Recycling coefficient $\eta$ and $\eta_n$ | 1 |

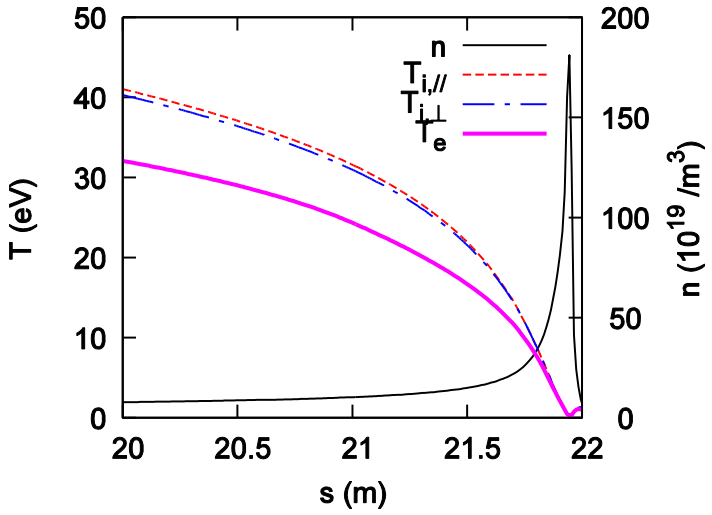


Figure 28 Profiles of plasma density $n$ (thin solid line), parallel ion temperature $T_{i,//}$ (broken line), perpendicular ion temperature $T_{i,\perp}$ (chain line) and electron temperature $T_e$ (thick solid) for $\Gamma_{sep} = 4\times10^{22}$ /s [63].

density, parallel/perpendicular ion temperature, electron temperature for $\Gamma_{sep} = 4\times10^{22}$ /s. Low density and low temperature plasma is formed just in front of the sheath entrance due to the volume recombination. Figure 29 shows the amplification factors $R$ for particle flux $\Gamma$ and the momentum flux $p$ defined by Eqs. (3.9) and (3.10) as functions of the particle flux from the core plasma $\Gamma_{sep}$. In Fig. 29 (a), the heat flux from the core plasma $P_{sep}$ is changed. In low $\Gamma_{sep}$ region, $R_\Gamma$ becomes higher as $\Gamma_{sep}$ increases. When $R_\Gamma$ reaches about 2.5, $R_p$ becomes almost zero and $R_\Gamma$ starts to decrease as $\Gamma_{sep}$ increases. Thus, the plasma transits from attached to the detached regime. In the experiments, however, high recycling

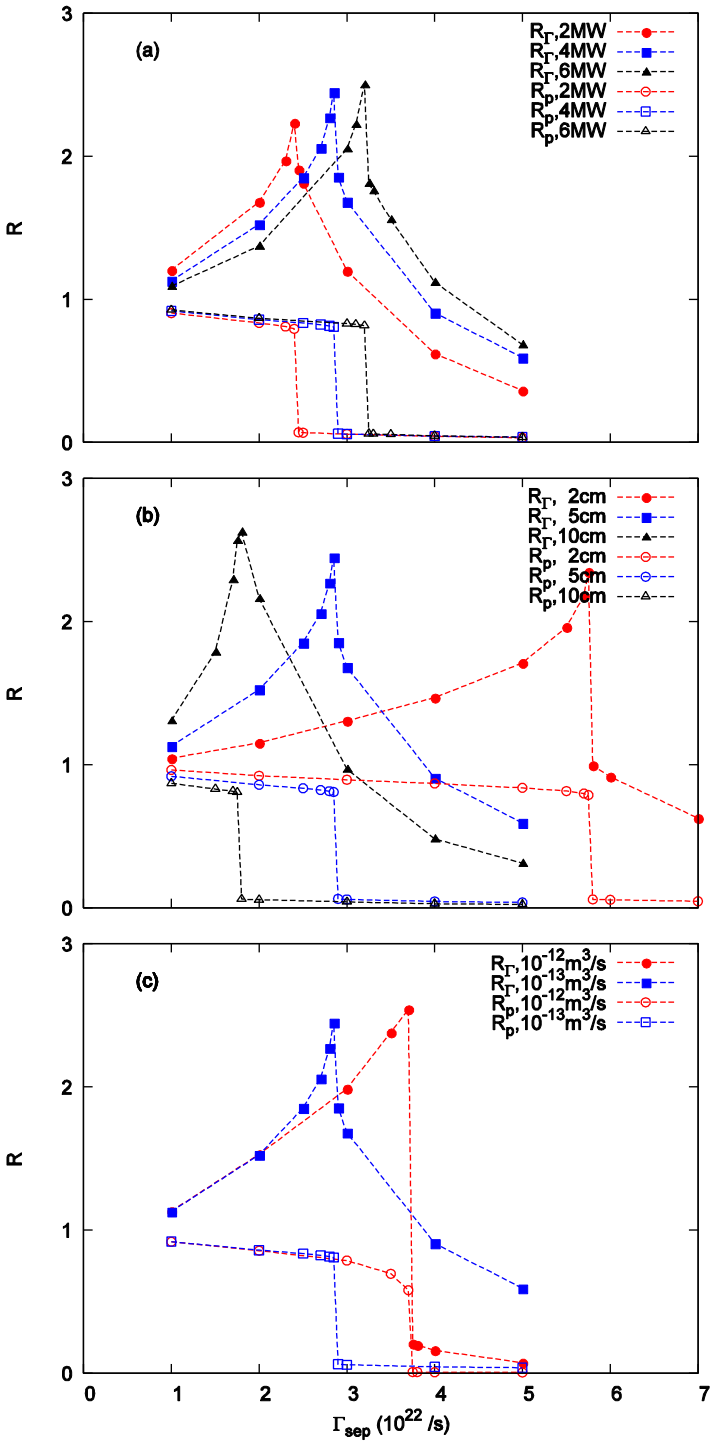


Figure 29 Flux amplification factor $R$ for particle ($\Gamma$) and momentum ($p$) as functions of the particle flux from the core plasma $\Gamma_{\text{sep}}$ for different values of (a) the heat flux from the core $P_{\text{sep}}$, (b) flux tube width in DIV $d_{\text{DIV}}$ and (c) $C_z$ [63].

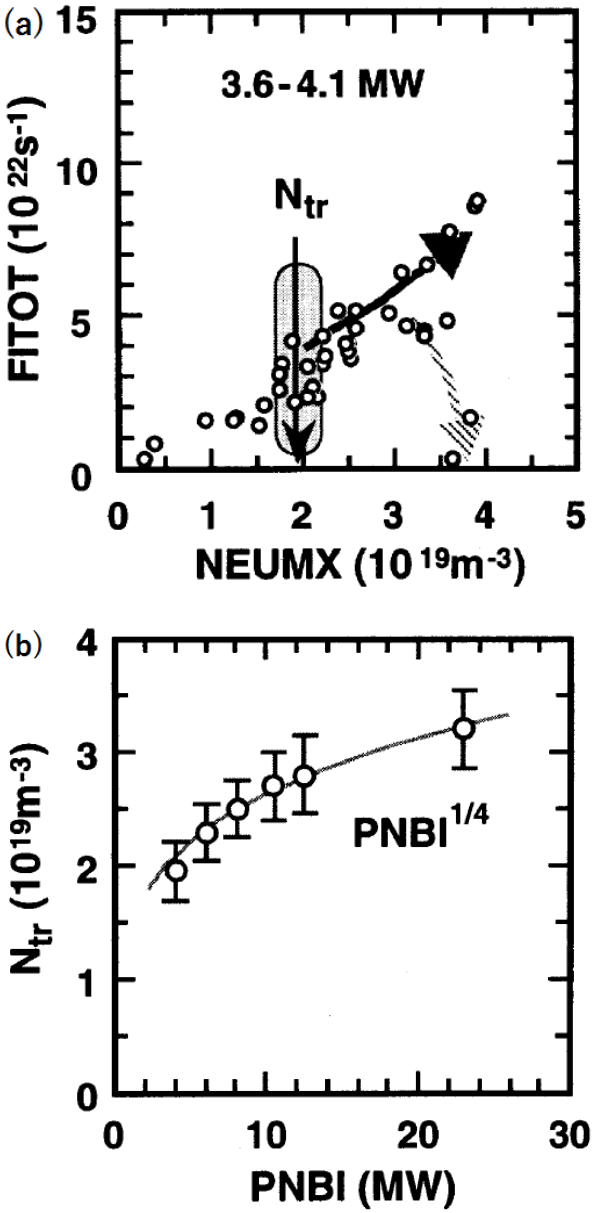


Figure 30 Database of JT-60U experiments; (a) total particle flux to the divertor plate as a function of line averaged electron density and (b) Transition density as a function of the heating power by neutral beam injection (NBI) [21].

regime where $R_{\Gamma} > \sim 5$ is observed before the transition to the detached regime. The existence of high recycling regime was verified numerically, too [67]. In the JT-60U experiments, it was found that the transition density where the plasma transits from low to high recycling regime was proportional to 1/4 power of the heating power [21] as shown in Fig. 30. In our results, the density at the stagnation

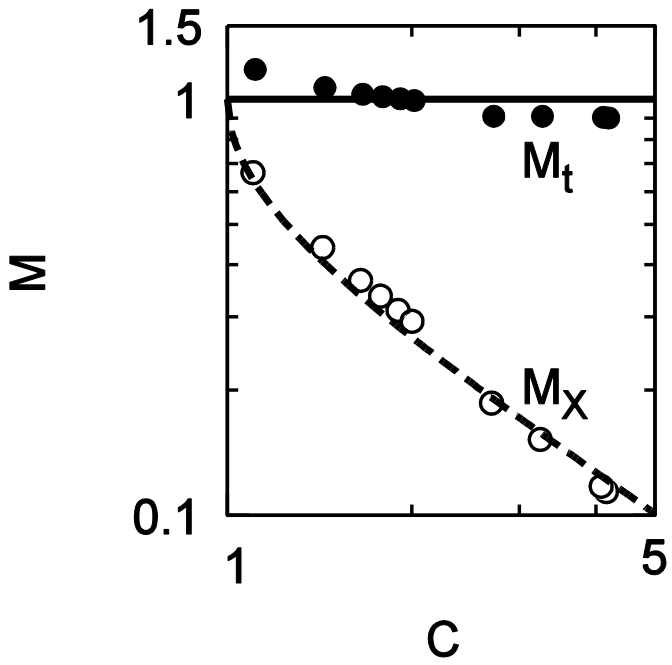


Figure 31 Mach number at the sheath entrance $M_t$ (closed circles) and at the X-point $M_X$ (open circles) as functions of $C$. The theoretical curves are given by Eqs. (3.12) and (3.13).

point ($s$ = 0) when $R_\Gamma$ reaches the maximum was proportional to $P_{sep}^{0.17}$ which is qualitatively similar to the observation in JT-60U experiments.

The dependence of the behavior of $R$ on $d_{DIV}$ is shown in Fig. 29 (b). As $d_{DIV}$ becomes large, the increase of $R_\Gamma$ in the low recycling regime becomes faster because the efficiency of neutral confinement rises. The maximum $R_\Gamma$, however, scarcely changes by $d_{DIV}$. The dependence of the behavior of $R$ on $C_z$ is shown in Fig. 29 (c). The increase of $R_\Gamma$ in the low recycling regime is slower when the radiation energy loss is stronger because the ionization rate is lower due to the lower electron density. In the detached regime, the reduction of $R_\Gamma$ is sharp due to the strong volume recombination. In these calculation conditions, we could not reproduce the high recycling regime.

Figure 31 shows the Mach number at the sheath entrance $M_t$ and at the X-point $M_X$ as functions of $C$. Here, the data for $M_t$ are picked in the VD region by 1 cm for numerical reason. The result agrees well with the theoretical curves but the supersonic flows are not obtained.

## 5.2 Effect of radial diffusive loss on detachment

As the candidates to reduce the particle flux to the divertor plates, radial diffusive loss of plasma particles is considered to be important in addition to the volume recombination [68]. Moreover, as is mentioned in the previous section, the radial diffusive loss tends to make the plasma flow supersonic.

Just like the particle and heat fluxes from the core plasma, we consider the effect of the radial diffusive loss by introducing the following sink terms to the fluid equations Eqs. (2.3)-(2.7) in DIV as follows;

$$S^{\perp} = -\frac{n}{\tau^{\perp}}, \tag{5.1}$$

$$M_{\mathrm{m}}^{\perp} = -\frac{m_{\mathrm{i}} n V}{\tau^{\perp}}, \tag{5.2}$$

$$Q_{\mathrm{i},//}^{\perp} = -\frac{1}{\tau^{\perp}}\left(\frac{1}{2} m_{\mathrm{i}} n V^2 + g_{\mathrm{i},//}^{\perp} \frac{1}{2} n T_{\mathrm{i},//}\right), \tag{5.3}$$

$$Q_{\mathrm{i},\perp}^{\perp} = -\frac{g_{\mathrm{i},\perp}^{\perp} n T_{\mathrm{i},\perp}}{\tau^{\perp}}, \tag{5.4}$$

$$Q_{\mathrm{e}}^{\perp} = -\frac{1}{\tau^{\perp}}\left(g_{\mathrm{e}}^{\perp} \frac{3}{2} n T_{\mathrm{e}}\right). \tag{5.5}$$

Here, the characteristic time of the radial diffusive loss $\tau^{\perp}$ is estimated as follows;

$$\tau^{\perp} = \frac{d_1^2}{D_{\perp}}. \tag{5.6}$$

The radial decay length on the side of private flux region (PFR) is denoted by $d_1$ and given as an input parameter in our code. As is shown schematically in Fig. 32, $d_1 = d_{\mathrm{DIV}}$ in the attached and full detached regimes and $d_1 < d_{\mathrm{DIV}}$ in the partially detached regime. The radial heat diffusion coefficients $g^{\perp}$ reflects the effect of the radial heat diffusion which are also input parameters.

First, we introduced the effect of radial diffusive loss in the no neutral conditions. The plasma parameters are shown in Table 6 and the parameters of VD model are the same as Table 2. Figure 33 shows the Mach number at the sheath entrance $M_{\mathrm{t}}$ and at the X-point $M_{\mathrm{X}}$ as functions of $C$. As $d_1/d_{\mathrm{DIV}}$ becomes small, Mt becomes large and supersonic flows are obtained. The results agree well with the theoretical curves given by Eqs. (3.12) and (3.13). We also introduced the effect of radial diffusive loss to the simulations in Sec. 5.1 with $D_{\perp}$ = 1 m$^2$/s, $d_1/d_{\mathrm{DIV}}$ = 0.5 and $g_{\perp}$ = 1. The result is shown with that in Sec 5.1 in Fig. 34.

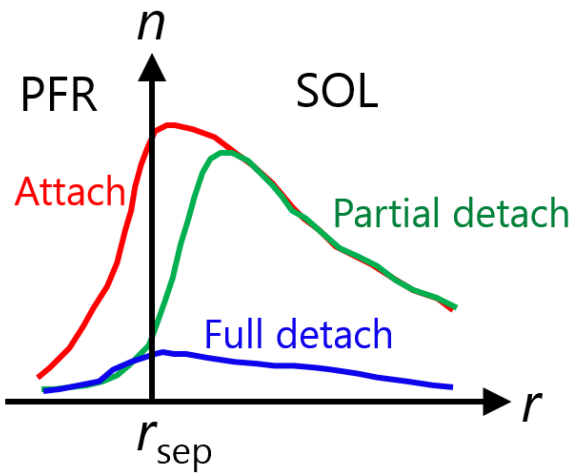


Figure 32 Schematic picture of radial density profile in attached, partial detached and full detached regimes.

Table 6 Parameters of the plasma

| Parameters | Values |
|---|---|
| The ion species | Hydrogen |
| Parallel SOL length $L_{SOL}$ | 35.2 m |
| Parallel plasma region length $L$ | 44 m |
| Separatrix area $A_{sep}$ | 40 $m^2$ |
| Flux tube width of SOL $d_{SOL}$ | 2 cm |
| Flux tube width of DIV $d_{DIV}$ | 5 cm |
| Radial decay length $d_1/d_{DIV}$ | 0.16 ~ $\infty$ |
| Radial particle diffusivity $D_\perp$ | 1 $m^2/s$ |
| Particle flux from the core $\Gamma_{sep}$ | $3\times10^{22}$ /s |
| Heat flux from the core $P_{sep}$ | 4 MW |

It shows that thanks to the radial diffusive loss of particles, the high recycling regime $R_\Gamma > 5$ appears. Neither in this case could we obtain the supersonic flows.

Next, we introduced the effects of radial heat diffusion by simply setting $g^\perp = 3$. In addition, we used the impurity radiation model of Model B (non-coronal) with Type A. The decay lengths $d_1/d_{DIV} = \infty$, 1, 0.5 and 0.3 are used. Other parameters are the same as Tables 4 and 5. The results are shown in Fig. 35. By using Model B instead of Model A, the high recycling regime appears even if

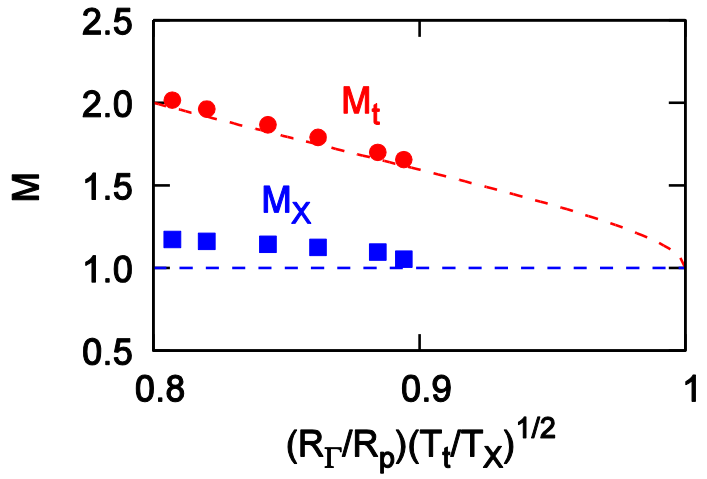


Figure 33 Mach number at the sheath entrance $M_t$ (circles) and at the X-point $M_X$ (squares) as functions of $C$. The theoretical curves are given by Eqs. (3.12) and (3.13).

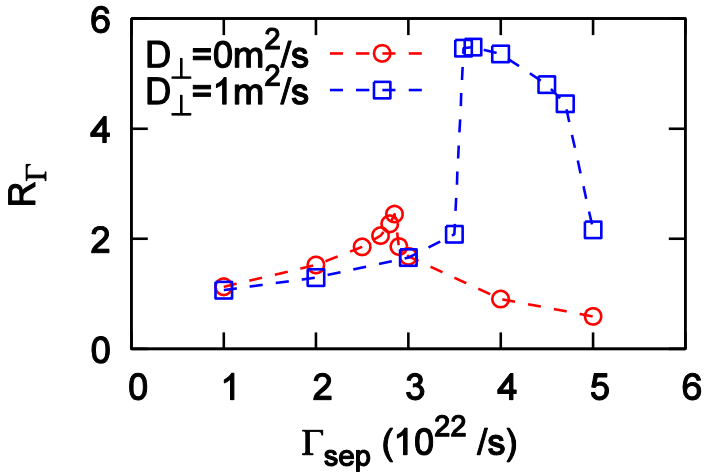


Figure 34 Particle flux amplification factors $R_\Gamma$ as functions of $\Gamma_{sep}$ for $D_\perp$ = 0 (circles) and 1 m$^2$/s (squares).

$d_1/d_{DIV} = \infty$. As $d_1/d_{DIV}$ becomes small, the maximum value of $R_\Gamma$ becomes large except for $d_1/d_{DIV}$ = 0.3. This is because the electron temperature near the sheath entrance becomes higher and the ionization is enhanced more. For $d_1/d_{DIV}$ = 0.5, the roll-over of $R_\Gamma$ occurs with non-zero $R_p$. Thus, by the effect of the radial diffusive loss of particle and heat, the roll-over of $R_\Gamma$ (or the particle flux to the divertor plates) becomes moderate. In these cases, however, supersonic flows are not obtained.

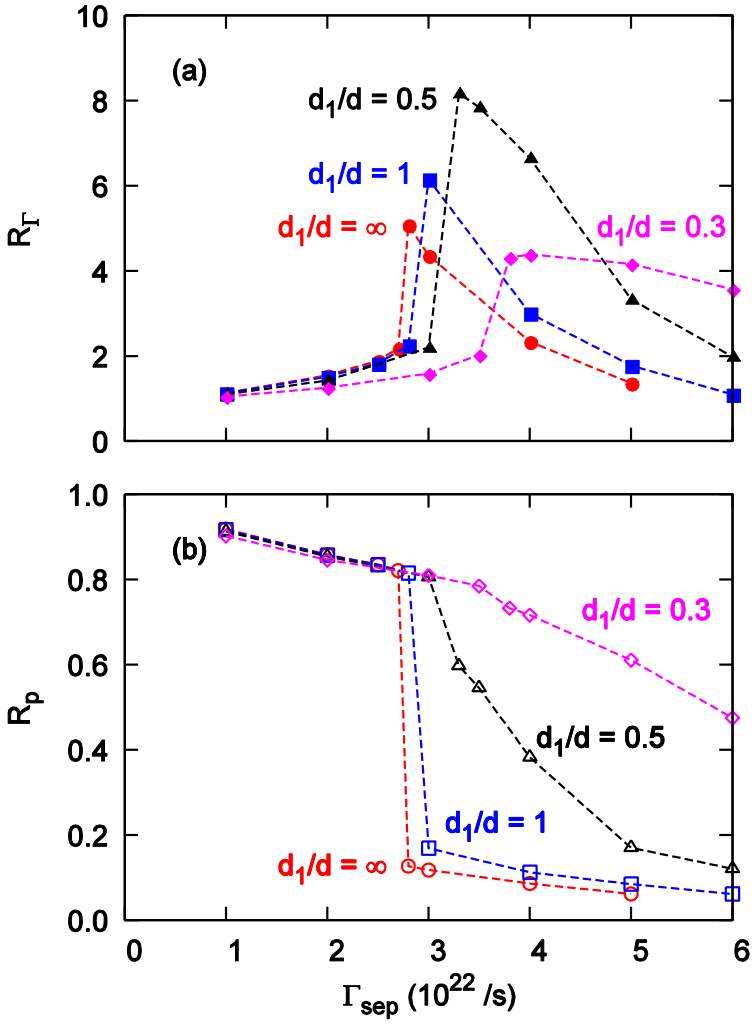


Figure 35 Particle and momentum flux amplification factors $R$ as functions of $\Gamma_{sep}$ for $d_1/d_{DIV} = \infty$, 1, 0.5 and 0.3.

Finally, we enhanced the effect of impurity radiation by using the Model B (non-coronal) with Type B and setting $r_{imp}$ = 3 %. When $\Gamma_{sep}$ = $5\times10^{22}$ /s is set, the motion of the fronts are observed as shown in Fig. 36. In this case, the steady state solution is not obtained but the Mach number at the sheath entrance becomes larger than unity. By introducing the radial heat source, the motion of the fronts can be stabilized and steady state solution might be obtained [44] which is explained briefly in Appendix A.4 and one of our future issues.

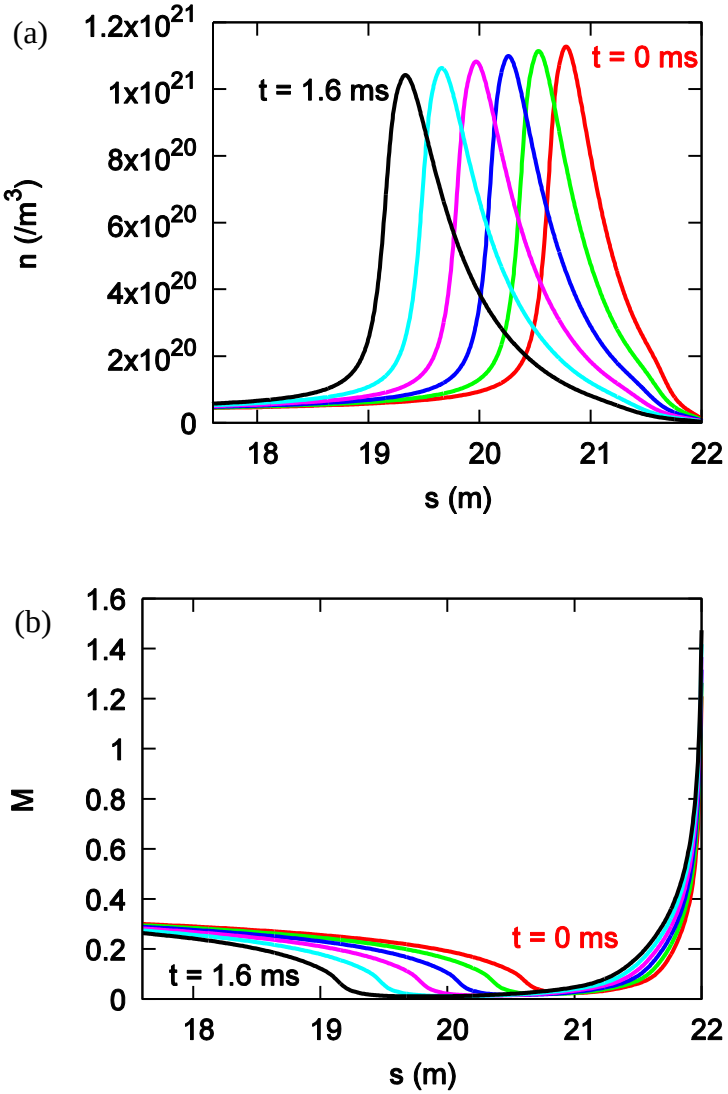


Figure 36 Time evolution of the profiles of (a) plasma density $n$ and (b) Mach number $M$.

# Chapter 6
# Conclusion

In order to commercialize the tokamak fusion reactors, reduction of the divertor heat load is one of the most important issues. Detached plasmas can reduce the heat load dramatically, so that the mechanism of them is researched worldwide. For the quantitative prediction of the heat load on the divertor in the future devices, Scrape-off-layer (SOL)-Divertor (DIV) plasma code packages are utilized. The results of them, however, do not satisfactorily agree with those of experiments.

We focus on the SOL-DIV plasma fluid model. Code packages are generally using the Braginskii's equations which assume that the temperature is almost isotropic. Due to this, the effect of pressure anisotropy is approximated by parallel viscous flux which makes the parallel momentum transport equation the second-order differential. Thus, the Mach number at the sheath entrance is required to be given as a boundary condition.

We developed a one-dimensional (1D) SOL-DIV plasma fluid code which introduces ion temperature anisotropy. Since the parallel momentum transport equation becomes the first-order differential, the boundary condition on the Mach number at the sheath entrance becomes unnecessary. Instead, we developed and incorporated a virtual divertor (VD) model. In this model, an artificial region (VD region) with artificial sinks for particle, momentum and energy is set beyond the sheath entrance.

In Chapter 2, the plasma fluid model with anisotropic ion temperature is described. The detail of the VD model is also explained. By using a periodic boundary condition, treatment of the complex plasma-wall boundary in the real device becomes much easier. The numerical scheme using periodic boundary condition is presented.

In Chapter 3, the validity of the VD model is shown about the Bohm criterion and the sheath heat transmission factors. Some preliminary results by using the plasma fluid model are also presented about the anisotropy of ion temperature, supersonic flows due to radiative cooling and the validity of the viscosity approximation.

In Chapter 4, the numerical model of neutral fluid is described which works with the VD model. This model is based on the first-flight corrected diffusion

(FFCD) model. The simple radiation cooling model is also explained. The validity of the VD model is shown about the boundary condition for the diffusion neutrals. Some preliminary results are presented about the effect of neutrals on the ion temperature anisotropy and the modification of the diffusivity of neutrals.

In Chapter 5, we show the results on the recombination detachment as an application of our code. We investigated the effect of supersonic flow on the transit from the attached to the detached regime. The formation of the low temperature and low density plasma near the sheath entrance is seen and roll-over of the particle flux amplification factor is reproduced. The high recycling regime did not at first appear. The dependence of the behavior of the particle flux amplification factor on the heat flux from the core plasma, flux tube width in DIV and the strength of the radiative cooling was investigated. By introducing the effect of radial diffusive loss or the more accurate impurity radiation model, we successfully obtained the high recycling regime. It is found that this effect makes the roll-over of the particle flux moderate. At this stage, the supersonic flow was not observed. By enhancing the impurity radiation, the motion of the fronts was observed and supersonic flow generated near the sheath entrance although steady state solution is not yet obtained.

In order to simulate more general plasma, we need to consider the effects of plasma current and the inhomogeneous magnetic field. For the transient simulations, such as edge localized modes (ELMs), $\tau^{\mathrm{VD}}$ needs to be much shorter than the characteristic times of the focused phenomenon. In order to mitigate the computational time, the inhomogeneous grid is required to be incorporated.

# Appendix

## A.1 Derivation of the basic plasma equations

The basic plasma equations, Eq. (2.3)-(2.7) are derived one-by-one from the following Boltzmann equation of parallel component to the magnetic field;

$$\frac{\partial f}{\partial t} + v_{//}\frac{\partial f}{\partial s} + \frac{qE}{m}\frac{\partial f}{\partial v_{//}} = \left.\frac{\partial f}{\partial t}\right|_{\mathrm{coll}} + \hat{S}. \tag{A.1}$$

Here, the neutral particles are not considered for simplicity. The electric charge of the particle species focused on is denoted by $q$ ($q = e$ for ions and $q = -e$ for electrons, respectively). The particle source term in a phase space is denoted by $\hat{S}$. For the velocity distribution function $f$, we assume that it is described by a drifting bi-Maxwellian with different $T_{//}$ and $T_{\perp}$ to the first-order as follows [15];

$$f = n\frac{\beta_{\perp}\beta_{//}^{1/2}}{\pi^{3/2}}\mathrm{e}^{-\beta_{//}u_{//}^2}\mathrm{e}^{-\beta_{\perp}v_{\perp}^2}, \tag{A.2}$$

$$\beta = \frac{m}{2T}, \tag{A.3}$$

$$u_{//} = v_{//} - V. \tag{A.4}$$

Here, $u_{//}$ is the random velocity.

*Equation of continuity*

Equation of continuity, Eq. (2.3), is derived by multiplying Eq. (A.1) by d$\boldsymbol{v}$ and integrating. The collisional term does not contribute to the particle source. By denoting the particle source/sink in the real space by $S$, we obtain the following;

$$\frac{\partial n}{\partial t} + \frac{\partial}{\partial s}(nV) = S. \tag{A.5}$$

*Equation of parallel momentum transport*

Equation of parallel momentum transport of the plasma is derived by taking the summation of those for ion and electron. The equation for ion is derived by

multiplying Eq. (A.1) by $m_{\mathrm{i}}v_{//}\mathrm{d}\boldsymbol{v}$ and integrating. The first term gives;

$$\begin{aligned}
&\int m_{\mathrm{i}}v_{//}\frac{\partial f}{\partial t}\mathrm{d}\boldsymbol{v} = \frac{\partial}{\partial t}m_{\mathrm{i}}\int_{-\infty}^{\infty}v_{//}\mathrm{d}v_{//}\int_{0}^{\infty}2\pi v_{\perp}f\mathrm{d}v_{\perp} \\
&= \frac{\partial}{\partial t}m_{\mathrm{i}}n\frac{2\beta_{\mathrm{i},\perp}\beta_{\mathrm{i},//}^{1/2}}{\pi^{1/2}}\int_{-\infty}^{\infty}\mathrm{d}u_{//}\left(u_{//}+V\right)\mathrm{e}^{-\beta_{\mathrm{i},//}u_{//}^{2}}\int_{0}^{\infty}\mathrm{d}v_{\perp}v_{\perp}\mathrm{e}^{-\beta_{\mathrm{i},\perp}v_{\perp}^{2}} \\
&= \frac{\partial}{\partial t}m_{\mathrm{i}}nV.
\end{aligned} \tag{A.6}$$

The second term gives;

$$\begin{aligned}
&\int m_{\mathrm{i}}v_{//}^{2}\frac{\partial f}{\partial s}\mathrm{d}\boldsymbol{v} = \frac{\partial}{\partial s}m_{\mathrm{i}}\int_{-\infty}^{\infty}v_{//}^{2}\mathrm{d}v_{//}\int_{0}^{\infty}2\pi v_{\perp}f\mathrm{d}v_{\perp} \\
&= \frac{\partial}{\partial s}m_{\mathrm{i}}n\frac{2\beta_{\mathrm{i},\perp}\beta_{\mathrm{i},//}^{1/2}}{\pi^{1/2}}\int_{-\infty}^{\infty}\mathrm{d}u_{//}\left(u_{//}+V\right)^{2}\mathrm{e}^{-\beta_{\mathrm{i},//}u_{//}^{2}}\int_{0}^{\infty}\mathrm{d}v_{\perp}v_{\perp}\mathrm{e}^{-\beta_{\mathrm{i},\perp}v_{\perp}^{2}} \\
&= \frac{\partial}{\partial s}\left(m_{\mathrm{i}}nV^{2}+nT_{\mathrm{i},//}\right).
\end{aligned} \tag{A.7}$$

The third term gives;

$$\begin{aligned}
&\int m_{\mathrm{i}}v_{//}\frac{eE}{m_{\mathrm{i}}}\frac{\partial f}{\partial v_{//}}\mathrm{d}\boldsymbol{v} = eE\int\left[\frac{\partial}{\partial v_{//}}\left(v_{//}f\right)-f\right]\mathrm{d}\boldsymbol{v} \\
&= eE\int_{0}^{\infty}2\pi v_{\perp}\mathrm{d}v_{\perp}\int_{-\infty}^{\infty}\frac{\partial}{\partial v_{//}}\left(v_{//}f\right)\mathrm{d}v_{//}-eE\int f\mathrm{d}\boldsymbol{v} \\
&= -eEn.
\end{aligned} \tag{A.8}$$

The collisional term in the right hand side gives the thermal force term due to the Coulomb collisions in the assumption of no plasma current as follows [37];

$$R_{T} = 0.71n\frac{\partial T_{\mathrm{e}}}{\partial s}. \tag{A.9}$$

By combining Eqs. (A.6)-(A.9) and denoting the momentum source/sink term by Mm, following equation of parallel momentum transport for ion is obtained;

$$\frac{\partial}{\partial t}\left(m_{\mathrm{i}}nV\right)+\frac{\partial}{\partial s}\left(m_{\mathrm{i}}nV^{2}+nT_{\mathrm{i},//}\right)-eEn = R_{T}+M_{\mathrm{m}}. \tag{A.10}$$

Similarly, following equation of parallel momentum transport for electron, known as the generalized Ohm's law, is obtained;

$$\frac{\partial}{\partial s}\left(nT_{\mathrm{e}}\right)+eEn=-R_T. \tag{A.11}$$

In this equation, the inertia term and the dynamic pressure term are dropped due to its smallness. The electron temperature is assumed to be isotropic due to its strong self-collisionality. The summation of Eqs. (A.10) and (A.11) becomes the following;

$$\frac{\partial}{\partial t}\left(m_{\mathrm{i}}nV\right)+\frac{\partial}{\partial s}\left(m_{\mathrm{i}}nV^2+nT_{\mathrm{i},//}+nT_{\mathrm{e}}\right)=M_{\mathrm{m}}. \tag{A.12}$$

*Equation of parallel ion energy transport*

Equation of parallel ion energy transport is derived by multiplying Eq. (A.1) by $(1/2)m_{\mathrm{i}}v_{//}^2\mathrm{d}\boldsymbol{v}$ and integrating. The first term gives;

$$\begin{aligned}
&\int\frac{1}{2}m_{\mathrm{i}}v_{//}^2\frac{\partial f}{\partial t}\mathrm{d}\boldsymbol{v}=\frac{\partial}{\partial t}\frac{1}{2}m_{\mathrm{i}}\int_{-\infty}^{\infty}v_{//}^2\mathrm{d}v_{//}\int_0^{\infty}2\pi v_{\perp}f\mathrm{d}v_{\perp}\\
&=\frac{\partial}{\partial t}m_{\mathrm{i}}n\frac{\beta_{\mathrm{i},\perp}\beta_{\mathrm{i},//}^{1/2}}{\pi^{1/2}}\int_{-\infty}^{\infty}\mathrm{d}u_{//}\left(u_{//}+V\right)^2\mathrm{e}^{-\beta_{\mathrm{i},//}u_{//}^2}\int_0^{\infty}\mathrm{d}v_{\perp}v_{\perp}\mathrm{e}^{-\beta_{\mathrm{i},\perp}v_{\perp}^2}\\
&=\frac{\partial}{\partial t}\left(\frac{1}{2}m_{\mathrm{i}}nV^2+\frac{m_{\mathrm{i}}n}{4\beta_{\mathrm{i},//}}\right)=\frac{\partial}{\partial t}\left(\frac{1}{2}m_{\mathrm{i}}nV^2+\frac{1}{2}nT_{\mathrm{i},//}\right).
\end{aligned} \tag{A.13}$$

The second term gives;

$$\begin{aligned}
&\int\frac{1}{2}m_{\mathrm{i}}v_{//}^3\frac{\partial f}{\partial s}\mathrm{d}\boldsymbol{v}=\int\frac{1}{2}m_{\mathrm{i}}\left(u_{//}+V\right)^3\frac{\partial f}{\partial s}\mathrm{d}\boldsymbol{v}\\
&=\frac{\partial}{\partial s}\frac{1}{2}m_{\mathrm{i}}\int_{-\infty}^{\infty}\left(V^3+3u_{//}^2V\right)\mathrm{d}u_{//}\int_0^{\infty}2\pi v_{\perp}f\mathrm{d}v_{\perp}+\frac{\partial}{\partial s}\int\frac{1}{2}m_{\mathrm{i}}u_{//}^3f\mathrm{d}\boldsymbol{v}\\
&=\frac{\partial}{\partial s}m_{\mathrm{i}}n\frac{\beta_{\mathrm{i},\perp}\beta_{\mathrm{i},//}^{1/2}}{\pi^{1/2}}\int_{-\infty}^{\infty}\mathrm{d}u_{//}\left(V^3+3u_{//}^2V\right)\mathrm{e}^{-\beta_{\mathrm{i},//}u_{//}^2}\int_0^{\infty}\mathrm{d}v_{\perp}v_{\perp}\mathrm{e}^{-\beta_{\mathrm{i},\perp}v_{\perp}^2}\\
&+\frac{\partial}{\partial s}\frac{1}{2}m_{\mathrm{i}}n\left\langle u_{//}^3\right\rangle\\
&=\frac{\partial}{\partial s}\left(\frac{1}{2}m_{\mathrm{i}}nV^2+\frac{3}{2}nT_{\mathrm{i},//}\right)V+\frac{\partial}{\partial s}\left(-c\kappa_{\mathrm{i}}^{\mathrm{SH}}\frac{\partial T_{\mathrm{i},//}}{\partial s}\right).
\end{aligned} \tag{A.14}$$

Here, in the derivation of the conductive heat flux, kinetic effect is considered as follows;

$$
\begin{aligned}
&\frac{1}{2}m_{\mathrm{i}}n\left\langle u_{//}^{3}\right\rangle=\frac{1}{2}m_{\mathrm{i}}\left(\int_{u_{//}=-\infty}^{u_{//}=0}u_{//}^{3}f\mathrm{d}\boldsymbol{v}+\int_{u_{//}=0}^{u_{//}=\infty}u_{//}^{3}f\mathrm{d}\boldsymbol{v}\right)\\
&\approx\frac{1}{2}m_{\mathrm{i}}\left(\int_{u_{//}=-\infty}^{u_{//}=0}u_{//}^{3}f\left(T_{\mathrm{i},//,+}\right)\mathrm{d}\boldsymbol{v}+\int_{u_{//}=0}^{u_{//}=\infty}u_{//}^{3}f\left(T_{\mathrm{i},//,-}\right)\mathrm{d}\boldsymbol{v}\right)\\
&=\frac{1}{2}m_{\mathrm{i}}\frac{n}{2\pi^{1/2}}\left[\left(\frac{2T_{\mathrm{i},//,-}}{m_{\mathrm{i}}}\right)^{3/2}-\left(\frac{2T_{\mathrm{i},//,+}}{m_{\mathrm{i}}}\right)^{3/2}\right]\\
&\approx\frac{3\sqrt{2}}{4\sqrt{\pi}}n\sqrt{\frac{T_{\mathrm{i},//}}{m_{\mathrm{i}}}}\left(T_{\mathrm{i},//,-}-T_{\mathrm{i},//,+}\right)\approx-c_{//}n\sqrt{\frac{T_{\mathrm{i},//}}{m_{\mathrm{i}}}}\frac{\partial T_{\mathrm{i},//}}{\partial s}\sqrt{\frac{T_{\mathrm{i},//}}{m_{\mathrm{i}}}}\tau_{\mathrm{i}}\\
&=-c_{//}\frac{nT_{\mathrm{i},//}\tau_{\mathrm{i}}}{m_{\mathrm{i}}}\frac{\partial T_{\mathrm{i},//}}{\partial s}=-c\kappa_{\mathrm{i}}^{\mathrm{SH}}\frac{\partial T_{\mathrm{i},//}}{\partial s}.
\end{aligned}
\tag{A.15}
$$

Here, the subscripts "+" and "-" represent the special deviation by $\delta s \sim (T_{\mathrm{i},//}/m_{\mathrm{i}})^{1/2}\tau_{\mathrm{i}}$. An ambiguity remains in the fraction of the conduction heat flux for $T_{\mathrm{i},//}$ which is determined by the coefficient $c$. The third term gives;

$$
\begin{aligned}
&\int\frac{1}{2}m_{\mathrm{i}}v_{//}^{2}\frac{eE}{m_{\mathrm{i}}}\frac{\partial f}{\partial v_{//}}\mathrm{d}\boldsymbol{v}=\frac{eE}{2}\int\left[\frac{\partial}{\partial v_{//}}\left(v_{//}^{2}f\right)-2v_{//}f\right]\mathrm{d}\boldsymbol{v}\\
&=\frac{eE}{2}\int_{0}^{\infty}2\pi v_{\perp}\mathrm{d}v_{\perp}\int_{-\infty}^{\infty}\frac{\partial}{\partial v_{//}}\left(v_{//}^{2}f\right)\mathrm{d}v_{//}-eE\int v_{//}f\mathrm{d}\boldsymbol{v}\\
&=-eEnV.
\end{aligned}
\tag{A.16}
$$

The collisional term gives three kinds of terms; (a) pressure anisotropy relaxation term $Q_{\mathrm{rlx}} = n(T_{\mathrm{i},\perp} - T_{\mathrm{i},//})/\tau_{\mathrm{rlx}}$ [45, 46], (b) joule heating term $Q_R = R_T V$ and (c) thermal equilibrium term $Q_{\mathrm{eq},//} = (m_{\mathrm{e}}/m_{\mathrm{i}})n(T_{\mathrm{e}} - T_{\mathrm{i},//})/\tau_{\mathrm{e}}$. By combining Eqs. (A.13)-(A.16) and denoting the heat source/sink by $Q_{\mathrm{i},//}$, following parallel ion energy transport equation is obtained;

$$
\begin{aligned}
&\frac{\partial}{\partial t}\left(\frac{1}{2}m_{\mathrm{i}}nV^{2}+\frac{1}{2}nT_{\mathrm{i},//}\right)+\frac{\partial}{\partial s}\left(\frac{1}{2}m_{\mathrm{i}}nV^{2}+\frac{3}{2}nT_{\mathrm{i},//}\right)V\\
&+\frac{\partial}{\partial s}\left(-c\kappa_{\mathrm{i}}^{\mathrm{SH}}\frac{\partial T_{\mathrm{i},//}}{\partial s}\right)=Q_{\mathrm{i},//}+Q_{\mathrm{rlx}}+Q_{\mathrm{eq},//}+Q_{R}+eEnV.
\end{aligned}
\tag{A.17}
$$

By substituting Eq. (A.11) to Eq. (A.17), following equation is derived;

$$\begin{aligned}
&\frac{\partial}{\partial t}\left(\frac{1}{2}m_{\mathrm{i}}nV^2+\frac{1}{2}nT_{\mathrm{i},//}\right)+\frac{\partial}{\partial s}\left(\frac{1}{2}m_{\mathrm{i}}nV^2+\frac{3}{2}nT_{\mathrm{i},//}\right)V\\
&+\frac{\partial}{\partial s}\left(-c\kappa_{\mathrm{i}}^{\mathrm{SH}}\frac{\partial T_{\mathrm{i},//}}{\partial s}\right)\\
&=Q_{\mathrm{i},//}+\frac{n\left(T_{\mathrm{i},\perp}-T_{\mathrm{i},//}\right)}{\tau_{\mathrm{rlx}}}+\frac{m_{\mathrm{e}}}{m_{\mathrm{i}}}\frac{n\left(T_{\mathrm{e}}-T_{\mathrm{i},//}\right)}{\tau_{\mathrm{e}}}-V\frac{\partial}{\partial s}\left(nT_{\mathrm{e}}\right).
\end{aligned}\tag{A.18}$$

In a similar way, following parallel electron energy transport equation is derived;

$$\begin{aligned}
&\frac{\partial}{\partial t}\left(\frac{1}{2}nT_{\mathrm{e},//}\right)+\frac{\partial}{\partial s}\left(\frac{3}{2}nT_{\mathrm{e},//}\right)V+\frac{\partial}{\partial s}\left(-c\kappa_{\mathrm{e}}^{\mathrm{SH}}\frac{\partial T_{\mathrm{e},//}}{\partial s}\right)\\
&=Q_{\mathrm{e},//}+\frac{n\left(T_{\mathrm{e},\perp}-T_{\mathrm{e},//}\right)}{\tau_{\mathrm{e,rlx}}}+\frac{m_{\mathrm{e}}}{m_{\mathrm{i}}}\frac{n\left(T_{\mathrm{i}}-T_{\mathrm{e},//}\right)}{\tau_{\mathrm{e}}}+V\frac{\partial}{\partial s}\left(nT_{\mathrm{e}}\right).
\end{aligned}\tag{A.19}$$

*Equation of perpendicular ion energy transport*

Equation of perpendicular ion energy transport is derived by multiplying Eq. (A.1) by $(1/2)m_{\mathrm{i}}v_{\perp}^2\mathrm{d}\boldsymbol{v}$ and integrating. The first term gives;

$$\begin{aligned}
&\int\frac{1}{2}m_{\mathrm{i}}v_{\perp}^2\frac{\partial f}{\partial t}\mathrm{d}\boldsymbol{v}=\frac{\partial}{\partial t}\frac{1}{2}m_{\mathrm{i}}\int_{-\infty}^{\infty}\mathrm{d}v_{//}\int_0^{\infty}2\pi v_{\perp}^3 f\mathrm{d}v_{\perp}\\
&=\frac{\partial}{\partial t}m_{\mathrm{i}}n\frac{\beta_{\mathrm{i},\perp}\beta_{\mathrm{i},//}^{1/2}}{\pi^{1/2}}\int_{-\infty}^{\infty}\mathrm{d}u_{//}\mathrm{e}^{-\beta_{\mathrm{i},//}u_{//}^2}\int_0^{\infty}\mathrm{d}v_{\perp}v_{\perp}^3\mathrm{e}^{-\beta_{\mathrm{i},\perp}v_{\perp}^2}\\
&=\frac{\partial}{\partial t}\left(\frac{m_{\mathrm{i}}n}{2\beta_{\mathrm{i},\perp}}\right)=\frac{\partial}{\partial t}\left(nT_{\mathrm{i},\perp}\right).
\end{aligned}\tag{A.20}$$

The second term gives;

$$\begin{aligned}
&\int\frac{1}{2}m_{\mathrm{i}}v_{\perp}^2v_{//}\frac{\partial f}{\partial s}\mathrm{d}\boldsymbol{v}=\int\frac{1}{2}m_{\mathrm{i}}v_{\perp}^2\left(u_{//}+V\right)\frac{\partial f}{\partial s}\mathrm{d}\boldsymbol{v}\\
&=\frac{\partial}{\partial s}\frac{1}{2}m_{\mathrm{i}}V\int_{-\infty}^{\infty}\mathrm{d}v_{//}\int_0^{\infty}2\pi v_{\perp}^3 f\mathrm{d}v_{\perp}+\frac{\partial}{\partial s}\int\frac{1}{2}m_{\mathrm{i}}u_{//}v_{\perp}^2 f\mathrm{d}\boldsymbol{v}\\
&=\frac{\partial}{\partial s}m_{\mathrm{i}}nV\frac{\beta_{\mathrm{i},\perp}\beta_{\mathrm{i},//}^{1/2}}{\pi^{1/2}}\int_{-\infty}^{\infty}\mathrm{d}u_{//}\mathrm{e}^{-\beta_{\mathrm{i},//}u_{//}^2}\int_0^{\infty}\mathrm{d}v_{\perp}v_{\perp}^3\mathrm{e}^{-\beta_{\mathrm{i},\perp}v_{\perp}^2}+\frac{\partial}{\partial s}\frac{1}{2}m_{\mathrm{i}}n\left\langle u_{//}v_{\perp}^2\right\rangle\\
&=\frac{\partial}{\partial s}\left(nT_{\mathrm{i},\perp}V\right)+\frac{\partial}{\partial s}\left[-\left(1-c\right)\kappa_{\mathrm{i}}^{\mathrm{SH}}\frac{\partial T_{\mathrm{i},\perp}}{\partial s}\right].
\end{aligned}\tag{A.21}$$

Here again, the kinetic effect is considered in the derivation of conductive heat flux as follows;

$$
\begin{aligned}
&\frac{1}{2}m_{\mathrm{i}}n\left\langle u_{//}v_{\perp}^{2}\right\rangle=\frac{1}{2}m_{\mathrm{i}}\left(\int_{u_{//}=-\infty}^{u_{//}=0}u_{//}v_{\perp}^{2}\,f\mathrm{d}\boldsymbol{v}+\int_{u_{//}=0}^{u_{//}=\infty}u_{//}v_{\perp}^{2}\,f\mathrm{d}\boldsymbol{v}\right)\\
&\approx\frac{1}{2}m_{\mathrm{i}}\left(\int_{u_{//}=-\infty}^{u_{//}=0}u_{//}v_{\perp}^{2}\,f\left(T_{\mathrm{i},\perp,+}\right)\mathrm{d}\boldsymbol{v}+\int_{u_{//}=0}^{u_{//}=\infty}u_{//}v_{\perp}^{2}\,f\left(T_{\mathrm{i},\perp,-}\right)\mathrm{d}\boldsymbol{v}\right)\\
&=\frac{1}{2}m_{\mathrm{i}}\,\frac{n}{2\pi^{1/2}}\sqrt{\frac{2T_{\mathrm{i},//}}{m_{\mathrm{i}}}}\left(\frac{2T_{\mathrm{i},\perp,-}}{m_{\mathrm{i}}}-\frac{2T_{\mathrm{i},\perp,+}}{m_{\mathrm{i}}}\right)\\
&=\frac{\sqrt{2}}{2\sqrt{\pi}}n\sqrt{\frac{T_{\mathrm{i},//}}{m_{\mathrm{i}}}}\left(T_{\mathrm{i},\perp,-}-T_{\mathrm{i},\perp,+}\right)\approx-c_{\perp}n\sqrt{\frac{T_{\mathrm{i},//}}{m_{\mathrm{i}}}}\,\frac{\partial T_{\mathrm{i},\perp}}{\partial s}\sqrt{\frac{T_{\mathrm{i},//}}{m_{\mathrm{i}}}}\tau_{\mathrm{i}}\\
&=-c_{\perp}\frac{nT_{\mathrm{i},//}\tau_{\mathrm{i}}}{m_{\mathrm{i}}}\frac{\partial T_{\mathrm{i},\perp}}{\partial s}=-\left(1-c\right)\kappa_{\mathrm{i}}^{\mathrm{SH}}\,\frac{\partial T_{\mathrm{i},\perp}}{\partial s}.
\end{aligned}
\tag{A.22}
$$

Here, the coefficient (1 - $c$) is for the summation of the conductive heat fluxes of parallel and perpendicular ion temperature to accord with $(\partial/\partial s)(-\kappa_{\mathrm{i}}^{\mathrm{SH}}(\partial T_{\mathrm{i}}/\partial s))$ when the ion temperature is almost isotropic, $T_{\mathrm{i},//}\approx T_{\mathrm{i},\perp}\approx T_{\mathrm{i}}$. The third term gives;

$$
\int\frac{1}{2}m_{\mathrm{i}}v_{\perp}^{2}\,\frac{eE}{m_{\mathrm{i}}}\frac{\partial f}{\partial v_{//}}\mathrm{d}\boldsymbol{v}=\frac{eE}{2}\int_{0}^{\infty}2\pi v_{\perp}^{3}\mathrm{d}v_{\perp}\int_{-\infty}^{\infty}\frac{\partial f}{\partial v_{//}}\mathrm{d}v_{//}=0.
\tag{A.23}
$$

The collisional term gives two kinds of terms; (a) pressure anisotropy relaxation term $-Q_{\mathrm{rlx}}=-n(T_{\mathrm{i},\perp}-T_{\mathrm{i},//})/\tau_{\mathrm{rlx}}$ [45, 46] and (b) thermal equilibrium term $Q_{\mathrm{eq},\perp}=(2m_{\mathrm{e}}/m_{\mathrm{i}})n(T_{\mathrm{e}}-T_{\mathrm{i},\perp})/\tau_{\mathrm{e}}$. By combining Eqs. (A.20)-(A.23), and denoting the heat source/sink by $Q_{\mathrm{i},\perp}$, following equation of perpendicular ion energy transport is obtained;

$$
\begin{aligned}
&\frac{\partial}{\partial t}\left(nT_{\mathrm{i},\perp}\right)+\frac{\partial}{\partial s}\left(nT_{\mathrm{i},\perp}V\right)+\frac{\partial}{\partial s}\left[-\left(1-c\right)\kappa_{\mathrm{i}}^{\mathrm{SH}}\,\frac{\partial T_{\mathrm{i},\perp}}{\partial s}\right]\\
&=Q_{\mathrm{i},\perp}-\frac{n\left(T_{\mathrm{i},\perp}-T_{\mathrm{i},//}\right)}{\tau_{\mathrm{rlx}}}+\frac{2m_{\mathrm{e}}}{m_{\mathrm{i}}}\frac{n\left(T_{\mathrm{e}}-T_{\mathrm{i},\perp}\right)}{\tau_{\mathrm{e}}}.
\end{aligned}
\tag{A.24}
$$

In a similar way, following equation of perpendicular electron energy transport is obtained;

$$
\begin{aligned}
&\frac{\partial}{\partial t}\left(nT_{\mathrm{e},\perp}\right)+\frac{\partial}{\partial s}\left(nT_{\mathrm{e},\perp}V\right)+\frac{\partial}{\partial s}\left[-\left(1-c\right)\kappa_{\mathrm{e}}^{\mathrm{SH}}\,\frac{\partial T_{\mathrm{e},\perp}}{\partial s}\right]\\
&=Q_{\mathrm{e},\perp}-\frac{n\left(T_{\mathrm{e},\perp}-T_{\mathrm{e},//}\right)}{\tau_{\mathrm{rlx}}}+\frac{2m_{\mathrm{e}}}{m_{\mathrm{i}}}\frac{n\left(T_{\mathrm{i}}-T_{\mathrm{e},\perp}\right)}{\tau_{\mathrm{e}}}.
\end{aligned}
\tag{A.25}
$$

Here, it should be noted that the summation of the equations of parallel and perpendicular ion energy transport, Eqs. (A.18) and (A.24), in the condition of isotropic ion temperature accords with the Braginskii's equation of ion energy

transport [37];

$$\begin{aligned}&\frac{\partial}{\partial t}\left(\frac{1}{2}m_{\mathrm{i}}nV^2+\frac{3}{2}nT_{\mathrm{i}}\right)+\frac{\partial}{\partial s}\left(\frac{1}{2}m_{\mathrm{i}}nV^3+\frac{5}{2}nT_{\mathrm{i}}V\right)+\frac{\partial}{\partial s}\left(-\kappa_{\mathrm{i}}^{\mathrm{SH}}\frac{\partial T_{\mathrm{i}}}{\partial s}\right)\\&=Q_{\mathrm{i}}-\frac{\partial}{\partial s}\left(-\eta_{\mathrm{i}}\frac{\partial V}{\partial s}\right)V+\frac{3m_{\mathrm{e}}}{m_{\mathrm{i}}}\frac{n\left(T_{\mathrm{e}}-T_{\mathrm{i}}\right)}{\tau_{\mathrm{e}}}-V\frac{\partial}{\partial s}\left(nT_{\mathrm{e}}\right).\end{aligned} \tag{A.26}$$

*Equation of electron energy transport*

Equation of electron energy transport is obtained by the summation of Eqs. (A.19) and (A.25) and assuming that electron temperature is isotropic as follows;

$$\begin{aligned}&\frac{\partial}{\partial t}\left(\frac{3}{2}nT_{\mathrm{e}}\right)+\frac{\partial}{\partial s}\left(\frac{5}{2}nT_{\mathrm{e}}V\right)+\frac{\partial}{\partial s}\left(-\kappa_{\mathrm{e}}^{\mathrm{SH}}\frac{\partial T_{\mathrm{e}}}{\partial s}\right)\\&=Q_{\mathrm{e}}-\frac{3m_{\mathrm{e}}}{m_{\mathrm{i}}}\frac{n\left(T_{\mathrm{e}}-T_{\mathrm{i}}\right)}{\tau_{\mathrm{e}}}+V\frac{\partial}{\partial s}\left(nT_{\mathrm{e}}\right).\end{aligned} \tag{A.27}$$

## A.2 Necessity of the artificial viscosity term

The equation of continuity and the parallel momentum transport in VD region in the steady state without the artificial viscosity term become as follows;

$$\frac{\mathrm{d}}{\mathrm{d}s}\left(nV\right)=-\frac{n}{\tau^{\mathrm{VD}}}, \tag{A.28}$$

$$\frac{\mathrm{d}}{\mathrm{d}s}\left(m_{\mathrm{i}}nV^2+nT_{\mathrm{i},//}+nT_{\mathrm{e}}\right)=-\frac{m_{\mathrm{i}}nV}{\tau^{\mathrm{VD}}}. \tag{A.29}$$

By combining these equations, following equation can be obtained;

$$\left(V^2-c_{\mathrm{s}}^2\right)\frac{\mathrm{d}V}{\mathrm{d}s}=\frac{c_{\mathrm{s}}^2}{\tau^{\mathrm{VD}}}-V\frac{\mathrm{d}}{\mathrm{d}s}\left(c_{\mathrm{s}}^2\right). \tag{A.30}$$

If the Bohm criterion is satisfied, $V^2 - c_{\mathrm{s}}^2$ in the left hand side of Eq. (A.30) becomes positive in the VD region. Because the right hand side of Eq. (A.30) is always positive, it leads that d$V$/d$s$ is also positive in the VD region. This means that the flow velocity $V$ cannot be continuous when it changes sign in the VD region. By introducing the artificial viscosity term in the momentum sink as shown in Eq. (2.40), the flow velocity can be continuous in the VD region and a periodic boundary condition becomes available. The artificial momentum diffusivity $D_{\mathrm{m}}^{\mathrm{VD}}$ has non-zero values at positions far enough from the sheath entrance, so that Eq.

(2.4) keeps its nature as the first-order differential equation in the plasma region.

## A.3 Numerical calculation method

All of the fluid equations are discretized individually on the homogeneous staggered grid shown in Fig. 37. The grid number and time step are denoted by *i* and *j*, respectively. For the discretization of inertia terms, the full implicit scheme is used. The convection terms and diffusion terms are discretized by the first-order accurate upwind scheme and the second-order accurate central-difference scheme. In this section, the effects of atomic processes and plasma radial diffusion are included in the source terms in the right hand side.

*Equation of continuity for ion*

The equation of continuity for ion, Eq. (2.3), is discretized as follows;

$$\left(n_i^{j+1}-n_i^{j}\right)\frac{\Delta s}{\Delta t}+\left(nV\right)_{i+1/2}^{j+1}-\left(nV\right)_{i-1/2}^{j+1}+n_i^{j+1}\frac{\Delta s}{\tau^{\mathrm{VD}}}=S_i^{j+1}\Delta s, \tag{A.31}$$

$$\left(nV\right)_{i+1/2}^{j+1}=\begin{cases} n_i^{j+1}\left[V_i^{j+1},0\right]-n_{i+1}^{j+1}\left[-V_i^{j+1},0\right] & \left(1\le i\le N-1\right) \\ n_N^{j+1}\left[V_N^{j+1},0\right]-n_1^{j+1}\left[-V_N^{j+1},0\right] & \left(i=N\right) \end{cases}, \tag{A.32}$$

$$\left(nV\right)_{i-1/2}^{j+1}=\begin{cases} n_N^{j+1}\left[V_N^{j+1},0\right]-n_i^{j+1}\left[-V_N^{j+1},0\right] & \left(i=1\right) \\ n_{i-1}^{j+1}\left[V_{i-1}^{j+1},0\right]-n_i^{j+1}\left[-V_{i-1}^{j+1},0\right] & \left(2\le i\le N\right) \end{cases}, \tag{A.33}$$

Here, the bracket [ ] represents a function which returns the maximum value among the arguments. Equation (A.31) is rewritten in the form of Eq. (2.51) as follows;

$$a_i n_i^{j+1}=\begin{cases} b_1 n_2^{j+1}+c_1 n_N^{j+1}+d_1 & \left(i=1\right) \\ b_i n_{i+1}^{j+1}+c_i n_{i-1}^{j+1}+d_i & \left(2\le i\le N-1\right) \\ b_N n_1^{j+1}+c_N n_{N-1}^{j+1}+d_N & \left(i=N\right) \end{cases}, \tag{A.34}$$

$$a_i=\begin{cases} \dfrac{\Delta s}{\Delta t}+\dfrac{\Delta s}{\tau^{\mathrm{VD}}}+\left[V_1^{j+1},0\right]+\left[-V_N^{j+1},0\right] & \left(i=1\right) \\ \dfrac{\Delta s}{\Delta t}+\dfrac{\Delta s}{\tau^{\mathrm{VD}}}+\left[V_i^{j+1},0\right]+\left[-V_{i-1}^{j+1},0\right] & \left(2\le i\le N\right) \end{cases}, \tag{A.35}$$

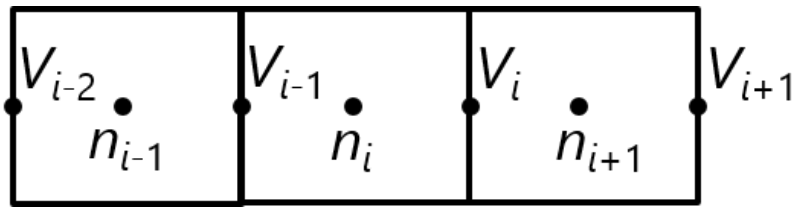


Figure 37 Staggered grid. The grid number is denoted by $i$. The range is $1 \le i \le N$.

$$b_i = \left[-V_i^{j+1}, 0\right], \tag{A.36}$$

$$c_i = \begin{cases} \left[V_N^{j+1}, 0\right], & (i=1) \\ \left[V_{i-1}^{j+1}, 0\right], & (2 \le i \le N) \end{cases} \tag{A.37}$$

$$d_i = n_i^j \frac{\Delta s}{\Delta t} + S_i^{j+1} \Delta s. \tag{A.38}$$

*Equation of parallel momentum transport*

The equation of parallel momentum transport, Eq. (2.4), is discretized as follows;

$$\begin{aligned} &\left( \left(m_\mathrm{i} n V\right)_i^{j+1} - \left(m_\mathrm{i} n V\right)_i^j \right) \frac{\Delta s}{\Delta t} + \left(m_\mathrm{i} n V^2\right)_{i+1/2}^{j+1} - \left(m_\mathrm{i} n V^2\right)_{i-1/2}^{j+1} \\ &+ \left( - m_\mathrm{i} n D_\mathrm{m}^{\mathrm{VD}} \frac{\partial V}{\partial s} \right)_{i+1/2}^{j+1} - \left( - m_\mathrm{i} n D_\mathrm{m}^{\mathrm{VD}} \frac{\partial V}{\partial s} \right)_{i-1/2}^{j+1} + \left(m_\mathrm{i} n V\right)_i^{j+1} \frac{\Delta s}{\tau^{\mathrm{VD}}} \\ &= M_{\mathrm{m},i}^{j+1} \Delta s - n_{i+1}^{j+1} \left( T_{\mathrm{i},//,i+1}^{j+1} + T_{\mathrm{e},i+1}^{j+1} \right) + n_i^{j+1} \left( T_{\mathrm{i},//,i}^{j+1} + T_{\mathrm{e},i}^{j+1} \right), \end{aligned} \tag{A.39}$$

$$\left(m_\mathrm{i} n V\right)_i = \begin{cases} m_\mathrm{i} \dfrac{n_i + n_{i+1}}{2} V_i, & (1 \le i \le N-1) \\ m_\mathrm{i} \dfrac{n_N + n_1}{2} V_N, & (i = N) \end{cases} \tag{A.40}$$

$$\left(m_{\mathrm{i}} n V^2\right)_{i+1/2}^{j+1} = \begin{cases} m_{\mathrm{i}} n_{i+1}^{j+1} \left[ \dfrac{V_i^{j+1} + V_{i+1}^{j+1}}{2}, 0 \right] V_i^{j+1} \\ - m_{\mathrm{i}} n_{i+1}^{j+1} \left[ - \dfrac{V_i^{j+1} + V_{i+1}^{j+1}}{2}, 0 \right] V_{i+1}^{j+1}, \\ m_{\mathrm{i}} n_1^{j+1} \left[ \dfrac{V_N^{j+1} + V_1^{j+1}}{2}, 0 \right] V_N^{j+1} \\ - m_{\mathrm{i}} n_1^{j+1} \left[ - \dfrac{V_N^{j+1} + V_1^{j+1}}{2}, 0 \right] V_1^{j+1}, \end{cases} \quad \begin{matrix} (1 \le i \le N-1) \\ (i = N) \end{matrix} \tag{A.41}$$

$$\left(m_{\mathrm{i}} n V^2\right)_{i-1/2}^{j+1} = \begin{cases} m_{\mathrm{i}} n_1^{j+1} \left[ \dfrac{V_N^{j+1} + V_1^{j+1}}{2}, 0 \right] V_N^{j+1} \\ - m_{\mathrm{i}} n_1^{j+1} \left[ - \dfrac{V_N^{j+1} + V_1^{j+1}}{2}, 0 \right] V_1^{j+1}, \\ m_{\mathrm{i}} n_i^{j+1} \left[ \dfrac{V_{i-1}^{j+1} + V_i^{j+1}}{2}, 0 \right] V_{i-1}^{j+1} \\ - m_{\mathrm{i}} n_i^{j+1} \left[ - \dfrac{V_{i-1}^{j+1} + V_i^{j+1}}{2}, 0 \right] V_i^{j+1}, \end{cases} \quad \begin{matrix} (i = 1) \\ (2 \le i \le N) \end{matrix} \tag{A.42}$$

$$\left( - m_{\mathrm{i}} n D_{\mathrm{m}}^{\mathrm{VD}} \frac{\partial V}{\partial s} \right)_{i+1/2}^{j+1} = \begin{cases} - m_{\mathrm{i}} n_{i+1}^{j+1} D_{\mathrm{m},i+1}^{\mathrm{VD}} \dfrac{V_{i+1}^{j+1} - V_i^{j+1}}{\Delta s}, & (1 \le i \le N-1) \\ - m_{\mathrm{i}} n_1^{j+1} D_{\mathrm{m},1}^{\mathrm{VD}} \dfrac{V_1^{j+1} - V_N^{j+1}}{\Delta s}, & (i = N) \end{cases} \tag{A.43}$$

$$\left( - m_{\mathrm{i}} n D_{\mathrm{m}}^{\mathrm{VD}} \frac{\partial V}{\partial s} \right)_{i-1/2}^{j+1} = \begin{cases} - m_{\mathrm{i}} n_1^{j+1} D_{\mathrm{m},1}^{\mathrm{VD}} \dfrac{V_1^{j+1} - V_N^{j+1}}{\Delta s}, & (i = 1) \\ - m_{\mathrm{i}} n_i^{j+1} D_{\mathrm{m},i}^{\mathrm{VD}} \dfrac{V_i^{j+1} - V_{i-1}^{j+1}}{\Delta s}. & (2 \le i \le N) \end{cases} \tag{A.44}$$

Equation (A.39) is rewritten in the form of Eq. (2.51) as follows;

$$a_i V_i^{j+1} = \begin{cases} b_1 V_2^{j+1} + c_1 V_N^{j+1} + d_1, & (i = 1) \\ b_i V_{i+1}^{j+1} + c_i V_{i-1}^{j+1} + d_i, & (2 \le i \le N-1) \\ b_N V_1^{j+1} + c_N V_{N-1}^{j+1} + d_N, & (i = N) \end{cases} \tag{A.45}$$

$$
a_i = \begin{cases}
m_{\mathrm{i}} \dfrac{n_1^{j+1} + n_2^{j+1}}{2} \dfrac{\Delta s}{\Delta t} + m_{\mathrm{i}} \dfrac{n_1^{j+1} + n_2^{j+1}}{2} \dfrac{\Delta s}{\tau^{\mathrm{VD}}} \\
+ m_{\mathrm{i}} n_2^{j+1} \left[ \dfrac{V_1^{j+1} + V_2^{j+1}}{2}, 0 \right] \\
+ m_{\mathrm{i}} n_1^{j+1} \left[ - \dfrac{V_N^{j+1} + V_1^{j+1}}{2}, 0 \right] \\
+ m_{\mathrm{i}} n_2^{j+1} \dfrac{D_{\mathrm{m},2}^{\mathrm{VD}}}{\Delta s} + m_{\mathrm{i}} n_1^{j+1} \dfrac{D_{\mathrm{m},1}^{\mathrm{VD}}}{\Delta s}, \\
m_{\mathrm{i}} \dfrac{n_i^{j+1} + n_{i+1}^{j+1}}{2} \dfrac{\Delta s}{\Delta t} + m_{\mathrm{i}} \dfrac{n_i^{j+1} + n_{i+1}^{j+1}}{2} \dfrac{\Delta s}{\tau^{\mathrm{VD}}} \\
+ m_{\mathrm{i}} n_{i+1}^{j+1} \left[ \dfrac{V_i^{j+1} + V_{i+1}^{j+1}}{2}, 0 \right] \\
+ m_{\mathrm{i}} n_i^{j+1} \left[ - \dfrac{V_{i-1}^{j+1} + V_i^{j+1}}{2}, 0 \right] \\
+ m_{\mathrm{i}} n_{i+1}^{j+1} \dfrac{D_{\mathrm{m},i+1}^{\mathrm{VD}}}{\Delta s} + m_{\mathrm{i}} n_i^{j+1} \dfrac{D_{\mathrm{m},i}^{\mathrm{VD}}}{\Delta s}, \\
m_{\mathrm{i}} \dfrac{n_N^{j+1} + n_1^{j+1}}{2} \dfrac{\Delta s}{\Delta t} + m_{\mathrm{i}} \dfrac{n_N^{j+1} + n_1^{j+1}}{2} \dfrac{\Delta s}{\tau^{\mathrm{VD}}} \\
+ m_{\mathrm{i}} n_1^{j+1} \left[ \dfrac{V_N^{j+1} + V_1^{j+1}}{2}, 0 \right] \\
+ m_{\mathrm{i}} n_N^{j+1} \left[ - \dfrac{V_{N-1}^{j+1} + V_N^{j+1}}{2}, 0 \right] \\
+ m_{\mathrm{i}} n_1^{j+1} \dfrac{D_{\mathrm{m},1}^{\mathrm{VD}}}{\Delta s} + m_{\mathrm{i}} n_N^{j+1} \dfrac{D_{\mathrm{m},N}^{\mathrm{VD}}}{\Delta s},
\end{cases}
\begin{array}{l}
(i = 1) \\
(2 \le i \le N-1) \\
(i = N)
\end{array}
\tag{A.46}
$$

$$
b_i = \begin{cases}
m_{\mathrm{i}} n_{i+1}^{j+1} \left[ - \dfrac{V_i^{j+1} + V_{i+1}^{j+1}}{2}, 0 \right] + m_{\mathrm{i}} n_{i+1}^{j+1} \dfrac{D_{\mathrm{m},i+1}^{\mathrm{VD}}}{\Delta s}, \\
m_{\mathrm{i}} n_1^{j+1} \left[ - \dfrac{V_N^{j+1} + V_1^{j+1}}{2}, 0 \right] + m_{\mathrm{i}} n_1^{j+1} \dfrac{D_{\mathrm{m},1}^{\mathrm{VD}}}{\Delta s},
\end{cases}
\begin{array}{l}
(1 \le i \le N-1) \\
(i = N)
\end{array}
\tag{A.47}
$$

$$
c_i = \begin{cases}
m_{\mathrm{i}} n_1^{j+1} \left[ \dfrac{V_N^{j+1} + V_1^{j+1}}{2}, 0 \right] + m_{\mathrm{i}} n_1^{j+1} \dfrac{D_{\mathrm{m},1}^{\mathrm{VD}}}{\Delta s}, \\
m_{\mathrm{i}} n_i^{j+1} \left[ \dfrac{V_{i-1}^{j+1} + V_i^{j+1}}{2}, 0 \right] + m_{\mathrm{i}} n_i^{j+1} \dfrac{D_{\mathrm{m},i}^{\mathrm{VD}}}{\Delta s},
\end{cases}
\begin{array}{l}
(i = 1) \\
(2 \le i \le N)
\end{array}
\tag{A.48}
$$

$$d_i = \begin{cases} m_{\mathrm{i}} \dfrac{n_i^j + n_{i+1}^j}{2} V_i^{\,j} \dfrac{\Delta s}{\Delta t} + M_{\mathrm{m},i}^{\,j+1} \Delta s \\ - n_{i+1}^{j+1} \left( T_{\mathrm{i},//,i+1}^{\,j+1} + T_{\mathrm{e},i+1}^{\,j+1} \right) + n_i^{j+1} \left( T_{\mathrm{i},//,i}^{\,j+1} + T_{\mathrm{e},i}^{\,j+1} \right), & (1 \le i \le N-1) \\ m_{\mathrm{i}} \dfrac{n_N^j + n_1^j}{2} V_N^j \dfrac{\Delta s}{\Delta t} + M_{\mathrm{m},N}^{\,j+1} \Delta s & (i = N) \\ - n_1^{j+1} \left( T_{\mathrm{i},//,1}^{\,j+1} + T_{\mathrm{e},1}^{\,j+1} \right) + n_N^{j+1} \left( T_{\mathrm{i},//,N}^{\,j+1} + T_{\mathrm{e},N}^{\,j+1} \right) \end{cases} \tag{A.49}$$

*Equation of parallel ion energy transport*

The equation of parallel ion energy transport, Eq. (2.5), is discretized as follows;

$$\begin{aligned} & \left( \left( \frac{1}{2} m_{\mathrm{i}} n V^2 + \frac{1}{2} n T_{\mathrm{i},//} \right)_i^{j+1} - \left( \frac{1}{2} m_{\mathrm{i}} n V^2 + \frac{1}{2} n T_{\mathrm{i},//} \right)_i^{j} \right) \frac{\Delta s}{\Delta t} \\ & + \left( \frac{1}{2} m_{\mathrm{i}} n V^3 + \frac{3}{2} n T_{\mathrm{i},//} V \right)_{i+1/2}^{j+1} - \left( \frac{1}{2} m_{\mathrm{i}} n V^3 + \frac{3}{2} n T_{\mathrm{i},//} V \right)_{i-1/2}^{j+1} \\ & + \left( - \kappa_{\mathrm{i},//}^{\mathrm{eff}} \frac{\partial T_{\mathrm{i},//}}{\partial s} \right)_{i+1/2}^{j+1} - \left( - \kappa_{\mathrm{i},//}^{\mathrm{eff}} \frac{\partial T_{\mathrm{i},//}}{\partial s} \right)_{i-1/2}^{j+1} \\ & + \frac{g_{\mathrm{i},//}^{\mathrm{VD}}}{2} n_i^{j+1} T_{\mathrm{i},//,i}^{\,j+1} \frac{\Delta s}{\tau^{\mathrm{VD}}} + n_i^{j+1} T_{\mathrm{i},//,i}^{\,j+1} \frac{\Delta s}{\tau_{\mathrm{rlx},i}^{\,j+1}} + \frac{m_{\mathrm{e}}}{m_{\mathrm{i}}} n_i^{j+1} T_{\mathrm{i},//,i}^{\,j+1} \frac{\Delta s}{\tau_{\mathrm{e},i}^{\,j+1}} \\ & = Q_{\mathrm{i},//,i}^{\,j+1} \Delta s - \left( \frac{1}{2} m_{\mathrm{i}} n V^2 \right)_i^{j+1} \frac{\Delta s}{\tau^{\mathrm{VD}}} + n_i^{j+1} T_{\mathrm{i},\perp,i}^{\,j+1} \frac{\Delta s}{\tau_{\mathrm{rlx},i}^{\,j+1}} + \frac{m_e}{m_i} n_i^{j+1} T_{\mathrm{e},i}^{\,j+1} \frac{\Delta s}{\tau_{\mathrm{e},i}^{\,j+1}} \\ & - \frac{1}{2} V_{i-1}^{\,j+1} \left( n_i^{j+1} T_{\mathrm{e},i}^{\,j+1} - n_{i-1}^{j+1} T_{\mathrm{e},i-1}^{\,j+1} \right) - \frac{1}{2} V_i^{\,j+1} \left( n_{i+1}^{j+1} T_{\mathrm{e},i+1}^{\,j+1} - n_i^{j+1} T_{\mathrm{e},i}^{\,j+1} \right), \end{aligned} \tag{A.50}$$

$$\left( \frac{1}{2} m_{\mathrm{i}} n V^2 \right)_i = \frac{1}{2} m_{\mathrm{i}} n_i \left( \frac{V_{i-1} + V_i}{2} \right)^2, \tag{A.51}$$

$$\left(\frac{1}{2}m_{\mathrm{i}}nV^3+\frac{3}{2}nT_{\mathrm{i},//}V\right)_{i+1/2}^{j+1}$$
$$=\begin{cases}\left(\frac{1}{2}m_{\mathrm{i}}n_i^{j+1}\left(V_i^{j+1}\right)^2+\frac{3}{2}n_i^{j+1}T_{\mathrm{i},//,i}^{j+1}\right)\left[V_i^{j+1},0\right] & \\ -\left(\frac{1}{2}m_{\mathrm{i}}n_{i+1}^{j+1}\left(V_i^{j+1}\right)^2+\frac{3}{2}n_{i+1}^{j+1}T_{\mathrm{i},//,i+1}^{j+1}\right)\left[-V_i^{j+1},0\right], & \left(1\le i\le N-1\right) \\ \left(\frac{1}{2}m_{\mathrm{i}}n_N^{j+1}\left(V_N^{j+1}\right)^2+\frac{3}{2}n_N^{j+1}T_{\mathrm{i},//,N}^{j+1}\right)\left[V_N^{j+1},0\right] & \left(i=N\right) \\ -\left(\frac{1}{2}m_{\mathrm{i}}n_1^{j+1}\left(V_N^{j+1}\right)^2+\frac{3}{2}n_1^{j+1}T_{\mathrm{i},//,1}^{j+1}\right)\left[-V_N^{j+1},0\right], & \end{cases} \quad \text{(A.52)}$$

$$\left(\frac{1}{2}m_{\mathrm{i}}nV^3+\frac{3}{2}nT_{\mathrm{i},//}V\right)_{i-1/2}^{j+1}$$
$$=\begin{cases}\left(\frac{1}{2}m_{\mathrm{i}}n_N^{j+1}\left(V_N^{j+1}\right)^2+\frac{3}{2}n_N^{j+1}T_{\mathrm{i},//,N}^{j+1}\right)\left[V_N^{j+1},0\right] & \\ -\left(\frac{1}{2}m_{\mathrm{i}}n_1^{j+1}\left(V_N^{j+1}\right)^2+\frac{3}{2}n_1^{j+1}T_{\mathrm{i},//,1}^{j+1}\right)\left[-V_N^{j+1},0\right], & \left(i=1\right) \\ \left(\frac{1}{2}m_{\mathrm{i}}n_{i-1}^{j+1}\left(V_{i-1}^{j+1}\right)^2+\frac{3}{2}n_{i-1}^{j+1}T_{\mathrm{i},//,i-1}^{j+1}\right)\left[V_{i-1}^{j+1},0\right] & \left(2\le i\le N\right) \\ -\left(\frac{1}{2}m_{\mathrm{i}}n_i^{j+1}\left(V_{i-1}^{j+1}\right)^2+\frac{3}{2}n_i^{j+1}T_{\mathrm{i},//,i}^{j+1}\right)\left[-V_{i-1}^{j+1},0\right], & \end{cases} \quad \text{(A.53)}$$

$$\left(-\kappa_{\mathrm{i},//}^{\mathrm{eff}}\frac{\partial T_{\mathrm{i},//}}{\partial s}\right)_{i+1/2}^{j+1}=\begin{cases}-\kappa_{\mathrm{i},//,i+1/2}^{\mathrm{eff},j+1}\dfrac{T_{\mathrm{i},//,i+1}^{j+1}-T_{\mathrm{i},//,i}^{j+1}}{\Delta s}, & \left(1\le i\le N-1\right) \\ -\kappa_{\mathrm{i},//,N+1/2}^{\mathrm{eff},j+1}\dfrac{T_{\mathrm{i},//,1}^{j+1}-T_{\mathrm{i},//,N}^{j+1}}{\Delta s}, & \left(i=N\right)\end{cases} \quad \text{(A.54)}$$

$$\left(-\kappa_{\mathrm{i},//}^{\mathrm{eff}}\frac{\partial T_{\mathrm{i},//}}{\partial s}\right)_{i-1/2}^{j+1}=\begin{cases}-\kappa_{\mathrm{i},//,1/2}^{\mathrm{eff},j+1}\dfrac{T_{\mathrm{i},//,1}^{j+1}-T_{\mathrm{i},//,N}^{j+1}}{\Delta s}, & \left(i=1\right) \\ -\kappa_{\mathrm{i},//,i-1/2}^{\mathrm{eff},j+1}\dfrac{T_{\mathrm{i},//,i}^{j+1}-T_{\mathrm{i},//,i-1}^{j+1}}{\Delta s}. & \left(2\le i\le N\right)\end{cases} \quad \text{(A.55)}$$

Here, the heat conductivities at the boundaries of the cells are estimated by the harmonic average of those at the adjacent grids as follows;

$$\kappa_{\mathrm{i},//,i+1/2}^{\mathrm{eff}} = \begin{cases} \dfrac{2\kappa_{\mathrm{i},//,i}^{\mathrm{eff}}\kappa_{\mathrm{i},//,i+1}^{\mathrm{eff}}}{\kappa_{\mathrm{i},//,i}^{\mathrm{eff}} + \kappa_{\mathrm{i},//,i+1}^{\mathrm{eff}}}, & (1 \le i \le N-1) \\ \dfrac{2\kappa_{\mathrm{i},//,N}^{\mathrm{eff}}\kappa_{\mathrm{i},//,1}^{\mathrm{eff}}}{\kappa_{\mathrm{i},//,N}^{\mathrm{eff}} + \kappa_{\mathrm{i},//,1}^{\mathrm{eff}}}. & (i = N) \end{cases} \quad \text{(A.56)}$$

Equation (A.50) is rewritten in the form of Eq. (2.51) as follows;

$$a_i T_{\mathrm{i},//,i}^{j+1} = \begin{cases} b_1 T_{\mathrm{i},//,2}^{j+1} + c_1 T_{\mathrm{i},//,N}^{j+1} + d_1, & (i = 1) \\ b_i T_{\mathrm{i},//,i+1}^{j+1} + c_i T_{\mathrm{i},//,i-1}^{j+1} + d_i, & (2 \le i \le N-1) \\ b_N T_{\mathrm{i},//,1}^{j+1} + c_N T_{\mathrm{i},//,N-1}^{j+1} + d_N, & (i = N) \end{cases} \quad \text{(A.57)}$$

$$a_i = \begin{cases} n_1^{j+1}\left( \dfrac{\Delta s}{2\Delta t} + \dfrac{g_{\mathrm{i},//}^{\mathrm{VD}}\Delta s}{2\tau^{\mathrm{VD}}} + \dfrac{\Delta s}{\tau_{\mathrm{rlx},1}^{j+1}} + \dfrac{m_{\mathrm{e}}}{m_{\mathrm{i}}}\dfrac{\Delta s}{\tau_{\mathrm{e},1}^{j+1}} \right) \\ + \dfrac{3}{2} n_1^{j+1}\left( \left[ V_1^{j+1}, 0 \right] + \left[ -V_N^{j+1}, 0 \right] \right) \\ + \dfrac{\kappa_{\mathrm{i},//,3/2}^{\mathrm{eff},j+1} + \kappa_{\mathrm{i},//,1/2}^{\mathrm{eff},j+1}}{\Delta \mathrm{s}}, & (i = 1) \\ n_i^{j+1}\left( \dfrac{\Delta s}{2\Delta t} + \dfrac{g_{\mathrm{i},//}^{\mathrm{VD}}\Delta s}{2\tau^{\mathrm{VD}}} + \dfrac{\Delta s}{\tau_{\mathrm{rlx},i}^{j+1}} + \dfrac{m_{\mathrm{e}}}{m_{\mathrm{i}}}\dfrac{\Delta s}{\tau_{\mathrm{e},i}^{j+1}} \right) \\ + \dfrac{3}{2} n_i^{j+1}\left( \left[ V_i^{j+1}, 0 \right] + \left[ -V_{i-1}^{j+1}, 0 \right] \right) \\ + \dfrac{\kappa_{\mathrm{i},//,i+1/2}^{\mathrm{eff},j+1} + \kappa_{\mathrm{i},//,i-1/2}^{\mathrm{eff},j+1}}{\Delta \mathrm{s}}, & (2 \le i \le N) \end{cases} \quad \text{(A.58)}$$

$$b_i = \begin{cases} \dfrac{3}{2} n_{i+1}^{j+1}\left[ -V_i^{j+1}, 0 \right] + \dfrac{\kappa_{\mathrm{i},//,i+1/2}^{\mathrm{eff},j+1}}{\Delta s}, & (1 \le i \le N-1) \\ \dfrac{3}{2} n_1^{j+1}\left[ -V_N^{j+1}, 0 \right] + \dfrac{\kappa_{\mathrm{i},//,N+1/2}^{\mathrm{eff},j+1}}{\Delta s}, & (i = N) \end{cases} \quad \text{(A.59)}$$

$$c_i = \begin{cases} \dfrac{3}{2} n_N^{j+1}\left[ V_N^{j+1}, 0 \right] + \dfrac{\kappa_{\mathrm{i},//,1/2}^{\mathrm{eff},j+1}}{\Delta s}, & (i = 1) \\ \dfrac{3}{2} n_{i-1}^{j+1}\left[ V_{i-1}^{j+1}, 0 \right] + \dfrac{\kappa_{\mathrm{i},//,i-1/2}^{\mathrm{eff},j+1}}{\Delta s}, & (2 \le i \le N) \end{cases} \quad \text{(A.60)}$$

$$
d_i = \begin{cases}
-\frac{1}{2} m_{\mathrm{i}} n_1^{j+1} \left( \frac{V_N^{j+1} + V_1^{j+1}}{2} \right)^2 \left( \frac{\Delta s}{\Delta t} + \frac{\Delta s}{\tau^{\mathrm{VD}}} \right) \\
+ \left( \frac{1}{2} m_{\mathrm{i}} n_1^{j} \left( \frac{V_N^{j} + V_1^{j}}{2} \right)^2 + \frac{1}{2} n_1^{j} T_{\mathrm{i},//,1}^{j} \right) \frac{\Delta s}{\Delta t} \\
-\frac{1}{2} m_{\mathrm{i}} \left( V_1^{j+1} \right)^2 \left( n_1^{j+1} \left[ V_1^{j+1}, 0 \right] - n_2^{j+1} \left[ -V_1^{j+1}, 0 \right] \right) \\
+\frac{1}{2} m_{\mathrm{i}} \left( V_N^{j+1} \right)^2 \left( n_N^{j+1} \left[ V_N^{j+1}, 0 \right] - n_1^{j+1} \left[ -V_N^{j+1}, 0 \right] \right) \\
+ Q_{\mathrm{i},//,1}^{j+1} \Delta s + n_1^{j+1} T_{\mathrm{i},\perp,1}^{j+1} \frac{\Delta s}{\tau_{\mathrm{rlx},1}^{j+1}} + n_1^{j+1} T_{\mathrm{e},1}^{j+1} \frac{m_{\mathrm{e}}}{m_{\mathrm{i}}} \frac{\Delta s}{\tau_{\mathrm{e},1}^{j+1}} \\
-\frac{1}{2} V_N^{j+1} \left( n_1^{j+1} T_{\mathrm{e},1}^{j+1} - n_N^{j+1} T_{\mathrm{e},1}^{j+1} \right) \\
-\frac{1}{2} V_1^{j+1} \left( n_2^{j+1} T_{\mathrm{e},2}^{j+1} - n_1^{j+1} T_{\mathrm{e},1}^{j+1} \right), & (i = 1) \\
-\frac{1}{2} m_{\mathrm{i}} n_i^{j+1} \left( \frac{V_{i-1}^{j+1} + V_i^{j+1}}{2} \right)^2 \left( \frac{\Delta s}{\Delta t} + \frac{\Delta s}{\tau^{\mathrm{VD}}} \right) & (2 \le i \le N-1) \\
+ \left( \frac{1}{2} m_{\mathrm{i}} n_i^{j} \left( \frac{V_{i-1}^{j} + V_i^{j}}{2} \right)^2 + \frac{1}{2} n_i^{j} T_{\mathrm{i},//,i}^{j} \right) \frac{\Delta s}{\Delta t} \\
-\frac{1}{2} m_{\mathrm{i}} \left( V_i^{j+1} \right)^2 \left( n_i^{j+1} \left[ V_i^{j+1}, 0 \right] - n_{i+1}^{j+1} \left[ -V_i^{j+1}, 0 \right] \right) \\
+\frac{1}{2} m_{\mathrm{i}} \left( V_{i-1}^{j+1} \right)^2 \left( n_{i-1}^{j+1} \left[ V_{i-1}^{j+1}, 0 \right] - n_i^{j+1} \left[ -V_{i-1}^{j+1}, 0 \right] \right) \\
+ Q_{\mathrm{i},//,i}^{j+1} \Delta s + n_i^{j+1} T_{\mathrm{i},\perp,i}^{j+1} \frac{\Delta s}{\tau_{\mathrm{rlx},i}^{j+1}} + n_i^{j+1} T_{\mathrm{e},i}^{j+1} \frac{m_{\mathrm{e}}}{m_{\mathrm{i}}} \frac{\Delta s}{\tau_{\mathrm{e},i}^{j+1}} \\
-\frac{1}{2} V_{i-1}^{j+1} \left( n_i^{j+1} T_{\mathrm{e},i}^{j+1} - n_{i-1}^{j+1} T_{\mathrm{e},i-1}^{j+1} \right) \\
-\frac{1}{2} V_i^{j+1} \left( n_{i+1}^{j+1} T_{\mathrm{e},i+1}^{j+1} - n_i^{j+1} T_{\mathrm{e},i}^{j+1} \right),
\end{cases}
\tag{A.61}
$$

$$
d_i = \begin{cases}
-\frac{1}{2} m_{\mathrm{i}} n_N^{j+1} \left( \frac{V_{N-1}^{j+1} + V_N^{j+1}}{2} \right)^2 \left( \frac{\Delta s}{\Delta t} + \frac{\Delta s}{\tau^{\mathrm{VD}}} \right) \\
+ \left( \frac{1}{2} m_{\mathrm{i}} n_N^{j} \left( \frac{V_{N-1}^{j} + V_N^{j}}{2} \right)^2 + \frac{1}{2} n_N^{j} T_{\mathrm{i},//,N}^{j} \right) \frac{\Delta s}{\Delta t} \\
-\frac{1}{2} m_{\mathrm{i}} \left( V_N^{j+1} \right)^2 \left( n_N^{j+1} \left[ V_N^{j+1}, 0 \right] - n_1^{j+1} \left[ -V_N^{j+1}, 0 \right] \right) \\
+\frac{1}{2} m_{\mathrm{i}} \left( V_{N-1}^{j+1} \right)^2 \left( n_{N-1}^{j+1} \left[ V_{N-1}^{j+1}, 0 \right] - n_N^{j+1} \left[ -V_{N-1}^{j+1}, 0 \right] \right) \\
+ Q_{\mathrm{i},//,N}^{j+1} \Delta s + n_N^{j+1} T_{\mathrm{i},\perp,N}^{j+1} \frac{\Delta s}{\tau_{\mathrm{rlx},N}^{j+1}} \\
+ n_N^{j+1} T_{\mathrm{e},N}^{j+1} \frac{m_{\mathrm{e}}}{m_{\mathrm{i}}} \frac{\Delta s}{\tau_{\mathrm{e},N}^{j+1}} \\
-\frac{1}{2} V_{N-1}^{j+1} \left( n_N^{j+1} T_{\mathrm{e},N}^{j+1} - n_{N-1}^{j+1} T_{\mathrm{e},N-1}^{j+1} \right) \\
-\frac{1}{2} V_N^{j+1} \left( n_1^{j+1} T_{\mathrm{e},1}^{j+1} - n_i^{j+1} T_{\mathrm{e},N}^{j+1} \right).
\end{cases} \qquad (i = N)
$$

*Equation of perpendicular ion energy transport*

The equation of perpendicular ion energy transport, Eq. (2.6), is discretized as follows;

$$
\begin{aligned}
&\left( n_i^{j+1} T_{\mathrm{i},\perp,i}^{j+1} - n_i^{j} T_{\mathrm{i},\perp,i}^{j} \right) \frac{\Delta s}{\Delta t} + \left( n T_{\mathrm{i},\perp} V \right)_{i+1/2}^{j+1} - \left( n T_{\mathrm{i},\perp} V \right)_{i-1/2}^{j+1} \\
&+ \left( -\kappa_{\mathrm{i},\perp}^{\mathrm{eff}} \frac{\partial T_{\mathrm{i},\perp}}{\partial s} \right)_{i+1/2}^{j+1} - \left( -\kappa_{\mathrm{i},\perp}^{\mathrm{eff}} \frac{\partial T_{\mathrm{i},\perp}}{\partial s} \right)_{i-1/2}^{j+1} \\
&+ g_{\mathrm{i},\perp}^{\mathrm{VD}} n_i^{j+1} T_{\mathrm{i},\perp,i}^{j+1} \frac{\Delta s}{\tau^{\mathrm{VD}}} + n_i^{j+1} T_{\mathrm{i},\perp,i}^{j+1} \frac{\Delta s}{\tau_{\mathrm{rlx},i}^{j+1}} + \frac{2 m_{\mathrm{e}}}{m_{\mathrm{i}}} n_i^{j+1} T_{\mathrm{i},\perp,i}^{j+1} \frac{\Delta s}{\tau_{\mathrm{e},i}^{j+1}} \\
&= Q_{\mathrm{i},\perp,i}^{j+1} \Delta s + n_i^{j+1} T_{\mathrm{i},//,i}^{j+1} \frac{\Delta s}{\tau_{\mathrm{rlx},i}^{j+1}} + \frac{2 m_{\mathrm{e}}}{m_{\mathrm{i}}} n_i^{j+1} T_{\mathrm{e},i}^{j+1} \frac{\Delta s}{\tau_{\mathrm{e},i}^{j+1}},
\end{aligned} \qquad \text{(A.62)}
$$

$$
\left( n T_{\mathrm{i},\perp} V \right)_{i+1/2}^{j+1} = \begin{cases}
n_i^{j+1} T_{\mathrm{i},\perp,i}^{j+1} \left[ V_i^{j+1}, 0 \right] \\
- n_{i+1}^{j+1} T_{\mathrm{i},\perp,i+1}^{j+1} \left[ -V_i^{j+1}, 0 \right], \\
n_N^{j+1} T_{\mathrm{i},\perp,N}^{j+1} \left[ V_N^{j+1}, 0 \right] \\
- n_1^{j+1} T_{\mathrm{i},\perp,1}^{j+1} \left[ -V_N^{j+1}, 0 \right],
\end{cases} \begin{matrix} (1 \le i \le N-1) \\ (i = N) \end{matrix} \qquad \text{(A.63)}
$$

$$\left(nT_{\mathrm{i},\perp}V\right)_{i-1/2}^{j+1}=\begin{cases} n_N^{j+1}T_{\mathrm{i},\perp,N}^{j+1}\left[V_N^{j+1},0\right] & \\ -n_1^{j+1}T_{\mathrm{i},\perp,1}^{j+1}\left[-V_N^{j+1},0\right], & (i=1) \\ n_{i-1}^{j+1}T_{\mathrm{i},\perp,i-1}^{j+1}\left[V_{i-1}^{j+1},0\right] & \\ -n_i^{j+1}T_{\mathrm{i},\perp,i}^{j+1}\left[-V_{i-1}^{j+1},0\right], & (2\le i\le N) \end{cases} \tag{A.64}$$

$$\left(-\kappa_{\mathrm{i},\perp}^{\mathrm{eff}}\frac{\partial T_{\mathrm{i},\perp}}{\partial s}\right)_{i+1/2}^{j+1}=\begin{cases} -\kappa_{\mathrm{i},\perp,i+1/2}^{\mathrm{eff},j+1}\dfrac{T_{\mathrm{i},\perp,i+1}^{j+1}-T_{\mathrm{i},\perp,i}^{j+1}}{\Delta s}, & (1\le i\le N-1) \\ -\kappa_{\mathrm{i},\perp,N+1/2}^{\mathrm{eff},j+1}\dfrac{T_{\mathrm{i},\perp,1}^{j+1}-T_{\mathrm{i},\perp,N}^{j+1}}{\Delta s}, & (i=N) \end{cases} \tag{A.65}$$

$$\left(-\kappa_{\mathrm{i},\perp}^{\mathrm{eff}}\frac{\partial T_{\mathrm{i},\perp}}{\partial s}\right)_{i-1/2}^{j+1}=\begin{cases} -\kappa_{\mathrm{i},\perp,1/2}^{\mathrm{eff},j+1}\dfrac{T_{\mathrm{i},\perp,1}^{j+1}-T_{\mathrm{i},\perp,N}^{j+1}}{\Delta s}, & (i=1) \\ -\kappa_{\mathrm{i},\perp,i-1/2}^{\mathrm{eff},j+1}\dfrac{T_{\mathrm{i},\perp,i}^{j+1}-T_{\mathrm{i},\perp,i-1}^{j+1}}{\Delta s}, & (2\le i\le N) \end{cases} \tag{A.66}$$

$$\kappa_{\mathrm{i},\perp,i+1/2}^{\mathrm{eff}}=\begin{cases} \dfrac{2\kappa_{\mathrm{i},\perp,i}^{\mathrm{eff}}\kappa_{\mathrm{i},\perp,i+1}^{\mathrm{eff}}}{\kappa_{\mathrm{i},\perp,i}^{\mathrm{eff}}+\kappa_{\mathrm{i},\perp,i+1}^{\mathrm{eff}}}, & (1\le i\le N-1) \\ \dfrac{2\kappa_{\mathrm{i},\perp,N}^{\mathrm{eff}}\kappa_{\mathrm{i},\perp,1}^{\mathrm{eff}}}{\kappa_{\mathrm{i},\perp,N}^{\mathrm{eff}}+\kappa_{\mathrm{i},\perp,1}^{\mathrm{eff}}}. & (i=N) \end{cases} \tag{A.67}$$

Equation (A.62) is rewritten in the form of Eq. (2.51) as follows;

$$a_iT_{\mathrm{i},\perp,i}^{j+1}=\begin{cases} b_1T_{\mathrm{i},\perp,2}^{j+1}+c_1T_{\mathrm{i},\perp,N}^{j+1}+d_1, & (i=1) \\ b_iT_{\mathrm{i},\perp,i+1}^{j+1}+c_iT_{\mathrm{i},\perp,i-1}^{j+1}+d_i, & (2\le i\le N-1) \\ b_NT_{\mathrm{i},\perp,1}^{j+1}+c_NT_{\mathrm{i},\perp,N-1}^{j+1}+d_N, & (i=N) \end{cases} \tag{A.68}$$

$$a_i=\begin{cases} n_1^{j+1}\left(\dfrac{\Delta s}{\Delta t}+\dfrac{g_{\mathrm{i},\perp}^{\mathrm{VD}}\Delta s}{\tau^{\mathrm{VD}}}+\dfrac{\Delta s}{\tau_{\mathrm{rlx},1}^{j+1}}+\dfrac{2m_{\mathrm{e}}}{m_{\mathrm{i}}}\dfrac{\Delta s}{\tau_{\mathrm{e},1}^{j+1}}\right) & \\ +n_1^{j+1}\left(\left[V_1^{j+1},0\right]+\left[-V_N^{j+1},0\right]\right) & \\ +\dfrac{\kappa_{\mathrm{i},\perp,3/2}^{\mathrm{eff},j+1}+\kappa_{\mathrm{i},\perp,1/2}^{\mathrm{eff},j+1}}{\Delta \mathrm{s}}, & (i=1) \\ n_i^{j+1}\left(\dfrac{\Delta s}{\Delta t}+\dfrac{g_{\mathrm{i},\perp}^{\mathrm{VD}}\Delta s}{\tau^{\mathrm{VD}}}+\dfrac{\Delta s}{\tau_{\mathrm{rlx},i}^{j+1}}+\dfrac{2m_{\mathrm{e}}}{m_{\mathrm{i}}}\dfrac{\Delta s}{\tau_{\mathrm{e},i}^{j+1}}\right) & \\ +n_i^{j+1}\left(\left[V_i^{j+1},0\right]+\left[-V_{i-1}^{j+1},0\right]\right) & \\ +\dfrac{\kappa_{\mathrm{i},\perp,i+1/2}^{\mathrm{eff},j+1}+\kappa_{\mathrm{i},\perp,i-1/2}^{\mathrm{eff},j+1}}{\Delta \mathrm{s}}, & (2\le i\le N) \end{cases} \tag{A.69}$$

$$b_i = \begin{cases} n_{i+1}^{j+1}\left[-V_i^{j+1},0\right]+\dfrac{\kappa_{\mathrm{i},\perp,i+1/2}^{\mathrm{eff},j+1}}{\Delta s}, & (1\le i\le N-1) \\ n_1^{j+1}\left[-V_N^{j+1},0\right]+\dfrac{\kappa_{\mathrm{i},\perp,N+1/2}^{\mathrm{eff},j+1}}{\Delta s}, & (i=N) \end{cases} \tag{A.70}$$

$$c_i = \begin{cases} n_N^{j+1}\left[V_N^{j+1},0\right]+\dfrac{\kappa_{\mathrm{i},\perp,1/2}^{\mathrm{eff},j+1}}{\Delta s}, & (i=1) \\ n_{i-1}^{j+1}\left[V_{i-1}^{j+1},0\right]+\dfrac{\kappa_{\mathrm{i},\perp,i-1/2}^{\mathrm{eff},j+1}}{\Delta s}, & (2\le i\le N) \end{cases} \tag{A.71}$$

$$d_i = n_i^j T_{\mathrm{i},\perp,i}^j \frac{\Delta s}{\Delta t} + Q_{\mathrm{i},\perp,i}^{j+1}\Delta s + n_i^{j+1}T_{\mathrm{i},/\!/,i}^{j+1}\frac{\Delta s}{\tau_{\mathrm{rlx},i}^{j+1}} + n_i^{j+1}T_{\mathrm{e},i}^{j+1}\frac{2m_\mathrm{e}}{m_\mathrm{i}}\frac{\Delta s}{\tau_{\mathrm{e},i}^{j+1}}. \tag{A.72}$$

*Equation of electron energy transport*

The equation of electron energy transport, Eq. (2.7), is discretized as follows;

$$\begin{aligned} &\left(\frac{3}{2}n_i^{j+1}T_{\mathrm{e},i}^{j+1}-\frac{3}{2}n_i^j T_{\mathrm{e},i}^j\right)\frac{\Delta s}{\Delta t}+\left(\frac{5}{2}nT_\mathrm{e}V\right)_{i+1/2}^{j+1}-\left(\frac{5}{2}nT_\mathrm{e}V\right)_{i-1/2}^{j+1} \\ &+\left(-\kappa_\mathrm{e}^{\mathrm{eff}}\frac{\partial T_\mathrm{e}}{\partial s}\right)_{i+1/2}^{j+1}-\left(-\kappa_\mathrm{e}^{\mathrm{eff}}\frac{\partial T_\mathrm{e}}{\partial s}\right)_{i-1/2}^{j+1} \\ &+\frac{3}{2}g_\mathrm{e}^{\mathrm{VD}}n_i^{j+1}T_{\mathrm{e},i}^{j+1}\frac{\Delta s}{\tau^{\mathrm{VD}}}+\frac{3m_\mathrm{e}}{m_\mathrm{i}}n_i^{j+1}T_{\mathrm{e},i}^{j+1}\frac{\Delta s}{\tau_{\mathrm{e},i}^{j+1}} \\ &-\frac{1}{2}V_{i-1}^{j+1}\left(n_i^{j+1}T_{\mathrm{e},i}^{j+1}-n_{i-1}^{j+1}T_{\mathrm{e},i-1}^{j+1}\right)-\frac{1}{2}V_i^{j+1}\left(n_{i+1}^{j+1}T_{\mathrm{e},i+1}^{j+1}-n_i^{j+1}T_{\mathrm{e},i}^{j+1}\right) \\ &=Q_{\mathrm{e},i}^{j+1}\Delta s+\frac{3m_\mathrm{e}}{m_\mathrm{i}}n_i^{j+1}T_{\mathrm{i},i}^{j+1}\frac{\Delta s}{\tau_{\mathrm{e},i}^{j+1}}, \end{aligned} \tag{A.73}$$

$$\left(\frac{5}{2}nT_\mathrm{e}V\right)_{i+1/2}^{j+1} = \begin{cases} \dfrac{5}{2}n_i^{j+1}T_{\mathrm{e},i}^{j+1}\left[V_i^{j+1},0\right] & \\ -\dfrac{5}{2}n_{i+1}^{j+1}T_{\mathrm{e},i+1}^{j+1}\left[-V_i^{j+1},0\right], & (1\le i\le N-1) \\ \dfrac{5}{2}n_N^{j+1}T_{\mathrm{e},N}^{j+1}\left[V_N^{j+1},0\right] & (i=N) \\ -\dfrac{5}{2}n_1^{j+1}T_{\mathrm{e},1}^{j+1}\left[-V_N^{j+1},0\right], & \end{cases} \tag{A.74}$$

$$\left(\frac{5}{2}nT_{\mathrm{e}}V\right)_{i-1/2}^{j+1}=\begin{cases}\dfrac{5}{2}n_N^{j+1}T_{\mathrm{e},N}^{j+1}\left[V_N^{j+1},0\right] & \\ -\dfrac{5}{2}n_1^{j+1}T_{\mathrm{e},1}^{j+1}\left[-V_N^{j+1},0\right], & (i=1)\\ \dfrac{5}{2}n_{i-1}^{j+1}T_{\mathrm{e},i-1}^{j+1}\left[V_{i-1}^{j+1},0\right] & (2\le i\le N)\\ -\dfrac{5}{2}n_i^{j+1}T_{\mathrm{e},i}^{j+1}\left[-V_{i-1}^{j+1},0\right], & \end{cases} \tag{A.75}$$

$$\left(-\kappa_{\mathrm{e}}^{\mathrm{eff}}\frac{\partial T_{\mathrm{e}}}{\partial s}\right)_{i+1/2}^{j+1}=\begin{cases}-\kappa_{\mathrm{e},i+1/2}^{\mathrm{eff},j+1}\dfrac{T_{\mathrm{e},i+1}^{j+1}-T_{\mathrm{e},i}^{j+1}}{\Delta s}, & (1\le i\le N-1)\\ -\kappa_{\mathrm{e},N+1/2}^{\mathrm{eff},j+1}\dfrac{T_{\mathrm{e},1}^{j+1}-T_{\mathrm{e},N}^{j+1}}{\Delta s}, & (i=N)\end{cases} \tag{A.76}$$

$$\left(-\kappa_{\mathrm{e}}^{\mathrm{eff}}\frac{\partial T_{\mathrm{e}}}{\partial s}\right)_{i-1/2}^{j+1}=\begin{cases}-\kappa_{\mathrm{e},1/2}^{\mathrm{eff},j+1}\dfrac{T_{\mathrm{e},1}^{j+1}-T_{\mathrm{e},N}^{j+1}}{\Delta s}, & (i=1)\\ -\kappa_{\mathrm{e},i-1/2}^{\mathrm{eff},j+1}\dfrac{T_{\mathrm{e},i}^{j+1}-T_{\mathrm{e},i-1}^{j+1}}{\Delta s}, & (2\le i\le N)\end{cases} \tag{A.77}$$

$$\kappa_{\mathrm{e},i+1/2}^{\mathrm{eff}}=\begin{cases}\dfrac{2\kappa_{\mathrm{e},i}^{\mathrm{eff}}\kappa_{\mathrm{e},i+1}^{\mathrm{eff}}}{\kappa_{\mathrm{e},i}^{\mathrm{eff}}+\kappa_{\mathrm{e},i+1}^{\mathrm{eff}}}, & (1\le i\le N-1)\\ \dfrac{2\kappa_{\mathrm{e},N}^{\mathrm{eff}}\kappa_{\mathrm{e},1}^{\mathrm{eff}}}{\kappa_{\mathrm{e},N}^{\mathrm{eff}}+\kappa_{\mathrm{e},1}^{\mathrm{eff}}}. & (i=N)\end{cases} \tag{A.78}$$

Equation (A.73) is rewritten in the form of Eq. (2.51) as follows;

$$a_iT_{\mathrm{e},i}^{j+1}=\begin{cases}b_1T_{\mathrm{e},2}^{j+1}+c_1T_{\mathrm{e},N}^{j+1}+d_1, & (i=1)\\ b_iT_{\mathrm{e},i+1}^{j+1}+c_iT_{\mathrm{e},i-1}^{j+1}+d_i, & (2\le i\le N-1)\\ b_NT_{\mathrm{e},1}^{j+1}+c_NT_{\mathrm{e},N-1}^{j+1}+d_N, & (i=N)\end{cases} \tag{A.79}$$

$$a_i = \begin{cases} n_1^{j+1}\left(\dfrac{3\Delta s}{2\Delta t}+\dfrac{3g_{\mathrm{i},\perp}^{\mathrm{VD}}\Delta s}{2\tau^{\mathrm{VD}}}+\dfrac{3m_{\mathrm{e}}}{m_{\mathrm{i}}}\dfrac{\Delta s}{\tau_{\mathrm{e},1}^{j+1}}\right) \\ +\dfrac{5}{2}n_1^{j+1}\left(\left[V_1^{j+1},0\right]+\left[-V_N^{j+1},0\right]\right) \\ +\dfrac{\kappa_{\mathrm{e},3/2}^{\mathrm{eff},j+1}+\kappa_{\mathrm{e},1/2}^{\mathrm{eff},j+1}}{\Delta \mathrm{s}}+\dfrac{1}{2}n_1^{j+1}\left(V_1^{j+1}-V_N^{j+1}\right), & (i=1) \\ n_i^{j+1}\left(\dfrac{3\Delta s}{2\Delta t}+\dfrac{3g_{\mathrm{i},\perp}^{\mathrm{VD}}\Delta s}{2\tau^{\mathrm{VD}}}+\dfrac{3m_{\mathrm{e}}}{m_{\mathrm{i}}}\dfrac{\Delta s}{\tau_{\mathrm{e},i}^{j+1}}\right) \\ +\dfrac{5}{2}n_i^{j+1}\left(\left[V_i^{j+1},0\right]+\left[-V_{i-1}^{j+1},0\right]\right) \\ +\dfrac{\kappa_{\mathrm{e},i+1/2}^{\mathrm{eff},j+1}+\kappa_{\mathrm{e},i-1/2}^{\mathrm{eff},j+1}}{\Delta \mathrm{s}}+\dfrac{1}{2}n_i^{j+1}\left(V_i^{j+1}-V_{i-1}^{j+1}\right), & (2\le i\le N) \end{cases} \tag{A.80}$$

$$b_i = \begin{cases} \dfrac{5}{2}n_{i+1}^{j+1}\left[-V_i^{j+1},0\right]+\dfrac{\kappa_{\mathrm{e},i+1/2}^{\mathrm{eff},j+1}}{\Delta s}+\dfrac{1}{2}n_{i+1}^{j+1}V_i^{j+1}, & (1\le i\le N-1) \\ \dfrac{5}{2}n_1^{j+1}\left[-V_N^{j+1},0\right]+\dfrac{\kappa_{\mathrm{e},N+1/2}^{\mathrm{eff},j+1}}{\Delta s}+\dfrac{1}{2}n_1^{j+1}V_N^{j+1}, & (i=N) \end{cases} \tag{A.81}$$

$$c_i = \begin{cases} \dfrac{5}{2}n_N^{j+1}\left[V_N^{j+1},0\right]+\dfrac{\kappa_{\mathrm{e},1/2}^{\mathrm{eff},j+1}}{\Delta s}-\dfrac{1}{2}n_N^{j+1}V_N^{j+1}, & (i=1) \\ \dfrac{5}{2}n_{i-1}^{j+1}\left[V_{i-1}^{j+1},0\right]+\dfrac{\kappa_{\mathrm{e},i-1/2}^{\mathrm{eff},j+1}}{\Delta s}-\dfrac{1}{2}n_{i-1}^{j+1}V_{i-1}^{j+1}, & (2\le i\le N) \end{cases} \tag{A.82}$$

$$d_i = \frac{3}{2}n_i^j T_{\mathrm{e},i}^j\frac{\Delta s}{\Delta t}+Q_{\mathrm{e},i}^{j+1}\Delta s+n_i^{j+1}T_{\mathrm{i},i}^{j+1}\frac{3m_{\mathrm{e}}}{m_{\mathrm{i}}}\frac{\Delta s}{\tau_{\mathrm{e},i}^{j+1}}. \tag{A.83}$$

*Equation of continuity for outer recycling neutrals*

The equation of continuity for outer recycling neutrals, Eq. (4.13), is discretized as follows;

$$\begin{aligned} &\left(n_{\mathrm{n,recy},i}^{\mathrm{out},j+1}-n_{\mathrm{n,recy},i}^{\mathrm{out},j}\right)\frac{\Delta x}{\Delta t} \\ &+\left(n_{\mathrm{n,recy}}^{\mathrm{out}}V_{\mathrm{n,recy}}^{\mathrm{out}}\right)_{i+1/2}^{j+1}-\left(n_{\mathrm{n,recy}}^{\mathrm{out}}V_{\mathrm{n,recy}}^{\mathrm{out}}\right)_{i-1/2}^{j+1}+n_{\mathrm{n,recy},i}^{\mathrm{out},j+1}\nu_{\mathrm{L,recy}\,i}\Delta x \\ &=S_{\mathrm{n,recy},i}^{\mathrm{out},j+1}\Delta x+\eta nH\left(-V\right)\frac{\Delta x}{\tau^{\mathrm{VD}}}+\eta_{\mathrm{n}}n_{\mathrm{n,diff},i}^{j+1}H\left(\frac{\partial n_{\mathrm{n,diff},i}^{j+1}}{\partial x}\right)\frac{\Delta x}{\tau_{\mathrm{n}}^{\mathrm{VD}}}, \end{aligned} \tag{A.84}$$

$$\left(n_{\mathrm{n,recy}}^{\mathrm{out}} V_{\mathrm{n,recy}}^{\mathrm{out}}\right)_{i+1/2}^{j+1} = n_{\mathrm{n,recy}i}^{\mathrm{out},j+1} V_{\mathrm{n,recy}}^{\mathrm{out}}, \tag{A.85}$$

$$\left(n_{\mathrm{n,recy}}^{\mathrm{out}} V_{\mathrm{n,recy}}^{\mathrm{out}}\right)_{i-1/2}^{j+1} = \begin{cases} n_{\mathrm{n,recy},N}^{\mathrm{out},j+1} V_{\mathrm{n,recy}}^{\mathrm{out}}, & (i=1) \\ n_{\mathrm{n,recy}i-1}^{\mathrm{out},j+1} V_{\mathrm{n,recy}}^{\mathrm{out}}. & (2 \le i \le N) \end{cases} \tag{A.86}$$

Equation (A.84) is rewritten in the form of Eq. (2.51) as follows;

$$a_i n_{\mathrm{n,recy},i}^{\mathrm{out},j+1} = \begin{cases} b_1 n_{\mathrm{n,recy},2}^{\mathrm{out},j+1} + c_1 n_{\mathrm{n,recy},N}^{\mathrm{out},j+1} + d_1, & (i=1) \\ b_i n_{\mathrm{n,recy},i+1}^{\mathrm{out},j+1} + c_i n_{\mathrm{n,recy},i-1}^{\mathrm{out},j+1} + d_i, & (2 \le i \le N-1) \\ b_N n_{\mathrm{n,recy},1}^{\mathrm{out},j+1} + c_N n_{\mathrm{n,recy},N-1}^{\mathrm{out},j+1} + d_N, & (i=N) \end{cases} \tag{A.87}$$

$$a_i = \frac{\Delta x}{\Delta t} + \nu_{\mathrm{L,recy},i} \Delta x + V_{\mathrm{n,recy}}^{\mathrm{out}}, \tag{A.88}$$

$$b_i = 0, \tag{A.89}$$

$$c_i = V_{\mathrm{n,recy}}^{\mathrm{out}}, \tag{A.90}$$

$$\begin{aligned} d_i &= n_{\mathrm{n,recy},i}^{\mathrm{out},j} \frac{\Delta x}{\Delta t} + S_{\mathrm{n,recy},i}^{\mathrm{out},j+1} \Delta x \\ &+ \eta n H(-V) \frac{\Delta x}{\tau^{\mathrm{VD}}} + \eta_{\mathrm{n}} n_{\mathrm{n,diff},i}^{j+1} H\left(\frac{\partial n_{\mathrm{n,diff},i}^{j+1}}{\partial x}\right) \frac{\Delta x}{\tau_{\mathrm{n}}^{\mathrm{VD}}}. \end{aligned} \tag{A.91}$$

*Equation of continuity for inner recycling neutrals*

The equation of continuity for inner recycling neutrals, Eq. (4.14), is discretized as follows;

$$\begin{aligned} &\left(n_{\mathrm{n,recy},i}^{\mathrm{inn},j+1} - n_{\mathrm{n,recy},i}^{\mathrm{inn},j}\right) \frac{\Delta x}{\Delta t} \\ &+ \left(n_{\mathrm{n,recy}}^{\mathrm{inn}} V_{\mathrm{n,recy}}^{\mathrm{inn}}\right)_{i+1/2}^{j+1} - \left(n_{\mathrm{n,recy}}^{\mathrm{inn}} V_{\mathrm{n,recy}}^{\mathrm{inn}}\right)_{i-1/2}^{j+1} + n_{\mathrm{n,recy},i}^{\mathrm{inn},j+1} \nu_{\mathrm{L,recy}i} \Delta x \\ &= S_{\mathrm{n,recy},i}^{\mathrm{inn},j+1} \Delta x + \eta n H(V) \frac{\Delta x}{\tau^{\mathrm{VD}}} + \eta_{\mathrm{n}} n_{\mathrm{n,diff},i}^{j+1} H\left(-\frac{\partial n_{\mathrm{n,diff},i}^{j+1}}{\partial x}\right) \frac{\Delta x}{\tau_{\mathrm{n}}^{\mathrm{VD}}}, \end{aligned} \tag{A.92}$$

$$\left(n_{\mathrm{n,recy}}^{\mathrm{inn}} V_{\mathrm{n,recy}}^{\mathrm{inn}}\right)_{i+1/2}^{j+1} = \begin{cases} n_{\mathrm{n,recy}i+1}^{\mathrm{inn},j+1} V_{\mathrm{n,recy}}^{\mathrm{inn}}, & (1 \le i \le N-1) \\ n_{\mathrm{n,recy}1}^{\mathrm{inn},j+1} V_{\mathrm{n,recy}}^{\mathrm{inn}}, & (i=N) \end{cases} \tag{A.93}$$

$$\left(n_{\mathrm{n,recy}}^{\mathrm{inn}} V_{\mathrm{n,recy}}^{\mathrm{inn}}\right)_{i-1/2}^{j+1} = n_{\mathrm{n,recy},i}^{\mathrm{inn},j+1} V_{\mathrm{n,recy}}^{\mathrm{inn}}. \tag{A.94}$$

Equation (A.92) is rewritten in the form of Eq. (2.51) as follows;

$$a_i n_{\mathrm{n,recy},i}^{\mathrm{inn},j+1} = \begin{cases} b_1 n_{\mathrm{n,recy},2}^{\mathrm{inn},j+1} + c_1 n_{\mathrm{n,recy},N}^{\mathrm{inn},j+1} + d_1, & (i=1) \\ b_i n_{\mathrm{n,recy},i+1}^{\mathrm{inn},j+1} + c_i n_{\mathrm{n,recy},i-1}^{\mathrm{inn},j+1} + d_i, & (2 \le i \le N-1) \\ b_N n_{\mathrm{n,recy},1}^{\mathrm{inn},j+1} + c_N n_{\mathrm{n,recy},N-1}^{\mathrm{inn},j+1} + d_N, & (i=N) \end{cases} \tag{A.95}$$

$$a_i = \frac{\Delta x}{\Delta t} + \nu_{\mathrm{L,recy},i} \Delta x - V_{\mathrm{n,recy}}^{\mathrm{inn}}, \tag{A.96}$$

$$b_i = -V_{\mathrm{n,recy}}^{\mathrm{inn}}, \tag{A.97}$$

$$c_i = 0, \tag{A.98}$$

$$\begin{aligned} d_i &= n_{\mathrm{n,recy},i}^{\mathrm{inn},j} \frac{\Delta x}{\Delta t} + S_{\mathrm{n,recy},i}^{\mathrm{inn},j+1} \Delta x \\ &+ \eta n H(V) \frac{\Delta x}{\tau^{\mathrm{VD}}} + \eta_{\mathrm{n}} n_{\mathrm{n,diff},i}^{j+1} H\left(-\frac{\partial n_{\mathrm{n,diff},i}^{j+1}}{\partial x}\right) \frac{\Delta x}{\tau_{\mathrm{n}}^{\mathrm{VD}}}. \end{aligned} \tag{A.99}$$

*Equation of continuity for diffusion neutrals*

The equation of continuity for diffusion neutrals, Eq. (4.15), is discretized as follows;

$$\begin{aligned} &\left(n_{\mathrm{n,diff},i}^{j+1} - n_{\mathrm{n,diff},i}^{j}\right)\frac{\Delta x}{\Delta t} + n_{\mathrm{n,diff},i}^{j+1} \frac{\Delta x}{\tau_{\mathrm{n}}^{\mathrm{VD}}} + n_{\mathrm{n,diff},i}^{j+1} \nu_{\mathrm{L,diff},i} \Delta x \\ &+ \left(-D_{\mathrm{n}} \frac{\partial n_{\mathrm{n,diff}}}{\partial x}\right)_{i+1/2}^{j+1} - \left(-D_{\mathrm{n}} \frac{\partial n_{\mathrm{n,diff}}}{\partial x}\right)_{i-1/2}^{j+1} = S_{\mathrm{n,recy},i}^{\mathrm{inn},j+1} \Delta x, \end{aligned} \tag{A.100}$$

$$\left(-D_{\mathrm{n}} \frac{\partial n_{\mathrm{n,diff}}}{\partial x}\right)_{i+1/2}^{j+1} = \begin{cases} -D_{\mathrm{n},i+1/2}^{j+1} \dfrac{n_{\mathrm{n,diff},i+1}^{j+1} - n_{\mathrm{n,diff},i}^{j+1}}{\Delta x}, & (1 \le i \le N-1) \\ -D_{\mathrm{n},1/2}^{j+1} \dfrac{n_{\mathrm{n,diff},1}^{j+1} - n_{\mathrm{n,diff},N}^{j+1}}{\Delta x}, & (i=N) \end{cases} \tag{A.101}$$

$$\left(-D_{\mathrm{n}} \frac{\partial n_{\mathrm{n,diff}}}{\partial x}\right)_{i-1/2}^{j+1} = \begin{cases} -D_{\mathrm{n},1/2}^{j+1} \dfrac{n_{\mathrm{n,diff},1}^{j+1} - n_{\mathrm{n,diff},N}^{j+1}}{\Delta x}, & (i=1) \\ -D_{\mathrm{n},i-1/2}^{j+1} \dfrac{n_{\mathrm{n,diff},i}^{j+1} - n_{\mathrm{n,diff},i-1}^{j+1}}{\Delta x}. & (2 \le i \le N) \end{cases} \tag{A.102}$$

Here, the particle diffusivities at the boundaries of the cells are estimated by the harmonic average of those at the adjacent grids as follows;

$$D_{\mathrm{n},i+1/2} = \begin{cases} \dfrac{2D_{\mathrm{n},i}D_{\mathrm{n},i+1}}{D_{\mathrm{n},i}+D_{\mathrm{n},i+1}}, & (1 \le i \le N-1) \\ \dfrac{2D_{\mathrm{n},N}D_{\mathrm{n},1}}{D_{\mathrm{n},N}+D_{\mathrm{n},1}}. & (i = N) \end{cases} \tag{A.103}$$

Equation (A.100) is rewritten in the form of Eq. (2.51) as follows;

$$a_i n_{\mathrm{n,diff},i}^{j+1} = \begin{cases} b_1 n_{\mathrm{n,diff},2}^{j+1} + c_1 n_{\mathrm{n,diff},N}^{j+1} + d_1, \\ b_i n_{\mathrm{n,diff},i+1}^{j+1} + c_i n_{\mathrm{n,diff},i-1}^{j+1} + d_i, \\ b_N n_{\mathrm{n,diff},1}^{j+1} + c_N n_{\mathrm{n,diff},N-1}^{j+1} + d_N, \end{cases} \tag{A.104}$$

$$a_i = \frac{\Delta x}{\Delta t} + \frac{\Delta x}{\tau_{\mathrm{n}}^{\mathrm{VD}}} + \nu_{\mathrm{L,diff},i}\Delta x + \frac{D_{\mathrm{n},i+1/2}^{j+1}}{\Delta x} + \frac{D_{\mathrm{n},i-1/2}^{j+1}}{\Delta x}, \tag{A.105}$$

$$b_i = \frac{D_{\mathrm{n},i+1/2}^{j+1}}{\Delta x}, \tag{A.106}$$

$$c_i = \frac{D_{\mathrm{n},i-1/2}^{j+1}}{\Delta x}, \tag{A.107}$$

$$d_i = n_{\mathrm{n,diff},i}^{j} \frac{\Delta x}{\Delta t} + S_{\mathrm{n,diff},i}^{j+1}\Delta x. \tag{A.108}$$

*Calculation flow*

The coefficient matrix and the RHS of Eq. (2.52), $\mathrm{G}\boldsymbol{\varphi} = \boldsymbol{d}$, for one variable includes functions of itself or the other variables. In this sense, eight matrix equations for eight variables are non-linear and solved iteratively. Here, we denote the iteration step by *k*.

We set $\boldsymbol{\varphi}^{j+1,k=0} = \boldsymbol{\varphi}^{j}$. In order to obtain $\boldsymbol{\varphi}^{j+1,k=1}$, we estimate G and $\boldsymbol{d}$ by using $\boldsymbol{\varphi}^{j+1,k=0}$ as $\mathrm{G}^{j+1,k=0}\boldsymbol{\varphi}^{j+1,k=1} = \boldsymbol{d}^{j+1,k=0}$. Eight matrix equations are solved by Sherman-Morrison formula and TDMA as explained in Sec. 2.3. In order to obtain $\boldsymbol{\varphi}^{j+1,k+1}$, we again estimate G and $\boldsymbol{d}$ by using $\boldsymbol{\varphi}^{j+1,k}$ as $\mathrm{G}^{j+1,k}\boldsymbol{\varphi}^{j+1,k+1} = \boldsymbol{d}^{j+1,k}$. Iteration proceeds until the following equation is satisfied for all grid points *i* for eight variables;

$$\left| \frac{\varphi_i^{j+1,k+1} - \varphi_i^{j+1,k}}{\varphi_i^{j+1,k+1}} \right| < 10^{-4}. \tag{A.109}$$

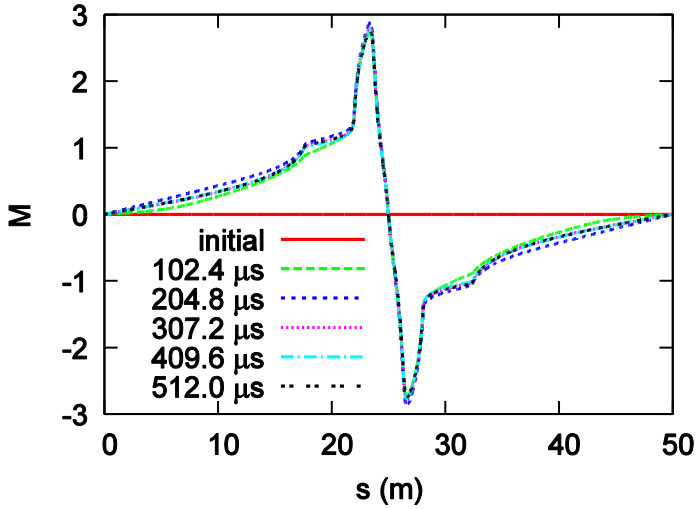


Figure 38 Time evolution of Mach profile from the initial condition to steady state.

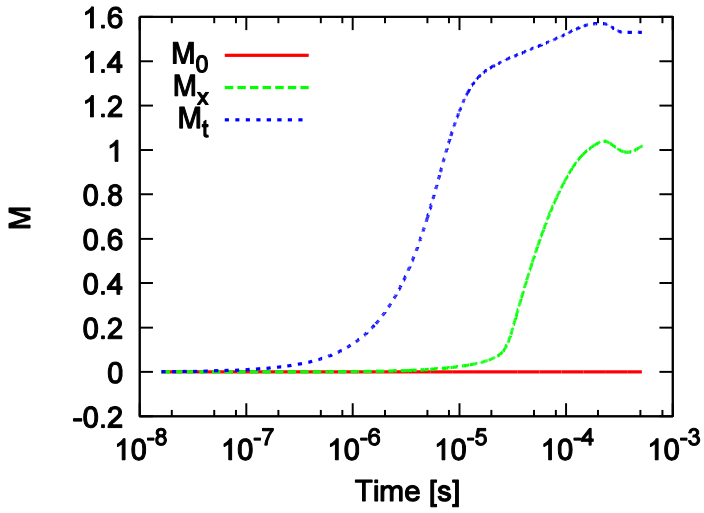


Figure 39 Time evolution of Mach numbers at the stagnation point ($s$ = 0, 50 m) $M_0$, X-point ($s$ = 17.6, 32.4 m) $M_X$ and the sheath entrance ($s$ = 22, 28 m) $M_t$ from the initial condition to steady state.

Then, we set $\boldsymbol{\varphi}^{j+1} = \boldsymbol{\varphi}^{j+1,k+1}$ and proceed to next time step $j$+2.

*Initial conditions and steady state*

We use a uniform profiles for eight variables whose values are $n = 10^{19}$ /m$^3$, $V$ = 0, $T_{i,//} = T_{i,\perp} = T_e = 100$ eV and $n_{n,recy}^{out} = n_{n,recy}^{inn} = n_{n,diff} = 0$, respectively. Figure 38 shows the time evolution of the Mach number profile for no neutral condition, and $\Gamma_{sep} = 2\times10^{22}$ /s and $P_{sep} = 4$ MW from the initial condition to steady state.

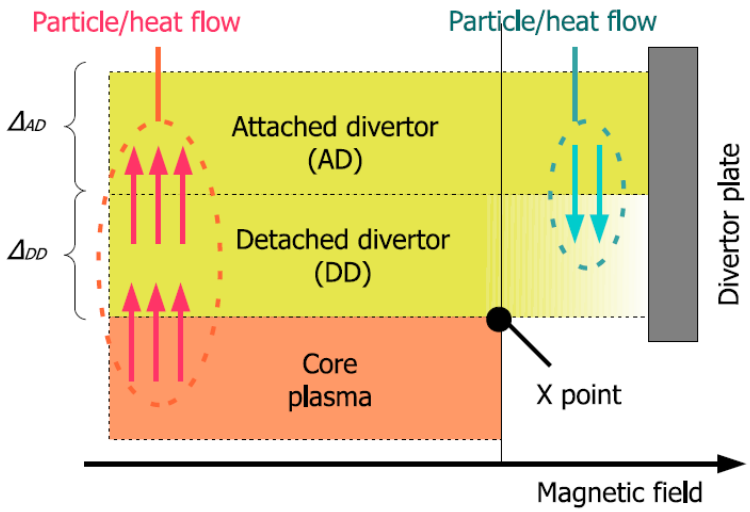


Figure 40 Schematic picture of the multi-layer 1D model [44].

Figure 39 shows the time evolution of Mach numbers at the stagnation point ($s$ = 0, 50 m) $M_0$, X-point ($s$ = 17.6, 32.4 m) $M_X$ and the sheath entrance ($s$ = 22, 28 m) $M_t$ in Fig. 38. $M_0$ keeps zero because of the symmetric condition. At first, $M_X$ and $M_t$ grow up to 1 and more than 1 and finally saturate at $t$ = 512 μs.

## A.4 Stabilization of the detachment front

We studied the stability of the detachment fronts in partially detached divertor plasma by using multi-layer 1D SOL-DIV model shown in Fig. 40 in Refs. [44], S. Togo *et al*., Plasma Fusion Res. **7** (2012), S. Togo *et al*., Plasma Fusion Res. **8** (2013) and S. Togo's master thesis research. In this model, we divided the flux tube radially and made detached plasmas in the inner tube which was close to the separatrix and attached plasmas in the outer tube by adjusting the gas puff at the divertor plate. Radial diffusive heat flux could be introduced between outer and inner tubes. In the calculation, $T_{i,//} = T_{i,\perp} = T_e = T$ was assumed and the viscosity term was neglected. Figure 41 shows the time evolution of the profiles of plasma density $n$ and temperature $T$. Without the radial diffusive heat flux, the detachment front moved to the X-point which indicated the cooling of the core plasma. By introducing the radial diffusive heat flux, the detachment front stayed in the DIV region. We concluded that this radial diffusive heat flux played an important role for stabilizing of the detachment fronts in the partially detached divertor plasma.

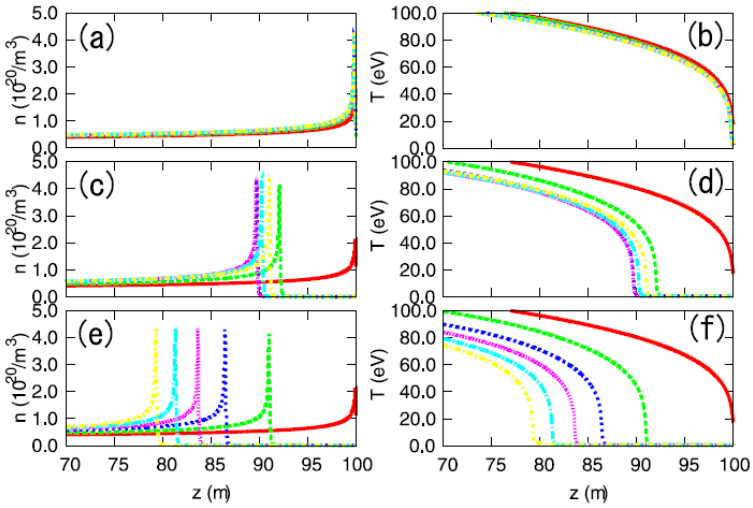


Figure 41 Time evolution of the profiles of plasma density $n$ (a), (c), (e) and temperature $T$ (b), (d) ,(f) in the outer (a), (b) and inner tubes (c)-(f). In (c) and (d), radial diffusive heat flux from the outer to inner flux tubes is introduced, but is absent in (e) and (f). X-point is located at $z$ = 80 m [44].

# References


[1] R. Dux *et al*., Nucl. Fusion **39** 1509 (1999).

[2] F. Ryter *et al*., Phys. Rev. Lett. **86** 5498 (2001).

[3] P. H. Rebut *et al*., Nucl. Fusion **25** 1011 (1985).

[4] JET team, Nucl. Fusion **32** 187 (1992).

[5] T. Ozeki *et al*., Nucl. Fusion **30** 1425 (1990).

[6] T. W. Petrie *et al*., Nucl. Fusion **37** 321 (1997).

[7] S. Ishida *et al*., Nucl. Fusion **51** 094018 (2011).

[8] H. Urano *et al*., Fusion Eng. Des. **100** 345 (2015).

[9] G. Janeschitz *et al*., J. Nucl. Mater. **290-293** 1 (2001).

[10] R. Kolesnikov *et al*., Nucl. Fusion **53** 083021 (2013).

[11] D. Maisonnier *et al*., Nucl. Fusion **47** 1524 (2007).

[12] K. Tobita *et al*., Nucl. Fusion **49** 075029 (2009).

[13] Y. Shimomura *et al*., Phys. Fluids **19** 1635 (1976).

[14] F. Wagner *et al*., Phys. Rev. Lett. **49** 1408 (1982).

[15] P. C. Stangeby, *The Plasma Boundary of Magnetic Fusion Devices*, Institute of Physics Publishing (Bristol and Philadelphia 1999).

[16] ITER Physics Expert Group on Divertor, Nucl. Fusion **39** 2391 (1999).

[17] K. Tobita *et al*., Nucl. Fusion **47** 892 (2007).

[18] K. Hoshino *et al*., Plasma Fusion Res. **9** 3403070 (2014).

[19] M. Groth *et al*., Nucl. Fusion **53** 093016 (2013).

[20] M. Wischmeier et al., J. Nucl. Mater. **415** S523 (2011).

[21] T. Takizuka *et al*., JAERI-Research 2003-010.

[22] R. Schneider *et al*., Contrib. Plasma Phys. **46** 3 (2006).

[23] H. Kawashima *et al*., Plasma Fusion Res. **1** 031 (2006).

[24] K. Shimizu *et al*., Nucl. Fusion **49** 065028 (2009).

[25] T. D. Rognlien *et al*., J. Nucl. Mater. **196-198** 347 (1992).

[26] R. Simonini *et al*., Contrib. Plasma Phys. **34** 368 (1994).

[27] B. Braams, *A Multi-Fluid Code for Simulation of the Edge Plasma in*

*Tokamaks*, NET rep. EUR-FU IXII-80-87-68, Comm. Of the European Communities (1987).

[28] K. Shimizu *et al*., J. Nucl. Mater. **313-316** 1277 (2003).

[29] D. Reiter *et al*., Plasma Phys. Control. Fusion **33** 1579 (1991).

[30] K. Shimizu *et al*., J. Nucl. Mater. **220-222** 410 (1995).

[31] S. Wiesen *et al*., J. Nucl. Mater. **463** 480 (2015).

[32] K. Hoshino *et al*., Contrib. Plasma Phys. **52** 550 (2012).

[33] N. Asakura *et al*., J. Nucl. Mater. **463** 1238 (2015).

[34] T. Lunt *et al*., Plasma Phys. Control. Fusion **56** 035009 (2014).

[35] K. Sato *et al*., Contrib. Plasma Phys. **34** 133 (1994).

[36] T. Takizuka *et al*., Contrib. Plasma Phys. **40** 471 (2000).

[37] S. I. Braginskii, Reviews of Plasma Physics **1** 205, New York (1965).

[38] K. Hoshino *et al*., Plasma Fusion Res. Ser. **9** 592 (2010).

[39] O. Marchuk and M. Z. Tokar, Contrib. Plasma Phys. **48** 164 (2008).

[40] A. V. Chankin *et al*., J. Nucl. Mater. **390-391** 319 (2009).

[41] M. Groth *et al*., J. Nucl. Mater. **415** S530 (2011).

[42] K. Hoshino *et al*., J. Nucl. Mater. **415** S549 (2011).

[43] S. Nakazawa *et al*., Plasma Phys. Control. Fusion **42** 401 (2000).

[44] M. Nakamura *et al*., J. Nucl. Mater. **415** S553 (2011).

[45] E. Zawaideh *et al*., Phys. Fluids **29** 463 (1986).

[46] W. Fundamenski, Plasma Phys. Control. Fusion **47** R.163 (2005).

[47] S. Togo *et al*., J. Nucl. Mater. **463** 502 (2015).

[48] T. Takizuka *et al*., J. Nucl. Mater. **128-129** 104 (1984).

[49] A. Froese *et al*., Plasma Fusion Res. **5** 026 (2010).

[50] P. Helander and D. J. Sigmar, *Collisional Transport in Magnetised Plasmas*, Cambridge University Press, New York (2002).

[51] J. P. Freidberg, *Plasma Physics and Fusion Energy*, Cambridge University Press (2007).

[52] P. Angot *et al*., Numer. Math. **81** 497 (1999).

[53] L. Isoardi *et al*., J. Comput. Phys. **229** 2220 (2010).

[54] A. Paredes *et al*., J. Nucl. Mater. **438** S625 (2013).

[55] G. Ciraolo *et al*., Contrib. Plasma Phys. **54** 432 (2014).

[56] S. V. Patankar, *Numerical Heat Transfer and Fluid Flow*, Hemisphere Publishing Co. (1980).

[57] W. H. Press, *Numerical Recipes in Fortran 77*, The Art of Scientific Computing. Cambridge University Press, New York (1992).
[58] T. Takizuka *et al*., J. Nucl. Mater. **290-293** 753 (2001).
[59] D. Tskhakaya *et al*., J. Nucl. Mater. **390-391** 335 (2009).
[60] E. L. Vold *et al*., J. Nucl. Mater. **176&177** 570 (1990).
[61] S. Togo *et al*., 42nd EPS Conference on Plasma Physics, P4.194 (2015).
[62] A. K. Prinja *et al*., J. Nucl. Mater. **196-198** 340 (1992).
[63] S. Togo *et al*., Contrib. Plasma Phys. to be published (2015).
[64] K. Hoshino and M. Toma, Plasma Fusion Res. **86** 681 (2010).
[65] D. E. Post, J. Nucl. Mater. **220-222** 143 (1995).
[66] K. Hoshino *et al*., Contrib. Plasma Phys. **48** 136 (2008).
[67] M. Sugihara *et al*., J. Nucl. Mater. **128-129** 114 (1984).
[68] K. Hoshino *et al*., J. Nucl. Mater. **463** 573 (2015).
[69] M. Ishida *et al*., Contrib. Plasma Phys. **50** 362 (2010).
[70] D. Reiter *et al*., Fusion Sci. Technol. **47** 172 (2005).

# Acknowledgement

I would like to express my deepest appreciation to Dr. Yuichi Ogawa for supervising my research for more than five years. He not only taught me the elementary knowledge of the plasma physics, but also told me the basic way to proceed the research. In addition, he introduced many kinds of conferences and meetings to me and encouraged me to attend them and write proceeding papers aggressively, which were valuable experiences in my student life.

I am deeply grateful to Dr. Tomonori Takizuka of Osaka University, who is one of the leading experts on the edge plasma, for coming every month from Naka city to our laboratory in Kashiwa city in order to discuss the results of our SOL-DIV plasma fluid code. He gave me lots of helpful comments on the numerical settings for the concept of virtual divertor model and the results from our code.

I would like to offer my special thanks to Dr. Makoto Nakamura of Japan Atomic Energy Agency (JAEA) who was a post-doctoral fellow in our laboratory and was developing a 1D SOL-DIV code when I was an undergraduate student. He taught me lots of knowledge on the SOL-DIV plasma physics and numerical simulations. The code became the basis of our code with virtual divertor model.

Dr. Kazuo Hoshino of JAEA, Dr. Kenzo Ibano of Osaka University and Mr. Tee Long Lang of University of Tokyo, who are also the coauthors of my papers, supported my research and writing papers through the monthly meeting in our laboratory. I would like to thank them deeply.

I would also like to thank Dr. Katsuhiro Shimizu of JAEA for helpful advice on the numerical schemes, Dr. Atsushi Okamoto of Nagoya University for fruitful discussions in the monthly meeting in our laboratory, Dr. Akiyoshi Hatayama of Keio University for inviting me to the meeting on plasma simulations every year, Dr. Kojiro Suzuki of University of Tokyo for the discussions on the fluid dynamics and Dr. Marco Wischmeier of Max-Planck-Institut für Plasmaphysik (IPP) for giving me an opportunity of making a presentation in IPP. My visit to Europe including IPP and EPS Conference on Plasma Physics was supported by the Academic Research Grant Program 2015 of Graduate School of Frontier Sciences.

As for the members of our laboratory, I want to thank Ms. Hashimoto for clerical works, Dr. Morikawa for supporting the network system and experiments and students for discussing the plasma physics in the sessions every morning.

Finally, I've been encouraged by my dear family and friends to live a life as a doctor course student and as a researcher in the future. I'm deeply grateful to them.

# Related Works

## 学術雑誌等に発表した論文

（査読有り）

(1) Makoto Nakamura, Satoshi Togo, Masanori Ito, Yuichi Ogawa, “One-Dimensional Time Dependent Analysis of the Detachment Front in a Divertor Plasma: Roles of the Cross-Field Transport”, Plasma and Fusion Research, The Japan Society of Plasma Science and Nuclear Fusion Research, **6**, pp. 2403098-1-4 (2012).

(2) Satoshi Togo, Makoto Nakamura, Yuichi Ogawa, Katsuhiro Shimizu, Tomonori Takizuka, Kazuo Hoshino, “Effects of Radial Losses of Particle and Energy on the Stability of Detachment Front in a Divertor Plasma”, Plasma and Fusion Research, The Japan Society of Plasma Science and Nuclear Fusion Research, **7**, pp. 2403087-1-4 (2012).

(3) Satoshi Togo, Makoto Nakamura, Yuichi Ogawa, Katsuhiro Shimizu, Tomonori Takizuka, Kazuo Hoshino, “Effects of Neutral Particles on the Stability of the Detachment Fronts in Divertor Plasmas”, Plasma and Fusion Research, The Japan Society of Plasma Science and Nuclear Fusion Research, **8**, pp. 2403096-1-4 (2013).

(4) Kenzo Ibano, Toshiki Tsutsui, Tee Long Lang, Satoshi Togo, Yuichi Ogawa, “Effects of impurity transport and melt layer motion to the tungsten wall erosion during anomaly events”, Journal of Nuclear Materials, ELSEVIER, **463**, pp. 185-188 (2015).

(5) Satoshi Togo, Tomonori Takizuka, Makoto Nakamura, Kazuo Hoshino, Yuichi Ogawa, “SOL–divertor plasma simulations introducing anisotropic temperature with virtual divertor model”, Journal of Nuclear Materials, ELSEVIER, **463**, pp. 502-505 (2015).

(6) Kenzo Ibano, Satoshi Togo, Tee Long Lang, Yuichi Ogawa, Heun Tae Lee, Yoshio Ueda, Tomonori Takizuka, “Simulations of Tungsten re-deposition

using a particle-in-cell code with non-uniform super particle sizes", Contributions to Plasma Physics, WILEY-VCH (2015) *to be published*.

(7) Satoshi Togo, Tomonori Takizuka, Makoto Nakamura, Kazuo Hoshino, Kenzo Ibano, Tee Long Lang, Yuichi Ogawa, "Simulation Study of Detached Plasmas by Using One-Dimensional SOL-Divertor Fluid Code with Virtual Divertor Model", Contributions to Plasma Physics, WILEY-VCH (2015) *to be published*.

(8) Satoshi Togo, Tomonori Takizuka, Makoto Nakamura, Kazuo Hoshino, Kenzo Ibano, Tee Long Lang, Yuichi Ogawa, "Self-consistent treatment of the sheath boundary conditions by introducing anisotropic ion temperatures and virtual divertor model", Journal of Computational Physics, ELSEVIER, **310**, pp. 109-126 (2016).

（査読無し）

(1) Satoshi Togo, Tomonori Takizuka, Makoto Nakamura, Kazuo Hoshino, Yuichi Ogawa, "Simulation Study of SOL-Divertor Plasmas Using a Virtual Divertor Model", 12th Burning Plasma Simulation Initiative (BPSI) Meeting, RIAM, pp. 15-18 (2015).

(2) Satoshi Togo, Tomonori Takizuka, Makoto Nakamura, Kazuo Hoshino, Kenzo Ibano, Tee Long Lang, Yuichi Ogawa, "Improvement of One-Dimensional Fluid Modeling of the SOL-Divertor Plasmas and Neutrals Concerning the Anisotropy of Ion Temperature and the Diffusion Coefficient of Neutrals", 42nd EPS Conference on Plasma Physics, P4.194 (2015).

(3) Satoshi Togo, Tomonori Takizuka, Makoto Nakamura, Kazuo Hoshino, Kenzo Ibano, Yuichi Ogawa, "Numerical analysis of the effects of radial plasma diffusion on the detached divertor plasmas", 13th Burning Plasma Simulation Initiative (BPSI) Meeting, RIAM (2016) *to be published*.

## 国際会議における発表

（ポスター発表、査読無し）

(1) ○Satoshi Togo, Makoto Nakamura, Yuichi Ogawa, Katsuhiro Shimizu,

Tomonori Takizuka, Kazuo Hoshino, “Effects of Radial Losses of Particle and Energy on the Stability of Detachment Front in a Divertor Plasma”, 21st International Toki Conference, P1-16, Toki, Japan, November 2011.

(2) ○Satoshi Togo, Makoto Nakamura, Yuichi Ogawa, Katsuhiro Shimizu, Tomonori Takizuka, Kazuo Hoshino, “Effects of Neutral Particles on the Stability of the Detachment Fronts in Divertor Plasmas”, 22nd International Toki Conference, P2-47, Toki, Japan, November 2012.

(3) ○Satoshi Togo, Tomonori Takizuka, Makoto Nakamura, Kazuo Hoshino, Yuichi Ogawa, “SOL–divertor plasma simulations introducing anisotropic temperature with virtual divertor model”, 21st International Conference on Plasma Surface Interactions, P2-038, Kanazawa, Japan, May 2014.

(4) ○Satoshi Togo, Tomonori Takizuka, Makoto Nakamura, Kazuo Hoshino, Kenzo Ibano, Tee Long Lang, Yuichi Ogawa, “Improvement of One-Dimensional Fluid Modeling of the SOL-Divertor Plasmas and Neutrals Concerning the Anisotropy of Ion temperature and the Diffusion Coefficient of Neutrals”, 42nd European Physical Society Conference on Plasma Physics, P4.194, Lisbon, Portugal, June 2015.

(5) ○Satoshi Togo, Tomonori Takizuka, Makoto Nakamura, Kazuo Hoshino, Kenzo Ibano, Tee Long Lang, Yuichi Ogawa, “Simulation Study of Detached Plasmas by Using One-Dimensional SOL-Divertor Fluid Code with Virtual Divertor Model”, 15th International Workshop on Plasma Edge Theory in Fusion Devices, P1-29, Nara, Japan, September 2015.

## 国内学会・シンポジウム等における発表

（口頭発表、査読無し）

(1) ○Satoshi Togo, Makoto Nakamura, Katsuhiro Shimizu, Tomonori Takizuka, Kazuo Hoshino, Yuichi Ogawa, “Analysis of Partially Detached Divertor Plasmas with Multi-Layer 1D Model”, Plasma Conference 2011, 24C06, Kanazawa, November 2011.

(2) ○東郷訓，中村誠，清水勝宏，滝塚知典，星野一生，小川雄一，「多層型一次元モデルを用いた部分非接触ダイバータプラズマ解析」，NIFS共同研究「原型炉へ向けた周辺・炉心プラズマ統合モデリング」研究作業会，土岐市, 2月, 2012.

(3) ○東郷訓, 中村誠, 清水勝宏, 滝塚知典, 星野一生, 小川雄一, 「一次元ダイバータプラズマコードの現状」, NIFS共同研究「原型炉に向けた周辺・炉心プラズマ統合モデリングによるダイバータ熱・粒子制御研究」研究作業会, 土岐市, 2月, 2013.

(4) ○東郷訓, 滝塚知典, 中村誠, 星野一生, 小川雄一, “SOL-divertor plasma simulations with virtual divertor model”, NIFS共同研究「原型炉に向けた周辺・炉心プラズマ統合モデリングによるダイバータ熱・粒子制御研究」研究作業会, 土岐市, 2月, 2014.

(5) ○東郷訓, 滝塚知典, 中村誠, 星野一生, 小川雄一, 「非等方イオン温度と仮想ダイバータモデルを導入したSOL-ダイバータプラズマシミュレーション」, プラズマ物理クラスター・スクレープオフ層とダイバータ物理サブクラスター, 炉工学クラスター・ブランケットサブクラスター/ダイバータサブクラスター合同会合, つくば市, 7-8月, 2014.

(6) ○東郷訓, 滝塚知典, 中村誠, 星野一生, 小川雄一, 「イオン温度の非等方性を考慮したSOL-ダイバータプラズマシミュレーション」, NIFS共同研究合同研究会（「境界領域プラズマ挙動の理解とその制御」研究会, プラズマ物理クラスター・周辺・ペデスタル物理サブクラスター会合）, 土岐市, 8月, 2014.

(7) ○Satoshi Togo, Tomonori Takizuka, Makoto Nakamura, Kazuo Hoshino, Yuichi Ogawa, “Simulation Study Using a Virtual Divertor Model on the Supersonic Flow in SOL-Divertor Plasmas Considering the Anisotropic Ion Temperature”, Plasma Conference 2014, 20pC2-4, Niigata, November 2014.

(8) ○Satoshi Togo, Tomonori Takizuka, Makoto Nakamura, Kazuo Hoshino, Yuichi Ogawa, “Simulation Study of SOL-Divertor Plasmas Using a Virtual Divertor Model”, 12th Burning Plasma Simulation Initiative (BPSI) Meeting, 1-4, Kasuga, December 2014.

(9) ○東郷訓, 滝塚知典, 中村誠, 星野一生, 伊庭野健造, Lang Tee Long, 小川雄一, 「仮想ダイバータモデルを用いたSOL-ダイバータシミュレーション研究の進展」, NIFS共同研究「不純物を含めた周辺・炉心プラズマ統合モデリング」研究作業会, 土岐市, 2月, 2015.

(10) ○東郷訓, 滝塚知典, 中村誠, 星野一生, 伊庭野健造, Lang Tee Long, 小川雄一, 「仮想ダイバータモデルに適合した中性粒子モデルと拡散

係数の効果」, NIFS共同研究合同研究会（「境界領域プラズマダイナミクスの診断と制御」研究会, プラズマ物理クラスター・周辺・ペデスタル物理サブクラスター会合）, 土岐市, 7月, 2015.

(11) ○東郷訓, 滝塚知典, 中村誠, 星野一生, 伊庭野健造, Lang Tee Long, 小川雄一, “Self-consistent treatment of sheath boundary conditions by virtual divertor model”, プラズマ物理クラスター・スクレープオフ層とダイバータ物理サブクラスター, 炉工学クラスター・ブランケットサブクラスター/ダイバータサブクラスター/炉材料サブクラスター合同会合, つくば市, 7月, 2015.

(12) ○Satoshi Togo, Tomonori Takizuka, Makoto Nakamura, Kazuo Hoshino, Kenzo Ibano, Tee Long Lang, Yuichi Ogawa, “Numerical Analysis of Detached Divertor Plasmas by Focusing on the Effects of Supersonic Plasma Flows”, 日本物理学会2015年秋季大会, 18pCN-6, Suita, September 2015.

(13) ○Satoshi Togo, Tomonori Takizuka, Makoto Nakamura, Kazuo Hoshino, Kenzo Ibano, Yuichi Ogawa, “Numerical analysis of the effects of radial plasma diffusion on the detached divertor plasmas”, 13th Burning Plasma Simulation Initiative (BPSI) Meeting, 3-3, Kasuga, December 2015.

(ポスター発表、査読無し)

(1) ○Satoshi Togo, Makoto Nakamura, Katsuhiro Shimizu, Tomonori Takizuka, Kazuo Hoshino, Yuichi Ogawa, “Effects of Neutral Particles on the Stability of the Detachment Fronts in Divertor Plasmas”, 第29回プラズマ・核融合学会年会, 28D31P, Kasuga, November 2012.

(2) ○Satoshi Togo, Tomonori Takizuka, Makoto Nakamura, Kazuo Hoshino, Yuichi Ogawa, “Simulations of Edge Plasmas Using the Virtual Divertor Model”, 第10回核融合エネルギー連合講演会, 19-068, Tsukuba, June 2014.

(3) ○Satoshi Togo, Tomonori Takizuka, Makoto Nakamura, Kazuo Hoshino, Kenzo Ibano, Tee Long Lang, Yuichi Ogawa, “Simulation Study of Detached Divertor Plasmas by Using a Virtual Divertor Model Concerning the Effect of Radial Plasma Diffusion”, 第32回プラズマ・核融合学会年会, 24pE25P, Nagoya, November 2015.

# 受賞歴

(1) 東郷訓, 「若手優秀発表賞」, Plasma Conference 2014, 20pC2-4, Niigata, November 2014.